Passive Flow Control in Spatially Developing Turbulent Boundary Layers

THE UNIVERSITY of ADELAIDE

Chi Ip Chan

School of Mechanical Engineering

The University of Adelaide

This dissertation is submitted for the degree of

Doctor of Philosophy

June 2022

Abstract

Flow control is a primary focus in most industrial and energy applications, for example, for skin friction drag reduction, enhancing heat transfer rate and aerodynamic noise reduction. As such, there has been an increasing demand for flow control strategies that aim to achieve these goals. This thesis presents numerical studies of the performance of two particular passive control approaches (i) large-eddy break up devices and (ii) miniature vortex generators in zero pressure gradient turbulent boundary layers through well-resolved numerical simulations. The numerical code is based on an efficient spectral integration method to solve the Navier–Stokes equations for the incompressible boundary layer flows. Flow geometry is implemented through an immerse boundary method. Simulations have been performed and detailed flow fields obtained to reveal many flow features that would otherwise be costly and difficult to capture in experiments. The instantaneous and mean flow behaviours of the turbulent boundary layers modified by these passive control methods are discussed, with the intention of providing a better physical understanding of these passive control strategies. In this thesis, several flow analysis approaches and theoretical studies based on the turbulent boundary layer equations have been conducted with the aim to provide new physical insights into the analysis methods of flow structures on a drag reduced flat plate turbulent boundary layer.

Preface

This thesis is submitted as a "thesis by publications" in accordance with "specifications for thesis" of the University of Adelaide. The thesis is based on and contains the following papers.

Paper 1. Chan, C. I., Schlatter, P. and Chin, R. C. (2021). Interscale transport mechanisms in turbulent boundary layers. *Journal of Fluid Mechanics*, 921, A13.

Paper 2. Chan, C. I., Örlü, R., Schlatter, P. and Chin, R. C. (2021). The skin-friction coefficient of a turbulent boundary layer modified by a large-eddy break-up device. *Physics of Fluids* 33, 035153.

Paper 3. Chan, C. I., Örlü, R., Schlatter, P. and Chin, R. C. (2022). Large-scale and small-scale contribution to the skin friction reduction in a modified turbulent boundary layer by a large-eddy break-up device. Submitted to *Physical Review Fluids* and accepted on 14 February for publication.

Paper 4. Chan, C. I. and Chin, R. C. (2022). Investigation of the influence of miniature vortex generators on the large-scale motions of a turbulent boundary layer. *Journal of Fluid Mechanics*, 932, A29.

Paper 5. Chan, C. I. and Chin, R. C. (2022). Characteristics of momentum transport in a turbulent boundary layer modified by miniature vortex generators. Submitted to *Physical Review Fluids* and is currently under review.

Declaration

I certify that this work contains no material which has been accepted for the award of any other degree or diploma in my name, in any university or other tertiary institution and, to the best of my knowledge and belief, contains no material previously published or written by another person, except where due reference has been made in the text. In addition, I certify that no part of this work will, in the future, be used in a submission in my name, for any other degree or diploma in any university or other tertiary institution without the prior approval of the University of Adelaide and where applicable, any partner institution responsible for the joint-award of this degree. I acknowledge that copyright of published works contained within this thesis resides with the copyright holder(s) of those works. I also give permission for the digital version of my thesis to be made available on the web, via the University's digital research repository, the Library Search and also through web search engines, unless permission has been granted by the University to restrict access for a period of time. I acknowledge the support I have received for my research through the provision of an Australian Government Research Training Program Scholarship.

Chi Ip Chan

February 2022

Acknowledgements

I would like to thank my supervisors for their patience and timely support, especially Dr. Rey Chin for his prompt and pertinent editing. The Royal Institute of Technology (KTH), Dr. Ramis Örlü and Prof. Philipp Schlatter, are greatly acknowledged for providing me with the opportunity to meet some of the prominent researchers in turbulent flow research. This work was supported with supercomputing resources provided by the Phoenix HPC service at the University of Adelaide. This research was undertaken with the assistance of resources provided at the NCI NF through the National Computational Merit Allocation Scheme, supported by the Australian Government. The PhD scholarship was provided by the University of Adelaide Research Scholarships (Adelaide Graduate Research Scholarships) and is gratefully acknowledged.

Table of contents

Chapter 1

Introduction

1.1 Background and objectives

The study of controlling wall-bounded flows is of great interest in engineering practice. Energy consumption can be reduced by drag reduction using different flow control methods, thereby improving the energy efficiency and reducing the costs. Flows in most of the engineering applications are turbulent, such as flows over the surface of an aircraft wing, cargo ship or pipelines. Research on flow control in wall-bounded flows was only possible through experimental investigations in the early 1980s, using passive approaches such as riblets, outer-layer devices and polymer additives [14]. Advances in computational power and turbulence modelling have prompted the full-scale and large-eddy numerical simulations of flow control studies over the past few decades. Flow control methods have been studied by both active and passive means [145, 129, 70, 46]. Flow control research has been focused on specifically targeting the coherent structures in wall-bounded flows [46]. From studies aiming to suppress the structures associated with near-wall cycle to the recent evidence that indicates the increasing near-wall modulation of the energetic large-scale motions in the outer region of the boundary layer, large-scale control studies have been targeting large-eddy control.

The aim of this work is to perform numerical simulations to investigate small- and large-scale passive controls in a spatially developing zero pressure gradient turbulent boundary layer (ZPG TBL). In particular, we focus on two types of passive approaches

amongst the available flow control techniques, which have attracted considerable interest due to their simplicity and ease of manufacturing: (i) large-eddy-break-up (LEBU) devices and (ii) miniature vortex generators (MVGs).

The first objective is to evaluate the performance of LEBU devices in TBLs. The LEBU device consists of single or multiple thin flat plates that are aligned along the flow direction and are positioned at different wall-normal distances from the wall, typically at a height scaled with the outer unit δ (boundary layer thickness), from 0.1δ to 0.8δ [173, 31, 5]. The existing studies in the literature have not provided information on the underlying mechanism for the local skin friction reduction that can be sustainable for downstream distances up to $O(100\delta)$ along the boundary layer. There is, therefore, a need to perform studies using numerical simulations, to further explore the drag reduction mechanism and the influences of the LEBU devices on the turbulent flow structures. In this study, we applied three approaches to elucidate the skin friction drag reduction mechanism of the LEBU device: (a) the Fukagata–Iwamoto–Kasagi (FIK) identity proposed by Fukagata et al. [66] where the skin friction coefficient is decomposed into four dynamic effects (see §2.2.2), which enables a quantitative discussion on the drag reduction contributions; (b) quadrant analysis of Reynolds shear stress exploited by Wallace et al. [213] where the Reynolds shear stress is classified by the sign of the product of the velocity fluctuations. As the hairpin vortices are closely related to the second and fourth quadrants [3], this enables a discussion of the influences of LEBU devices on the boundary layer structures and (c) spectral analysis provides a better understanding of the energy contribution of large-scale/small-scale (wavelengths) eddies to the streamwise velocity fluctuations as well as to the Reynolds shear stress [49].

The second objective is to examine the feasibility of using large-scale vortices to control TBLs and to reduce skin friction drag. The large-scale vortices will be imposed through the MVG. The MVG consists of pairs of winglets or rectangular blades arranged in spanwise oriented arrays positioned at the wall of a boundary layer. The performance of MVGs has been examined in laminar boundary layers for transition delay and flow separation. The MVGs have also been examined experimentally and numerically in laminar boundary layers, and have demonstrated substantial levels of drag reduction [189, 176]. This work

aims to investigate the performance of MVGs in a TBL: (i) to reduce skin friction at a solid surface, (ii) to disrupt or interfere with the coherent structures that have been found to populate at high Reynolds numbers TBLs (see review in §2.1) and (iii) to find the appropriate scaling of the MVG-induced flow features in TBLs. The present study aims to extend previous experimental investigations to a moderate Reynolds number TBL using well-resolved numerical simulations.

The thesis is organised as follows: Chapter 2 provides reviews on active and passive flow control studies, LEBU devices and MVGs. The aim is to provide an introduction for the earlier flow control studies that have most relevance to the current investigation. In Chapter 2 we also review relevant literature about smooth-wall ZPG TBL and coherent structures in turbulent wall-bounded flows, and review some of the relevant literature about the flow analysis we used in the papers. Chapter 3 provides the numerical procedures of our numerical simulations, including the large-eddy simulations and the flow geometry modelling. In Chapter 4 we summarise the papers. The conclusion of the thesis will be given in Chapter 5.

Chapter 2

Literature Review

2.1 Turbulent flows

2.1.1 Smooth wall-bounded flow - ZPG TBL

Incompressible flow Navier-stokes equations

The fundamental equations that describe the incompressible Newtonian fluids are the incompressible continuity equation and Navier–Stokes equations:

$$\frac{\partial u_i}{\partial x_i} = 0, \tag{2.1}$$

$$\frac{\partial u_i}{\partial t} + u_k \frac{\partial u_i}{\partial x_k} = -\frac{1}{\rho}\frac{\partial p}{\partial x_i} + \nu \Delta u_i, \tag{2.2}$$

which indicate the conservation of mass and momentum for fluids. To better characterise the turbulent flow, the flow velocity (and pressure) can be decomposed into a mean motion and a fluctuating motion following the Reynolds decomposition [199, 165]. The instantaneous flow velocity (and pressure) components can be decomposed into time-averaged and fluctuating components:

$$u_i(\boldsymbol{x}, t) = \overline{u}_i(\boldsymbol{x}) + u_i'(\boldsymbol{x}, t), \tag{2.3}$$

where the Cartesian coordinates in the streamwise, wall-normal and spanwise coordinates, in the remainder of the thesis, are denoted as x_i or $\boldsymbol{x} = (x, y, z)$. $\overline{u}_i$ or $\overline{\boldsymbol{u}} = (\overline{u}, \overline{v}, \overline{w})$ are the

mean velocities (where $\bar{\cdot}$ denotes time averaging) and their fluctuations are denoted as u_i' or $\boldsymbol{u'} = (u', v', w')$ (where $'$ denotes the fluctuation). The governing equations for the mean flow are the Reynolds-averaged Navier–Stokes equations (RANS):

$$\frac{\partial \overline{u}_i}{\partial x} = 0, \tag{2.4}$$

and

$$\overline{u}_k \frac{\partial \overline{u}_i}{\partial x_k} = -\frac{1}{\rho}\frac{\partial \overline{p}}{\partial x_i} + \nu \Delta \overline{u}_i - \frac{\partial \overline{u_i' u_k'}}{\partial x_k}, \tag{2.5}$$

where $\overline{u_i' u_k'}$ are the Reynolds stresses due to the shear forces of the turbulent fluctuations on the mean flow. The RANS are of interest for most practical applications, and are the foundational aspects with important implications for flow control analysis.

Momentum integral equations

In some practical applications the integral quantities are of interest, for example, to obtain an approximate method to determine the wall shear stress. For steady and two-dimensional turbulent boundary layers, the RANS can be reduced to the boundary layer equations in the form of

$$\frac{\partial \overline{u}}{\partial x} + \frac{\partial \overline{v}}{\partial y} = 0, \tag{2.6}$$

and

$$\overline{u}\frac{\partial \overline{u}}{\partial x} + \overline{v}\frac{\partial \overline{u}}{\partial y} = U_\infty \frac{dU_\infty}{dx} + \nu \frac{\partial^2 \overline{u}}{\partial y^2} - \frac{\partial \overline{u'v'}}{\partial y} - \frac{\partial}{\partial x}\left(\overline{u'u'} - \overline{v'v'}\right). \tag{2.7}$$

Integrates (2.6) and (2.7) with respect to y and gives

$$\frac{\tau_w(x)}{\rho} = \int_0^\infty U_\infty \frac{dU_\infty}{dx} dy + \int_0^\infty U_\infty \frac{\partial \overline{u}}{\partial x} dy - \int_0^\infty 2\overline{u}\frac{\partial \overline{u}}{\partial x} dy - \int_0^\infty \frac{\partial}{\partial x}\left(\overline{u'u'} - \overline{v'v'}\right) dy. \tag{2.8}$$

Rearranging gives the von Kármán integral equation:

$$\frac{\tau_w(x)}{\rho} = \frac{d}{dx}(\theta U_\infty^2) + \frac{dU_\infty}{dx}(\delta^* U_\infty) - \frac{d}{dx}\int_0^\infty \left(\overline{u'u'} - \overline{v'v'}\right) dy, \tag{2.9}$$

where θ and δ^* are the mean momentum thickness and mean displacement thickness, respectively,

$$\delta^*(x) = \int_0^\infty 1 - \frac{\overline{u}}{U_\infty} dy, \tag{2.10}$$

$$\theta(x) = \int_0^\infty \frac{\overline{u}}{U_\infty}\left(1 - \frac{\overline{u}}{U_\infty}\right) dy. \tag{2.11}$$

A useful result of the von Kármán integral equation is that it is a simplified boundary layer equation and an ordinary differential equation that provides a connection between the wall shear stress, momentum thickness and displacement thickness.

Logarithmic overlap law

A fundamental concept in boundary layer theory is the consideration of two types of scaling [210, 140], which provide a view that the flow can be divided into two flow regions; an inner scaling applied close to the wall and an outer scaling applied further away from the wall. The inner scaling suggests that the viscous effect is important close to the wall, and the outer scaling suggests that the viscous effect can be neglected and the flow becomes independent of the near-wall dynamics with an increasing Reynolds number. Considering that the total shear stress from the mean flow equation can be written as

$$\tau(x) = \tau_\nu + \tau_t = \rho\nu\frac{\partial\overline{u}}{\partial y} - \rho\overline{u'v'}, \tag{2.12}$$

where τ_ν is the mean viscous shear stress and $\tau_t = -\rho\overline{u'v'}$ is the Reynolds shear stress. The dimensional analysis gives the mean velocity distribution at the viscous wall layer as

$$\overline{u}^+ = f(y^+), \tag{2.13}$$

commonly referred to as the law of the wall. Considering the flow region further away from the wall, the viscous effect is less important and we assumed that the largest possible flow features will be in the order of the boundary layer thickness. Independently, at the

outer layer, the mean velocity has the form:

$$\overline{u}^+ = F(y/\delta, Re_\tau), \tag{2.14}$$

where δ is the boundary layer thickness, $\eta = y/\delta$, and $Re_\tau = \delta^+$ is the Reynolds number based on the friction velocity. The total shear stress (2.12) is normalised by the inner scales as

$$\frac{\tau(x)}{\rho u_\tau^2} = \frac{\partial \overline{u}^+}{\partial y^+} + \tau_t^+, \tag{2.15}$$

where u_τ is the friction velocity and the superscript + denotes non-dimensionalisation by u_τ and kinematic viscosity ν. The total shear stress can also be normalised by the outer scale δ as

$$\frac{\tau(x)}{\rho u_\tau^2} = \frac{\partial \overline{u}^+}{\partial \eta}\frac{1}{Re_\tau} + \tau_t^+. \tag{2.16}$$

At a sufficiently high Reynolds number, the overlap region exists. It is required that both the (2.15) and (2.16) boundary conditions hold at this region, such that

$$\lim_{y^+\to\infty} \frac{\partial \overline{u}^+}{\partial y^+} = \lim_{\eta\to 0} \frac{\partial \overline{u}^+}{\partial \eta}\frac{1}{Re_\tau}, \tag{2.17}$$

and therefore,

$$\lim_{y^+\to\infty} y^+ \frac{\partial \overline{u}^+}{\partial y^+} = \lim_{\eta\to 0} \frac{\partial \overline{u}^+}{\partial \eta}\eta = \text{const.} = \frac{1}{\kappa}, \tag{2.18}$$

where κ is the von Kármán constant [210]. For ZPG TBL, (2.18) can be rewritten as

$$\lim_{y\to 0} \frac{\partial \overline{u}}{\partial y} = \frac{u_\tau}{\kappa y}. \tag{2.19}$$

Integration with respect to y gives

$$\overline{u}^+(y^+) = \frac{1}{\kappa}\ln\left(y^+\right) + C, \tag{2.20}$$

the so-called logarithmic overlap law. The overlap law describes how the universal law of the wall behaves for $y^+ \to \infty$ [140], and is of fundamental importance in the study of

scaling laws and logarithmic layer in high Reynolds number turbulent wall-bounded flows [138].

Transport of turbulent-kinetic-energy

Apart from these mean flow characterisations, the Reynolds stress (tensor) transport equations describe the physical processes of turbulent fluctuations [170, 165, 182]. A particularly useful form of the tensor equation is the turbulent kinetic energy (Reynolds normal stresses) transport, derived from the Navier–Stokes equations, given by

$$\frac{Dk}{Dt}(\boldsymbol{x}) = P_k + T_k + D_k + \Pi_k - \varepsilon_k, \tag{2.21}$$

where $Dk/Dt = \partial k/\partial t + \bar{u}_j \partial k/\partial x_j$ is the mean flow material derivative of k and $k = \frac{1}{2}\overline{u_i' u_i'}$ is the turbulent kinetic energy. All the terms on the right-hand side of (2.21) are

$$\begin{aligned}
&\text{Turbulence production} && P_k(\boldsymbol{x}) = -\overline{u_i' u_j'}\frac{\partial \overline{u}_i}{\partial x_j};\\
&\text{Turbulent diffusion} && T_k(\boldsymbol{x}) = -\frac{1}{2}\frac{\partial \overline{u_i' u_i' u_j'}}{\partial x_j};\\
&\text{Viscous diffusion} && D_k(\boldsymbol{x}) = \nu\frac{\partial^2 k}{\partial x_j^2};\\
&\text{Pressure diffusion} && \Pi_k(\boldsymbol{x}) = -\overline{u_i'\frac{\partial p'}{\partial x_i}};\\
&\text{Dissipation} && \varepsilon_k(\boldsymbol{x}) = -\nu\overline{\frac{\partial u_i'}{\partial x_j}\frac{\partial u_i'}{\partial x_j}}.
\end{aligned} \tag{2.22}$$

The left-hand side of (2.21) represents the time dependence and advection due to the mean flow motion. The first term on the right-hand side is the rate of production of turbulent kinetic energy from the mean motion (P_k). The following three terms on the right-hand side represent the diffusion of kinetic energy due to the turbulence (T_k), viscosity (D_k) and pressure gradient Π_k, respectively. The last term on the right-hand side is the dissipation of turbulent kinetic energy by viscosity (ε_k). In the context of flow control studies, the

peak kinetic energy production at the viscous buffer layer and the balance between the production and dissipation at the overlap layer are of interest [34, 35]. Choi et al. [35] studied the opposite control of near-wall streamwise vortices to achieve a friction-drag reduction in the channel flow. They computed the production and dissipation of TKE in manipulated (*v, w*-control) channel flows. They found that both production and dissipation were weakened and shifted away from the wall to the location where u'_{rms} is the maximum as a result of the increased thickness of the viscous-sublayer. Choi et al. [34] used DNS to study TBL over riblets, which interfere with the flow in the buffer layer to reduce skin friction. Choi et al. [34] computed the production rate P_k and concluded that the term $-\overline{u'v'}\partial\bar{u}/\partial y$ is the main contribution to the total production, which is related to the positive Reynolds-shear-stress-producing-events (ejection $Q2$ and sweep $Q4$ of the quadrants analysis, as discussed in §2.1.2). A link between the skin friction drag reduction and the global balance of turbulent kinetic energy transport has been demonstrated in previous studies [197, 67, 87, 94]. Sumitani and Kasagi [197] computed Reynolds stresses and TKE transport equations to investigate the effects of uniform wall injection and suction on the turbulent transports in a channel flow. They found that injection enhances each term in the TKE equation, while suction suppresses it. Fukagata and Kasagi [67] computed a weighted Reynolds shear stresses budget in a pipe flow with feedback control to investigate the skin friction contribution from the FIK decomposition proposed by Fukagata et al. [66]. They concluded that the drag reduction is due to the significant decrease in the pressure-strain term in the near-wall region. In addition to the above-mentioned numerical studies, experiments studied by Hou et al. [87] on drag reduction resulting from polymer injection in TBL have shown that, in one of their test cases, as the polymer injection concentration increases, the drag reduction also increases. This is associated with a shifted outward production rate from the wall and decreased peak value. Jelly et al. [94] computed the TKE budget for their superhydrophobic surface study, and the production term was further decomposed into primary and secondary production, in which the terms $-\overline{u'v'}\partial\bar{u}/\partial y$ and $-\overline{u'w'}\partial\bar{w}/\partial z$ are the most dominant terms. In paper 2, we investigated the effect of LEBU on the distribution of turbulent kinetic energy. The weakened turbulent kinetic energy transport was shown to be associated with the maximum skin friction drag reduction.

Beside this, a more useful tool for understanding the multi-length scales structures and their interaction of wall-bounded turbulence that makes use of the Reynolds stress (tensor) transport equations is studied in paper 1 and is reviewed in the following section (§2.2.3).

2.1.2 Coherent structures of wall-bounded turbulent flows

The structural representation of turbulent wall-bounded flows (ZPG TBL, channel and pipe flows) has been intensively studied over several decades [192]. The terminology "coherent structures" is used to refer to the spatial and temporal coherences of these organised motions [24, 169, 3, 192]. A general classification of the coherent structures is based on their kinematic properties, such as their relative positions and length scales. The coherent structures were shown to be multi-scale of characteristic length scales ranging from $O(\nu/u_\tau)$ relevant to the near-wall structures to $O(\delta)$ for large-scale structures away from the wall.

Near-wall cycle

In the near-wall region, coherent structures can be visualised as horseshoe or hairpin vortices [200, 206, 158, 81] which often attached to the wall, as well as in the form of quasi-streamwise vortices and streamwise elongated low- and high-speed streaks [109, 95, 114] of order $O(\nu/u_\tau)$, which govern the near-wall dynamics. The streaks are found to have a mean spanwise width of $\Delta z^+ \simeq 100$ and mean streamwise length of $\Delta x^+ \simeq 1000$ [114, 155]. The low-speed streaks lift up from the wall by bursting, and account for most of the Reynolds shear stress generation and play an important role in the production of turbulent kinetic energy [43, 106, 80, 185]. The low-speed streaks, or ejection events, are subsequently followed by relatively larger-scale and faster-moving high-speed streaks or so-called the sweep events that occur closer to the wall [43]. It has been shown that the near-wall turbulence generation is a self-sustaining cycle composed of three different stages [106, 211, 155]. The quasi-streamwise vortices lift up and create streaks, which is followed by streak instability, and in turn, form new vortices by streamwise vorticity [106]. The

self-sustained cycle requires no interaction with the outer region, and was shown to be independent of the outer-layer conditions [97, 155].

Quadrant analysis of Reynolds shear stress

Wallace et al. [213] extended the work by Corino and Brodkey [43] of near-wall events. The near-wall events can be further classified by the quadrant analysis of Reynolds shear stress [128, 212], which can be expressed as

$$\begin{aligned} Q_1 &= \{u'v' \,|\, u' > 0, v' > 0\}, \quad Q_2 = \{u'v' \,|\, u' < 0, v' > 0\}, \\ Q_3 &= \{u'v' \,|\, u' < 0, v' < 0\}, \quad Q_4 = \{u'v' \,|\, u' > 0, v' < 0\}, \end{aligned} \tag{2.23}$$

where $u'v' = \sum_{n=1}^{4} Q_n$, and Q_n denotes the n^{th} quadrant of Reynolds shear stress. An ejection event is related to the Q_2 motion, defined as $u' < 0$ and $v' > 0$, where u', v' are the velocity fluctuations in the streamwise and wall-normal direction (2.3), and a sweep event is related to the Q_4 motion where $u' > 0$, $v' < 0$. The quadrant analysis of Reynolds shear stress provides a quantitative evaluation of the ejection and sweep events that observed in the work of Corino and Brodkey [43], which are related to the Q_2 and Q_4 motions and are the major fractional contributions to the Reynolds shear stress [109, 147, 128]. The other two quadrants are the Q_1 and Q_3 motions defined as $u' > 0$ and $v' > 0$ and $u' < 0$ and $v' < 0$, and are referred to the outward and inward interactions [212]. Quadrant analysis has gained interest in ejection and sweep type events as fundamental elements of turbulent wall-bounded flows and have generated many ideas for flow research based on the quadrant classification of the momentum, heat and vorticity covariances. For example, Nagano and Tagawa [151] employed the idea of quadrant classification to study wall-normal heat flux, based on velocity and temperature fluctuations. Ong and Wallace [154] performed the joint probability density analysis of the vorticity convariances and revealed the role of vorticity fluctuation plays in enstrophy transport equations. There have been many reviews related to the role of ejection and sweep events in fully turbulent wall-bounded flows. Willmarth and Lu [215] extended the quadrant analysis method by focusing on intense Reynolds

shear stress events.

$$|u'v'| \geq H_m|(u'v')_{\text{mean}}|, \tag{2.24}$$

where H_m is the hyperbolic-hole filtering size [215, 128] and $(u'v')_{\text{mean}}$ is the mean value of $u'v'$ for a given distance from the wall. Lozano-Durán et al. [126] further generalised this for three-dimensional turbulent channel flows.

$$|u'v'(y,z)| > H_r|u'_{\text{rms}}v'_{\text{rms}}(y)|, \tag{2.25}$$

where $H_r = 1.75$ is carefully selected based on the percolation analysis [126]. They identified two types of structures, which they called wall-detached and wall-attached quadrant events. It was shown that the wall-attached structures are responsible for most of the mean Reynolds shear stress and are important in the momentum transfer process. Extensions of this work by Lozano-Durán and Jiménez [127] studied the temporal evolution of three-dimensional structures of Reynolds shear stress in turbulent channel flows and showed that during the lifetimes of these structures, the ejections are generated by shear stress near the wall and rise to their mean wall-normal distance by vertical advection velocity ($+u_\tau$) before disappearing, whilst sweeps are produced away from the wall and move towards the wall quickly with $-u_\tau$, assembling into side-by-side sweep-ejection pairs [126]. Fiscaletti et al. [61] considered the intense quadrant events in turbulent boundary layers using the criterion based on Willmarth and Lu [215], demonstrating some noticeable differences in the intense quadrant events between turbulent boundary layers and channel flows. Overall, quadrant analysis of Reynolds shear stress is a fundamental tool in turbulent flow research. For a comprehensive review of quadrant analysis, the reader is referred to Wallace [212].

Hairpin vortices and the attached eddy model

In turbulent boundary layers there exist vortices commonly observed in the forms of horseshoe or hairpin vortices, which were believed to be the fundamental elements for turbulence production and momentum transport between the inner and outer regions [169]. There has been a long debate about whether or not these hairpin-like vortices exist. Head

and Bandyopadhyay [81] conducted flow visualisation studies of the ZPG TBL up to $Re_\theta < 17500$. They showed that at approximately $Re_\theta \simeq 10000$, the TBL was densely populated by flow features in the form of vortex loops, horseshoes or hairpins that elongated approximately at a characteristic angle of 45 degrees to the wall. The experimental studies of hairpin vortices were conducted while the measurement techniques were at relatively early stages of development [e.g. 60, 79, 2]. More recently, further supportive evidence of the hairpins and packets was drawn from experimental studies showing observations of hairpin packets through a newly-developed measurement tool called particle image velocimetry [4, 37, 72, 98] and from direct numerical simulation [216]. There is also a considerable body of evidence that suggested the Q_2 and Q_4 motions form the essential part of the hairpin vortices [4, 3], which through the nonlinear auto-generation mechanism forms new hairpins and packets [223, 98]. A packet consists of groups of streamwise-aligned hairpin vortices around a low-momentum region. Some studies using direct numerical simulation suggested that hairpins do not persist in fully turbulent boundary layer flows due to transition effects [95, 179]. Motoori and Goto [148] proposed that this controversial conclusion might be attributed to the mean shear stretching exerted among vortices. A recent study conducted by Dong et al. [54] in homogeneous shear turbulence suggested that the characteristic flow structure associated with forward and backward kinetic energy transfer is a vortex shaped as an inverted hairpin followed by an upright hairpin. Overall, there have been different models for the study of the flow structures and their generation mechanisms at the near-wall region and to the buffer and logarithmic regions. The importance of hairpin-like structures was also shown in a major model of wall-bounded turbulence based on the Townsend's attached eddy hypothesis [206], known as the attached eddy model [158–160, 137], which models the turbulent flow as hierarchies of geometrically self-similar eddies. Marusic [136] showed that the inclusion of packets of hairpin vortices into the attached eddy model improved the prediction of the velocity correlations and structure angles based on the model compared with the experimental results, suggesting that these spatially coherent packets are statistically important for the modelling of the logarithmic region.

Large-scale motions and inner-outer interactions

The observation of large-scale flow structures can be dated back over the past several decades [206, 77, 114, 115, 150, 19, 24, 169]. The study of Kim and Adrian [112] is one of the widely-recognised works regarding large-scale flow structures. The large-scale motions (LSMs) and very-large-scale motions (VLSMs) that scale with the local boundary layer thickness, channel half-height, or the pipe radius ($O(\delta)$) that reside in the logarithmic and outer regions [112, 50, 9, 204, 91], carry considerable amounts of the mean Reynolds shear stress and turbulent kinetic energy [78, 12]. The LSMs were shown to be associated with the formation of bulges due to the alignment of multiple hairpin structures that form the packets [192]. In high Reynolds number flows, the VLSMs are found to be very long with meandering features, consisting of alternating confined regions of low-streamwise-momentum and high-momentum fluids. These very-large-scale features were shown to have a streamwise length of $O(10R)$ where R is the pipe radius [112, 78, 12]. Similarly, these very-large-scale features were shown to have very long-meandering characteristics and length of order of $O(10\delta)$ in high Reynolds number turbulent boundary layers [91, 92, 146], where they are called superstructures. The VLSMs, or superstructures were shown to play a crucial role in turbulence production and contribution to the Reynolds shear stress. Further observations based on spectral analysis indicate that the footprints of superstructures extend to the wall as the low wavenumber energy shift in the streamwise velocity energy spectra. Additionally, there has been reported evidence of the inner-outer turbulence interactions in the literature [e.g. 15, 90, 1, 88, 164, 202, 71, 92, 139]. There are many ways to study the inner-outer interactions: for example, from a mathematical point of view, the scale-energy balance [e.g. 47, 83, 84, 134, 39, 40, 7] and the spectral Reynolds stress equation [143, 33, 119, 104] are time-dependent, nonlinear partial differential equations based on Navier-Strokes equations. The scale-energy balance considers the balance of the so-called second-order structure function:

$$\langle \delta u'^2 \rangle = \langle \delta u_i' \delta u_i' \rangle, \tag{2.26}$$

which is referred to as "scale-energy" and the velocity fluctuation differences $\delta u_i' = u_i'(\boldsymbol{x}_1) - u_i'(\boldsymbol{x}_2)$, where the mid-point position vector is $\boldsymbol{x_s} = (\boldsymbol{x}_1 + \boldsymbol{x}_2)/2$ and the separation vector $\boldsymbol{r_s} = \boldsymbol{x}_1 - \boldsymbol{x}_2$. The balance of the scale energy is the generalised Kolmogorov equation [84, 134], which, in general, can be recast into a six-dimensional space $(r_1, r_2, r_3, x_1, x_2, x_3)$. The reduced form of this equation is based on the four-dimensional space, or scale-energy "hyper-flux", which is studied in some notable turbulent channel flow studies, e.g. Marati et al. [134], Camarri et al. [21] and Cimarelli et al. [40]. These studies showed evidence of energy transfer from small scales to large scales (i.e. inverse energy transfer). A recent study by Alves-Portela et al. [7] has extended the analysis of the Kolmogorov equation for the turbulent planar wake of a square prism, as proposed by Thiesset et al. [201]. Another approach to study the inner-outer interaction is the Fourier-mode decomposition (sometimes simply referred to as the scale decomposition or mode decomposition), which requires the Fourier transform of the velocity fluctuation signal

$$u_i'(\tau, D) = \int_{-\infty}^{\infty} \mathcal{U}_i(\zeta) e^{i\tau\zeta}\, d\zeta, \tag{2.27}$$

$$\mathcal{U}_i(\zeta, D) = \int_{0}^{D} u_i'(\tau) e^{-i\tau\zeta}\, d\tau, \tag{2.28}$$

where $\mathcal{U}_i$ is the Fourier transform of u_i' and ζ is the wavenumber. τ is the displacement for the total distance (or total time) $D \to \infty$. An fast approximation of the one-sided wavenumber co-spectrum is

$$E_{ij}(\zeta) = 2\mathrm{Re}\Big[\lim_{D\to\infty} \frac{1}{D} \mathrm{Exp}\big[\mathcal{U}_i(\zeta, D)\, \mathcal{U}_j^*(\zeta, D)\big] \Big], \quad \zeta > 0, \tag{2.29}$$

where $\mathcal{U}_j^*(\zeta, D)$ is the complex conjugate of $\mathcal{U}_j(\zeta, D)$. $\mathrm{Exp}[\cdot]$ is the expected value operation and $\mathrm{Re}[\cdot]$ is the real part of the cross wavenumber spectral density function [16]. In practice, the total distance (or total time) D will be finite and the expected value is taken over a finite number of realisations [e.g. 78, 55] (i.e. ensemble averaging over all realisations [16]). The scale decomposition using spectral filters has been widely utilised for characterising large- and small-scale motions and their interactions. Hutchins and Marusic [92] used a spectral filter to capture the large-scale contribution to the streamwise velocity

fluctuation and revealed the large-scale modulation on the near-wall scales. A follow-up study by Mathis et al. [139] extended the work of Hutchins and Marusic [92] to study the modulation in more detail. They used the Hilbert transform of the decomposed small-scale fluctuation, where the modulation effects were analysed to be the large-scale envelope obtained by Hilbert transformation of the small-scale fluctuation, and they revealed a correlation between the near-wall cycle and the large-scale motions associated with the logarithmic region. Ganapathisubramani et al. [71] investigated the temporal modulation of the large-scale structures on the smaller scales using a time-scale decomposition and revealed the strong wall-normal dependence of the frequency modulation. An extended concept of the mode decomposition investigates the spectral analysis of the Reynolds stress transport equation, which considers the transport of spectral energy densities in the wavenumber space. In a two-dimensional case for streamwise-spanwise wavenumber space (k_x, k_z), the spectrum can be written as

$$\langle u_i' u_j' \rangle = \iint_{k_x,k_z} E_{ij,2D}(k_x, k_z) dk_x dk_z, \quad k_x > 0, k_z > 0, \tag{2.30}$$

and the relationship between two-dimensional and one-dimensional spectra as

$$E_{ij}(k_z) = \int_{k_z} E_{ij,2D}(k_x, k_z) dk_x. \tag{2.31}$$

Early attempts were made by Lumley [130], Bolotnov et al. [18] and Domaradzki et al. [53]. More recently, Mizuno [143] studied the spectral energy budget equation based on a Fourier transform of the turbulent kinetic energy transport equation. However, when considering the nonlinear turbulent transport term, it is important to consider the triad interactions between different Fourier modes (scales), which cannot be expressed in terms of a Fourier velocity spectrum. For example, it can be recast in the form of triadic wave interactions [33] or numerically approximated by a wavenumber differentiation [104, 103]. Lee and Moser [119] examined the large- and small-scale contributions to the turbulent kinetic energy transport equation based on a spectral filter. They examined the streamwise scale decomposition of turbulent kinetic energy production and provided statistical evidence of the interactions between the near-wall and outer turbulence as the large-scale modulation

of the near-wall turbulence. Kawata and Alfredsson [104] proposed an inter-scale transport equation (see §2.2.3), and using the Fourier mode decomposition on the Reynolds stress transport equations for plane Couette flow, they reported the small-scale dependence of Reynolds shear stress for large-scale structures. Although the spectral equations can be obtained using a number of different approaches [119, 33, 104] and have taken on a number of different forms, the evidence of inverse energy transfer from small scales to large scales is presented.

2.2 Fundamental flow analysis

In this section we review some flow analysis approaches presented in the literature. More thorough derivations can be found in the Appendix section for the readers' information.

2.2.1 Governing equations

The governing equations are the incompressible Navier–Stokes equations:

$$\frac{\partial u_i}{\partial t} + u_k \frac{\partial u_i}{\partial x_k} = -\frac{1}{\rho}\frac{\partial p}{\partial x_i} + \nu \Delta u_i. \tag{2.32}$$

As defined previously in (2.3), the instantaneous velocity (and pressure) components can be decomposed into time-averaged and fluctuating components

$$u_i(\boldsymbol{x},t) = \overline{u}_i(\boldsymbol{x}) + u_i'(\boldsymbol{x},t). \tag{2.33}$$

Alternatively, the instantaneous velocity (and pressure) components can be decomposed into a slightly general form, which includes (2.33) as a special case [41, 153, 42]

$$u_i(\boldsymbol{x},t) = \overline{u}_i(\boldsymbol{x}) + u_i'(\boldsymbol{x},t) = \underbrace{\langle u_i \rangle(x,y)}_{U_i(x,y)} + \underbrace{u_i'(\boldsymbol{x},t) + \tilde{u}_i(\boldsymbol{x})}_{u_i''(\boldsymbol{x},t)}, \tag{2.34}$$

when spanwise heterogeneity is not negligible and is sometimes called triple decomposition [29]. The $\langle\cdot\rangle$ denotes the global mean in the spanwise direction and in time. In the triple

decomposition (2.34), u_i'' denote the total fluctuations, u_i' are the turbulent fluctuations and $\tilde{u}_i$ are the coherent fluctuations due to spanwise inhomogeneity. The incompressible Navier–Stokes equations relate all extensive properties of a flow system and contain all the kinematic information on the system, e.g. the Reynolds stress and turbulent kinetic energy transports. Different flow analyses can be directly derived based on the incompressible Navier–Stokes equations and the decomposition schemes (2.33) and (2.34).

2.2.2 Fukagata–Iwamoto–Kasagi identity

The skin friction generation in ZPG TBLs, channel and pipe flows associated with turbulent coherent structures has been investigated through different approaches. The total skin friction coefficient is defined as $C_f = \tau_w/(\rho U_\infty^2/2)$ where τ_w, ρ and U_∞ are the mean wall shear stress, fluid density and free-stream velocity. Different skin friction decomposition methods have been proposed for the investigations of mean skin friction contributions in wall-bounded turbulent flows. They are based on the mean momentum, mean kinetic energy and vorticity transports [66, 167, 220].

The Fukagata–Iwamoto–Kasagi (FIK) identity relates the skin friction coefficient to dynamic effects that contribute to the mean wall-shear stress for plane flows, based on the basic equations for the mean momentum transport of turbulent flows (i.e. RANS). The FIK identity explicitly relates the Reynolds shear stress and other mean effects on the generation of mean skin friction [66]. The FIK identity has been widely used to provide a quantitative discussion of the skin friction generation mechanism in incompressible flow control studies of wall-bounded flows. Fukagata and Kasagi [68] studied the sub-optimal control law in drag-reduced pipe flows. They showed that the direct opposite control of near-wall Reynolds shear stress could achieve a drag reduction of approximately 11%, based on the analysis of the FIK identity. Stroh et al. [195] studied the opposite wall-normal velocity imposed on the near-wall region in TBL in comparison with fully-developed channel. Using FIK identity, they found that the spatial development effect contributes to the drag reduction in TBL, as, compared with the fully-developed channel, the skin friction is solely governed by the Reynolds shear stress. Hou et al. [87] studied skin friction decomposition

using an extended analysis of the polymer stress balance in polymer drag-reduced flows. They revealed the important role of the polymer stresses in contributing to the skin friction in the drag-reducing region in uniform polymer-injected channels and inhomogeneous TBLs. Kametani and Fukagata [100] studied the uniform blowing and suction in drag-reduced ZPG TBL and concluded that the mean convection is the decisive factor in the skin friction variation. Türk et al. [208] studied the dynamic contributions of friction drag over superhydrophobic surfaces in channel flows by considering the change in bulk velocity in terms of the average slip wall velocity and Reynolds shear stress. Experimental studies also developed concepts based on the FIK identity, such as the drag-reducing flow with surfactant additives [221] and developed a new experimental fit $(1-y/\delta)$ to the total shear stress profile in ZPG TBL [86]. For steady and two-dimensional TBL, the RANS in the streamwise direction can be reduced to

$$0 = \frac{\partial}{\partial y}\left[\overline{u'v'} - \frac{1}{Re_\delta}\frac{\partial \bar{u}}{\partial y} + \bar{u}\bar{v}\right] + \bar{I}_x, \tag{2.35}$$

where $\bar{I}_x$ denotes the spatial development term and is given by

$$\bar{I}_x(\boldsymbol{x}) = \frac{\partial \bar{p}}{\partial x} + \frac{\partial \bar{u}\bar{u}}{\partial x} - \frac{1}{Re_\delta}\frac{\partial^2 \bar{u}}{\partial x^2} + \frac{\partial \overline{u'u'}}{\partial x}. \tag{2.36}$$

By a triple integration of the RANS, the FIK identity is given by (Appendix A)

$$\begin{aligned} c_f(x) = {} & \underbrace{\frac{4(1-\delta_d)}{Re_\delta}}_{\text{DT}} + \underbrace{\frac{4}{U_\infty^2}\int_0^1 (1-y/\delta)(-\bar{u}\bar{v})\, d(y/\delta)}_{\text{MC}} \\ & + \underbrace{\frac{4}{U_\infty^2}\int_0^1 (1-y/\delta)(-\overline{u'v'})\, d(y/\delta)}_{\text{RS}} - \underbrace{\frac{2}{U_\infty^2}\int_0^1 \delta(1-y/\delta)^2\, \bar{I}_x\, d(y/\delta)}_{\text{SD}}, \end{aligned} \tag{2.37}$$

where $\delta_d = \int_0^1 (1-\overline{u}/U_\infty)\, d(y/\delta)$ is the dimensionless displacement thickness and other terms in the FIK identity are non-dimensionalised with δ and free-stream velocity U_∞. The four terms on the right side of (2.37) represent the net contribution to skin friction due to the laminar effect of the evolving boundary layer thickness (DT); the mean convection (MC)

as the mean effect of the motion-bearing mean streamwise velocity being advected by the mean wall-normal velocity; the turbulent contribution from the weighted Reynolds shear stress (RS) and the contribution from the spatial-derivatives of the streamwise velocity component (SD). It is also noteworthy that the RS evaluates the contribution from Reynolds shear stress with a weight function $(1 - y/\delta)$ that decreases linearly with increasing y, assigns more importance to the Reynolds shear stress in the region closer to the wall, and less importance to the region located further away from the wall. Recent studies have demonstrated the importance of the large-scale coherent structures in turbulent skin friction generation [49, 48, 55]. In paper 2, the FIK identity was used to investigate the universal skin friction behaviour of turbulent boundary layers modified by large-eddy-break-up devices. For flow control studies, the turbulent skin friction generation was examined in the framework of quadrant analysis of Reynolds shear stress [110, 28], because the literature hints that the mechanism responsible for generating skin friction can be linked to the existence of coherent structures that compose ejection and sweep events [95, 185, 4, 3, 126, 127]. In paper 3, the LEBU flows and the FIK identity were further explored based on the spectral analysis, to investigate the energy contribution of the large- and small-scale turbulence on the skin friction drag, following similar approaches by Deck et al. [49] and Duan et al. [55]. A scale decomposition based on the quadrant analysis of Reynolds shear stress was proposed, where the influence on skin friction drag of large- and small-scale sweep and ejection events was examined.

2.2.3 Fourier mode decomposition of Reynolds stresses transport

Spectral analysis is commonly employed to study wall-bounded turbulence. A recent development is the investigation of large- and small-scale interactions based on Reynolds stress transport and spectral decomposition [143, 104, 33, 119] due to the growing body of evidence that large-scale interference by the structures away from the wall occurs in the smaller-scale structures at the near-wall region [91, 92, 139]. An analytical approach for the investigation of large-scale and small-scale Reynolds stresses transports and their interactions was demonstrated by Kawata and Alfredsson [104] for plane Couette flow.

A scale decomposition based on the spanwise Fourier mode and a cut-off length scale $\lambda_z = 2\pi/k_z$ can be used to separate the total velocity fluctuations (i.e. denoted by " in (2.34)) into large-scale ($u_i''^{,\mathrm{L}}$) and small-scale components ($u_i''^{,\mathrm{S}}$) as

$$u_i''(\boldsymbol{x},t) = u_i''^{,\mathrm{L}}(k_z,\boldsymbol{x},t) + u_i''^{,\mathrm{S}}(k_z,\boldsymbol{x},t). \tag{2.38}$$

For steady and incompressible flow ZPG TBL, the large-scale Reynolds stress transport equations are given by

$$\frac{D\langle u_i''^{,\mathrm{L}} u_j''^{,\mathrm{L}}\rangle}{Dt}(k_z,x,y) = P_{ij}^{\mathrm{L}} + D_{ij}^{t,\mathrm{L}} + \phi_{ij}^{\mathrm{L}} + D_{ij}^{\nu,\mathrm{L}} - \epsilon_{ij}^{\mathrm{L}} - Tr_{ij}, \tag{2.39}$$

and the small-scale transport equations are obtained in a similar manner

$$\frac{D\langle u_i''^{,\mathrm{S}} u_j''^{,\mathrm{S}}\rangle}{Dt}(k_z,x,y) = P_{ij}^{\mathrm{S}} + D_{ij}^{t,\mathrm{S}} + \phi_{ij}^{\mathrm{S}} + D_{ij}^{\nu,\mathrm{S}} - \epsilon_{ij}^{\mathrm{S}} + Tr_{ij}. \tag{2.40}$$

This result was first given by Kawata and Alfredsson [104]. We provide a derivation of the equations in appendix B. The terms in the large-scale equations (2.39) are

$$\begin{aligned}
P_{ij}^{\mathrm{L}}(k_z,x,y) &= -\langle u_j''^{,\mathrm{L}} u_k''^{,\mathrm{L}}\rangle \frac{\partial U_i}{\partial x_k} - \langle u_i''^{,\mathrm{L}} u_k''^{,\mathrm{L}}\rangle \frac{\partial U_j}{\partial x_k},\\
\phi_{ij}^{\mathrm{L}}(k_z,x,y) &= -\frac{1}{\rho}\left[\langle u_j''^{,\mathrm{L}} \frac{\partial p''^{,\mathrm{L}}}{\partial x_i}\rangle + \langle u_i''^{,\mathrm{L}} \frac{\partial p''^{,\mathrm{L}}}{\partial x_j}\rangle\right],\\
D_{ij}^{\nu,\mathrm{L}}(k_z,x,y) &= \nu\frac{\partial^2}{\partial x_k^2}\langle u_i''^{,\mathrm{L}} u_j''^{,\mathrm{L}}\rangle, \quad \epsilon_{ij}^{\mathrm{L}} = 2\nu\left\langle \frac{\partial u_j''^{,\mathrm{L}}}{\partial x_k}\frac{\partial u_i''^{,\mathrm{L}}}{\partial x_k}\right\rangle,\\
D_{ij}^{t,\mathrm{L}}(k_z,x,y) &= -\frac{\partial}{\partial x_k}\left[\langle u_i''^{,\mathrm{L}} u_j''^{,\mathrm{L}} u_k''^{,\mathrm{L}}\rangle + \langle u_i''^{,\mathrm{L}} u_j''^{,\mathrm{L}} u_k''^{,\mathrm{S}}\rangle + \langle u_i''^{,\mathrm{S}} u_j''^{,\mathrm{L}} u_k''^{,\mathrm{S}}\rangle + \langle u_i''^{,\mathrm{L}} u_j''^{,\mathrm{S}} u_k''^{,\mathrm{S}}\rangle\right],\\
Tr_{ij}(k_z,x,y) &= \langle u_j''^{,\mathrm{L}} u_k''^{,\mathrm{L}} \frac{\partial u_i''^{,\mathrm{S}}}{\partial x_k}\rangle + \langle u_i''^{,\mathrm{L}} u_k''^{,\mathrm{L}} \frac{\partial u_j''^{,\mathrm{S}}}{\partial x_k}\rangle - \langle u_i''^{,\mathrm{S}} u_k''^{,\mathrm{S}} \frac{\partial u_j''^{,\mathrm{L}}}{\partial x_k}\rangle - \langle u_j''^{,\mathrm{S}} u_k''^{,\mathrm{S}} \frac{\partial u_i''^{,\mathrm{L}}}{\partial x_k}\rangle,
\end{aligned} \tag{2.41}$$

where, on the right-hand side of equations (2.39), are the large-scale production, turbulent transport, pressure transport, viscous transport, dissipation and the inter-scale flux [104]. All the terms in the small-scale equations (2.40) are obtained by interchanging the

superscripts L and S in (2.41). Note that Tr_{ij} in (2.39) and (2.40) are of opposite signs and therefore represent the local transfer between the large-scale $\left\langle u_i''^{,\mathrm{L}} u_j''^{,\mathrm{L}} \right\rangle$ and small-scale $\left\langle u_i''^{,\mathrm{S}} u_j''^{,\mathrm{S}} \right\rangle$ at the cut-off wavelength λ_z (or wavenumber k_z). The large-scale Reynolds stresses $\left\langle u_i''^{,\mathrm{L}} u_i''^{,\mathrm{L}} \right\rangle$ satisfy

$$\left\langle u_i''^{,\mathrm{L}} u_j''^{,\mathrm{L}} \right\rangle (k_z, y) = \int_0^{k_z} E_{ij}(K, y) dK, \quad \forall k_z, \tag{2.42}$$

where E_{ij} is the Reynolds stress tensor spectra. The spectral analysis of the Reynolds stress transport can be performed by differentiating (2.39) with respect to the cut-off wavenumber k_z,

$$\frac{DE_{ij}}{Dt}(k_z, x, y) = pr_{ij} + d^t_{ij} + \phi_{ij} + d^\nu_{ij} - \varepsilon_{ij} + tr_{ij}, \quad \forall k_z. \tag{2.43}$$

The terms in (2.43) are

$$\begin{aligned}
&pr_{ij}(k_z, x, y) = -\left[E_{jk} \frac{\partial U_i}{\partial x_k} + E_{ik} \frac{\partial U_j}{\partial x_k} \right], \quad \Phi_{ij}(k_z, x, y) = -\frac{1}{\rho} \frac{\partial}{\partial_{k_z}} \phi^{\mathrm{L}}_{ij}, \\
&d^\nu_{ij}(k_z, x, y) = \nu \frac{\partial^2 E_{ij}}{\partial x_k^2}, \quad \varepsilon_{ij}(k_z, x, y) = \frac{\partial}{\partial_{k_z}} \epsilon^{\mathrm{L}}_{ij}, \\
&d^t_{ij}(k_z, x, y) = \frac{\partial}{\partial_{k_z}} D^{t,\mathrm{L}}_{ij}, \quad tr_{ij}(k_z, x, y) = -\frac{\partial}{\partial_{k_z}} Tr_{ij}.
\end{aligned} \tag{2.44}$$

which can be interpreted as the spectral decomposition of the terms in the Reynolds stress transport equation. The approach was studied in a DNS dataset of ZPG TBL in paper 1 [27, p. 1-11]. Furthermore, we explored some ideas based on the spectral decomposed Reynolds stresses in paper 5 for the MVG flow control studies. In particular, the momentum transport of a turbulent boundary layer modified by the MVGs is investigated. This is in terms of the quadrant analysis of Reynolds shear stress. Then, the spanwise Fourier mode decomposition and triple velocity decomposition were utilised to study the MVG-induced flow modulation.

2.2.4 Triple velocity decomposition of Reynolds stress transport

The study of Reynolds stress (tensor) transport is of fundamental importance. Flows over spatial heterogeneous surfaces are commonly studied using triple velocity decomposition (2.34), where the total velocity fluctuation is further decomposed into turbulent and coherent fluctuations [41, 153, 42]. Flow that exhibits strong spanwise periodicity can be treated in a similar fashion, and thus in paper 4 we extend the analysis of kinetic energy transport of MVG by introducing triple velocity decomposition (2.34) to the steady and incompressible Navier–Stokes equations. The approach is similar to that of Reynolds and Hussain [168], where the transport equation for the turbulent kinetic energy is obtained by multiplying the turbulent velocity fluctuations u'_j and taking the time average; by interchanging i and j and summing up the resultant equation, the transport equation for turbulent kinetic energy is given by (Appendix C.2)

$$\begin{aligned}
&\frac{1}{2}\frac{\overline{\partial u_i' u_i'}}{\partial t} + \underbrace{\frac{U_k}{2}\frac{\overline{\partial u_i' u_i'}}{\partial x_k}}_{\mathcal{C}'(\boldsymbol{x})} = \underbrace{-\overline{u_i' u_k'}\frac{\partial U_i}{\partial x_k}}_{\mathcal{P}'(\boldsymbol{x})} + \underbrace{\tilde{u}_i\frac{\overline{\partial u_i' u_k'}}{\partial x_k}}_{\mathcal{T}(\boldsymbol{x})} \underbrace{-\frac{1}{\rho}\frac{\overline{\partial p' u_i'}}{\partial x_i}}_{\varphi'(\boldsymbol{x})} \\
&\underbrace{-\frac{1}{2}\frac{\partial}{\partial x_k}\left[\overline{u_i' u_i' u_k'} + \overline{u_i' u_i' \tilde{u}_k} + 2\overline{u_i' \tilde{u}_i u_k'}\right]}_{\mathcal{D}'(\boldsymbol{x})} + \underbrace{\frac{1}{2}\nu\overline{\Delta u_i' u_i'}}_{\mathcal{D}'_\nu(\boldsymbol{x})} \underbrace{-\nu\frac{\overline{\partial u_i'}}{\partial x_k}\frac{\partial u_i'}{\partial x_k}}_{\epsilon'(\boldsymbol{x})}.
\end{aligned} \tag{2.45}$$

Similarly, the MVG-induced (i.e. due to secondary motion) kinetic energy transport equation is obtained as (Appendix C.3)

$$\begin{aligned}
&\underbrace{\tilde{u}_i U_k\frac{\partial U_i}{\partial x_k} + \tilde{u}_i U_k\frac{\partial \tilde{u}_i}{\partial x_k}}_{\tilde{\mathcal{C}}(\boldsymbol{x})} = \underbrace{-\tilde{u}_i\tilde{u}_k\frac{\partial U_i}{\partial x_k}}_{\tilde{\mathcal{P}}(\boldsymbol{x})} \underbrace{-\tilde{u}_i\frac{\overline{\partial u_i' u_k'}}{\partial x_k}}_{\mathcal{T}(\boldsymbol{x})} \underbrace{-\frac{1}{2}\frac{\partial}{\partial x_k}\left[\tilde{u}_i\tilde{u}_i\tilde{u}_k\right]}_{\tilde{\mathcal{D}}(\boldsymbol{x})} \\
&\underbrace{-\frac{1}{\rho}\left[\frac{\partial P}{\partial x_i}\cdot\tilde{u}_i + \frac{\partial \tilde{p}}{\partial x_i}\cdot\tilde{u}_i\right]}_{\tilde{\varphi}(\boldsymbol{x})} + \underbrace{\nu\Delta U_i\cdot\tilde{u}_i + \frac{1}{2}\nu\Delta(\tilde{u}_i\tilde{u}_i)}_{\tilde{\mathcal{D}}_\nu(\boldsymbol{x})} \underbrace{-\nu\frac{\partial\tilde{u}_i}{\partial x_k}\frac{\partial\tilde{u}_i}{\partial x_k}}_{\tilde{\epsilon}(\boldsymbol{x})}.
\end{aligned} \tag{2.46}$$

We may rewrite (2.45) and (2.46) as

$$C' = \mathcal{P}' + \mathcal{D}' + \mathcal{T} + \varphi' + \mathcal{D}'_\nu - \epsilon', \tag{2.47}$$

and

$$\tilde{C} = \tilde{\mathcal{P}} + \tilde{\mathcal{D}} - \mathcal{T} + \tilde{\varphi} + \tilde{\mathcal{D}}_\nu - \tilde{\epsilon}, \tag{2.48}$$

where, on the right-hand side of equation (2.47), are the turbulent production, spatial transport, inter-component transport, pressure transport, viscous diffusion and dissipation. The terms in the equation (2.48) are the MVG-induced counterparts, which are decomposed from the turbulent fluctuations (2.47). The inter-component transport $\mathcal{T}$ in (2.47) and (2.48) are of opposite signs and represent a local exchange between turbulent ($\overline{u'_i u'_i}$) and MVG-induced ($\tilde{u}_i \tilde{u}_i$) kinetic energy. On the left-hand side of equation (2.48) is the advection term due to secondary motion. Adding up (2.47) and (2.48) yields the total kinetic energy transport equation (see also Appendix C.1)

$$C'' = \mathcal{P}'' + \mathcal{D}'' + \varphi'' + \mathcal{D}''_\nu - \epsilon'', \tag{2.49}$$

where $\partial(\cdot)/\partial t = 0$, and (2.49) collapses to the Reynolds-averaged turbulent kinetic energy transport equation, i.e. (2.21), when the coherent fluctuations $\tilde{u}_i$ approach zero. In paper 4, the triple decomposition of the kinetic energy transports was analysed. Simulation of an array of MVGs in a turbulent boundary layer was performed. The numerical study was motivated by the experimental investigations by Lögdberg et al. [125] and Fransson and Talamelli [65]. In the present study, the role that the mean flow plays in sustaining the secondary motions was examined. We also examined the influence of MVG on the large-scale coherent motions of a turbulent boundary layer using spectral analysis. The reader is referred to paper 4 for more information.

2.3 Flow control in turbulent wall-bounded flows

The aim of this section is to introduce the necessary background in order to provide a foundation for better understanding of the flow control methods in turbulent wall-bounded flows. Flow control methods can be categorised into active and passive flow controls with a particular emphasis on large-eddy break up devices and miniature vortex generators.

Control of turbulence by modifying the turbulent wall-bounded flows to reduce skin friction drag is of great importance and practical interest [14, 46]. The advancement in numerical simulations enables the flow control studies based on direct numerical simulation (DNS) and large-eddy simulation (LES), which advance our understanding of drag reduction mechanisms. Flow control strategies have been explored through active and passive means. A active flow control requires energy input with the aim of suppressing turbulence in order to achieve skin friction reductions [70]. For example, via uniform blowing and suction [156, 100], wall oscillation [99, 166] and opposite control [35, 107]. The passive flow control aims to suppress the formation or interaction of flow structures by introducing flow modulation effects (e.g. spanwise periodic flow) that propagates from the controlled flow region to the downstream region, which consists of a passive flow control arrangement and involves no energy input. It is, therefore, generally simpler to perform, such as by modifying the wall surfaces [25, 57, 69, 34, 96] or by addition of polymer solutions to the flows [221, 214].

Active flow controls

Using an active method with an efficient open- or closed-control loop system, it is possible to achieve significant skin-friction reduction. Examples are opposite control, wall blowing and suction (uniform or unsteady) and wall oscillation [70]. Choi et al. [35] examined the effectiveness of controls applied at the wall in reducing friction drag in turbulent channel flows. The aim was to suppress those quadrant events (ejections and sweeps) that are associated with the streamwise vortices via an opposite velocity component imposed at the wall, as shown in figure 2.1. This method resulted in up to 25% drag reduction. The control method requires sensors to be placed within $y^+ = 10$ from the wall, which seems to be

Figure 2.1: (a) Sensors plane location. (b) The opposite velocity control at the wall [35].

impractical; however, the results revealed that manipulation of the near-wall structure will lead to a substantial skin-friction drag reduction in wall-bounded flows. Subsequent studies based on the work of Choi et al. [35] include, for example, a neural network coupled with uniform blowing and suction [116]; sub-optimal control laws [117]; and near-wall streak control algorithms [58]. Recently, Kasagi et al. [102] reviewed the use of these feedback control algorithms, based on micro-electromechanical systems (MEMs) with flow sensors and actuators (figure 2.2), which attempted to modify the wall-surface shear stress and pressure fluctuations. For practical purpose, it is necessary to consider the turbulence scale separation as the Reynolds number increases. It is therefore required that the physical size and response time scale of the practical control system is comparable with the smallest scales of turbulent structures (i.e. in the order of $10\times$ viscous units), and it must be ensured that the requirements can be fulfilled by MEMS devices [102].

Studies of fluid injection and suction normal to a wall surface to suppress near-wall turbulence, such as by uniform blowing and suction (UB/US) using a spanwise localized slot (figure 2.3) in channels or spatially developing boundary layers, have also been investigated [e.g. 156, 111, 108, 100]. The work by Kametani and Fukagata [100] considered the contributions of skin-friction reduction in a turbulent boundary layer using a skin-friction decomposition proposed by Fukagata et al. [66] (as discussed in §2.2.2), which has provided a new point of view on the drag-decreasing mechanism by UB/US. Jung et al. [99] studied the high-frequency spanwise wall oscillation (where the wall moves in phase with a spanwise velocity (figure 2.4), which is a sinusoidal function of time (periodic) with a

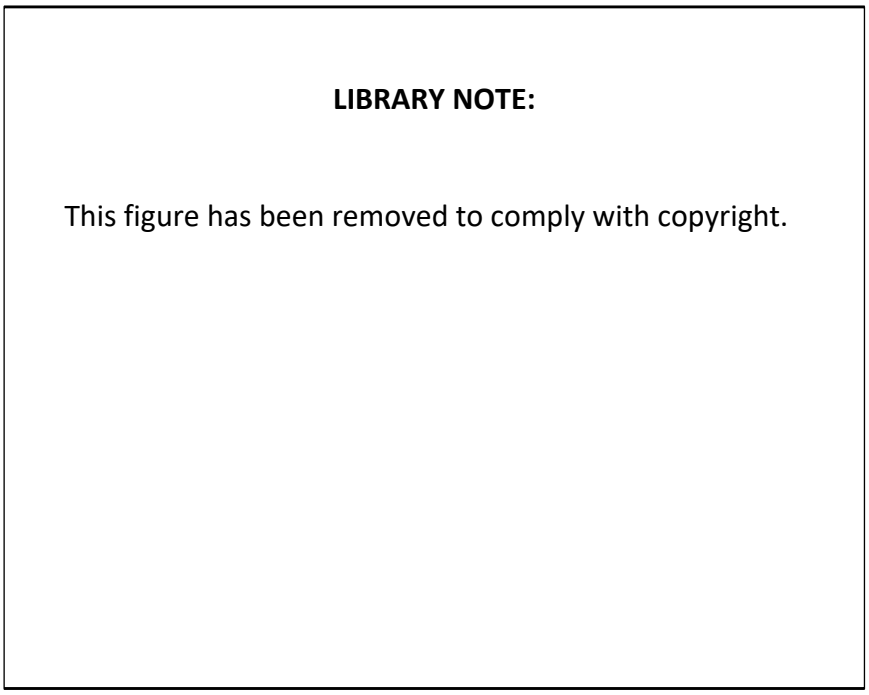

Figure 2.2: Examples of the micro-hot-film sensors and wall deformation actuators [171, 102].

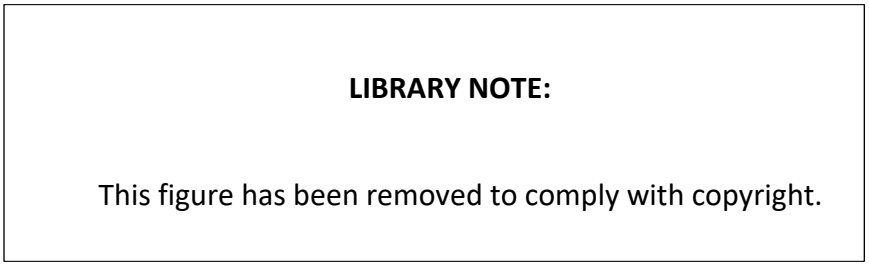

Figure 2.3: Schematic diagram of the computational domain by UB/US in Park and Choi [156] where W denotes the slot width.

no-slip condition applied to the streamwise direction and no-penetration applied to the wall normal direction). The spanwise oscillatory cross-flow or oscillatory channel wall results in weaker turbulence intensities and Reynolds shear stress [99] and leads to a sustained drag reduction of $10-40\%$.

In addition to the aforementioned studies of active flow controls, Schoppa and Hussain [184] proposed a control strategy that aims to suppress vortex formation and hence skin

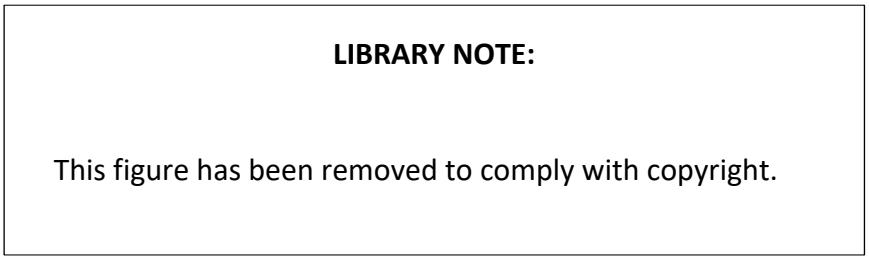

Figure 2.4: Schematic diagram of the wall boundary condition [99, 203].

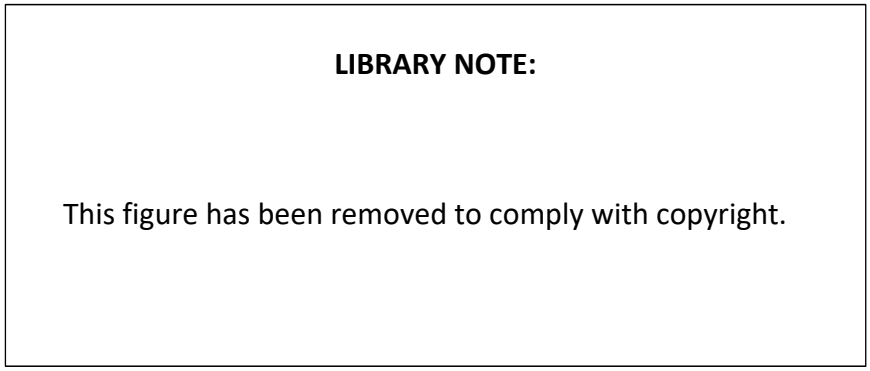

Figure 2.5: Schematic diagram of counter-rotating vortices in the spanwise section of a TBL. The box denotes the wall jet control region [184].

friction reduction using a spanwise row of counter-rotating streamwise vortices (figure 2.5). They reported a 20% sustained drag reduction when counter-rotating streamwise vortices were introduced to the flow; however, the drag reduction was argued to be a transient effect [22]. In a subsequent study [23], they investigated this control method using two sets of DNS with different Reynolds numbers (Re_τ = 360 and 550) and found that the large-scale vortices are able to efficiently provide drag reduction only at low Reynolds numbers (Re_τ = 360). The method seems to fail at the higher Reynolds numbers. In a subsequent study by Yao et al. [219], it was argued that the lack of drag reduction at higher Reynolds numbers conducted in Canton et al. [23] was due to the ineffective design of the large-scale control swirls.

Passive flow controls

Early experimental studies were mainly focused on riblets, polymer additives and outer-layer devices [14]. In the last three decades, various passive control studies involved

different types of methods, both experimentally and numerically, such as riblets [34, 96], superhydrophobic surfaces [135, 208, 94], compliant walls [25, 57, 69], wall deformations [152, 203], polymers or surfactant additives [221, 214] and large-eddy-break-up devices [193, 31]. From a practical viewpoint, surface modifications such as riblets, superhydrophobic surfaces, and compliant walls and wall deformations, might be the simplest way to achieve a skin-friction drag reduction. Choi et al. [34] studied flows over riblets using DNS (figure 2.6). The exposed surface to downwash motion associated with quasi-streamwise vortices was limited and the resultant drag reduction was approximately 6%. A superhydrophobic surface (SHS) consists of a thin-film hydrophobic coating with roughness pattern, where gas bubbles are trapped within the cavities of the coating, which provides a local free shear gas-liquid interface. Türk et al. [208] performed DNS in which the SHS (coating and gas-liquid interface) were modelled as alternating the no-slip and free-slip boundary conditions, proposed by Philip [163]. They proposed a prediction model that can estimate the gain from a SHS flow at high Reynolds numbers. A SHS study conducted by Jelly et al. [94] investigated in detail the transport of turbulent kinetic energy over the SHS texture. The TKE production, associated with the Reynolds shear stress, was significantly reduced over SHS in their study. Superhydrophobic surfaces may lead to a drag reduction of up to 75%, but in general the efficiency is limited and highly depends on the practical environment, such as high pressures and high shear rates [157]. Surface modifications can be made by compliant walls in which the wall surface acts like a tuned mass damper where momentum is transferred between compliant walls and fluids (figure 2.7), with the aim of delaying transition and suppressing the Reynolds shear stress at the near-wall region. However, the drag reduction by compliant surfaces in fully-developed flows remains uncertain. For example, Fukagata et al. [69] studied DNS channel flows over anisotropic compliant surface at the very low bulk velocity Reynolds number $Re_b = 3300$. They reported the skin friction was reduced by 8%; however, when the same parameters were applied to a larger domain, the compliant surfaces failed to achieve any skin friction reduction due to excessively large wall-normal velocity fluctuations [69].

Travelling-wave-like wall deformations have been demonstrated to re-laminarize the flow, which initiate a skin friction reduction, and the Reynolds shear stress are suppressed,

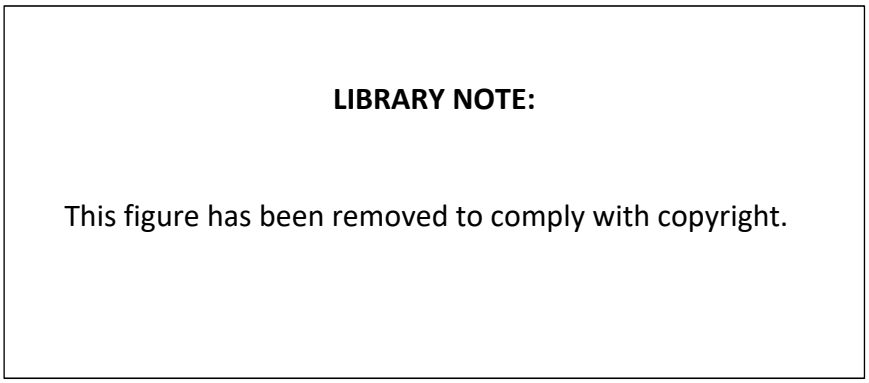

Figure 2.6: Riblet pattern for the DNS channel flow from Choi et al. [34].

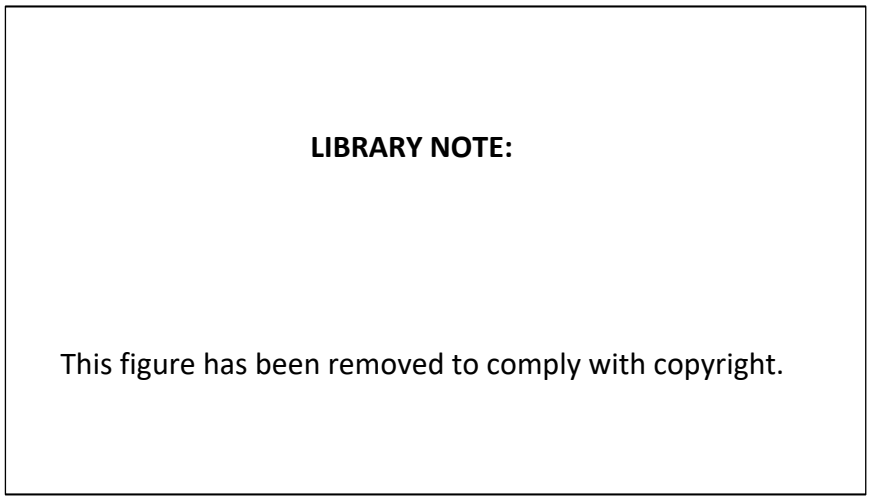

Figure 2.7: (a, b) Karmer's coating (left) and a simplified isotropic compliant wall model (right) [57]. (c, d) Grosskreutz's compliant wall (left) and an anisotropic compliant wall model (right) [25, 69].

downstream of the wave-like wall. For examples, see studies of streamwise wall deformation by Nakanishi et al. [152] and spanwise wall deformation by Tomiyama and Fukagata [203] (figures 2.8 and 2.9).

Research on the use of flow additives to achieve net drag reductions was originated by Toms [205] (also known as the "Toms effect"), as he found that the flow rate through a pipe increases if the concentration of polymer injected into a solvent increases. There

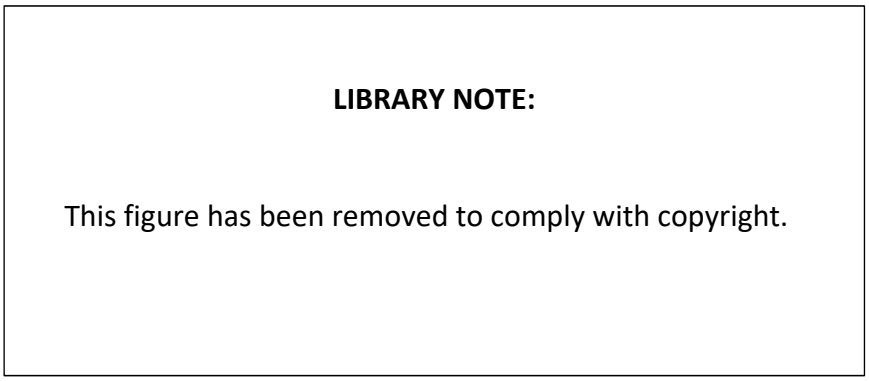

Figure 2.8: An example of streamwise wall deformation [152].

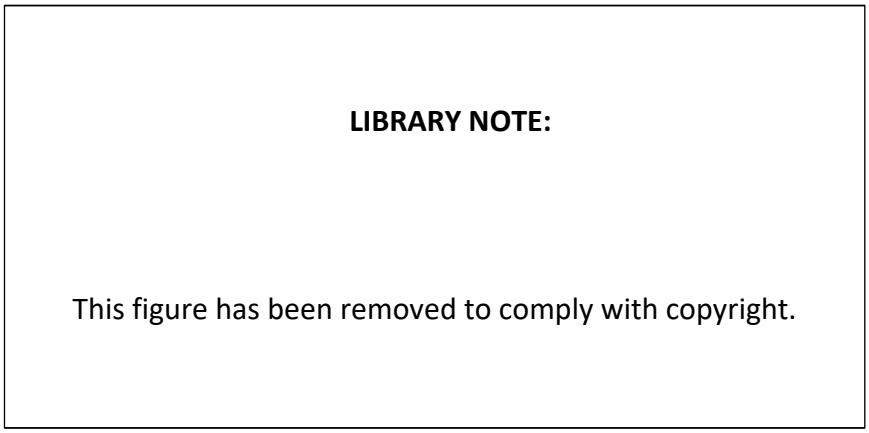

Figure 2.9: An example of spanwise wall deformation [203].

have been a large number of experimental and numerical studies on polymer additives, [e.g. 209, 51, 52, 214], which showed that substances directly interact with flows and dampen the quasi-streamwise vortices (known as polymer stress in Min et al. [141], as shown in figure 2.10). In addition to polymers additives, Yu et al. [221] utilised surfactant additives in order to obtain an insight into the mechanism of the Toms' effect phenomena.

Another category of passive control consists of thin plates or air-foils that are mounted in the outer part of a turbulent boundary layer [193, 31, 110], so-called outer-layer devices or large-eddy-break-up devices with the aim to disrupt the large coherent structures, which have attracted the interest of the engineering community [46]. The LEBUs were shown to be able to change the turbulent structure and intermittency, as well as to reduce skin friction drag. More recently, the miniature vortex generator is a similar candidate that

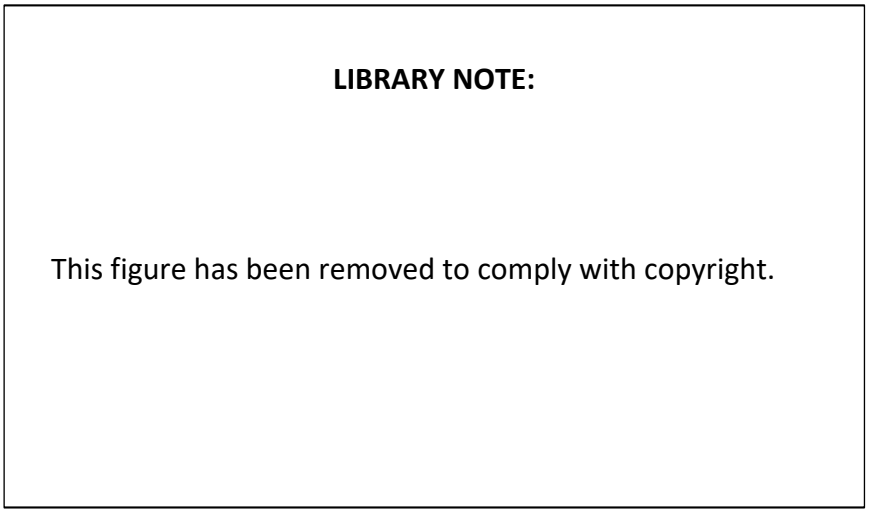

Figure 2.10: Schematic representation of the polymers' drag-reduction mechanism [141].

consists of pairs of winglets or rectangular blades, mounted on the wall and arranged in a spanwise oriented array, which show a very efficient drag reduction rate up to 65% in laminar boundary layers [189]. Because the works in this thesis are based on the LEBU device and MVG and there have been a great number of investigations into these two topics, in the following section, we review a collection of important studies that are particularly relevant to the present work.

Large-eddy break up devices

Attempts to achieve viscous drag reduction in turbulent boundary layers by altering the outer-layer large-scale flow structures have a long history [5, 46]. The early works on LEBU devices date back to the 1970s by Yajnik and Acharya [217], Corke et al. [44], Corke et al. [45], Anders et al. [9] and Hefner et al. [82]. The comprehensive studies conducted by Corke et al. [44] and Corke et al. [45] demonstrated that the net drag reductions can measure up to $15-20\%$. However, later studies showed that no net drag reduction can be achieved [172, 173, 133].

Sahlin et al. [173] studied the performance of airfoil-shaped LEBU devices in turbulent boundary layers over a range of chord length Reynolds numbers from 76 000 to 260 000. The total drag of the test plate and the device drag of the LEBUs were obtained indepen-

dently by several force gauges mounted at different locations of the towing tank. They focused on various parameters that may influence the performance of the LEBU devices. They reported a number of different configurations and results based on angles of attack from $-2°$ to $1°$ and wall-normal locations from $0.4\,\delta$ to $0.9\,\delta$, where δ is the boundary layer thickness, for single and tandem configurations. The maximum skin friction reduction was found to be 5%. However, no net drag reduction can be observed. They also demonstrated that a larger skin friction reduction will result in a higher device drag, so each nearly cancels the other out. Anders [8] assessed the performance of airfoil-shaped LEBU devices in a turbulent boundary layer developed on an axisymmetric body, and compared their drag reduction performance in relatively low and high Reynolds numbers. The chord length based Reynolds number ranges from 32 000 to 320 000 and the momentum thickness based Reynolds number Re_θ ranges from 2500 to 18 000. Of all the Reynolds numbers considered, the LEBU devices increased the total drag by $1-5\%$. However, they found that the device drag reduction mechanism seems to be associated with increasing Reynolds numbers. They thus suggested that this is due to the separation of scales at high Reynolds numbers. Lynn et al. [133] conducted a series of wind tunnel experiments to compare conventional thin blade and airfoil shaped LEBU devices (figure 2.11). Two drag balance plates were used separately to measure the skin friction drag on the flat plate and the LEBU device drag. They found that both thin blade and wire type LEBU devices increase the overall drag and they concluded that no net drag reduction was achievable. To explain the magnitudes and shapes of the observed skin-friction distributions in earlier studies of outer-layer devices, Savill and Mumford [177] conducted a series of flow visualisation experiments evaluating the impact of device height, length, thickness and separation between devices (for tandem arrangements) on the drag reduction performance of the LEBU devices (figure 2.12). They suggested that the principal mechanism for drag reduction is related to a sequence of active and interactive events between the wake vortices generated from the manipulators and the near-wall structure in the boundary layer.

Although the possibility of reducing viscous skin friction drag by LEBU devices in practical applications seems to be unlikely given the negative results that are presented in the earlier studies, there is growing interest in LEBU devices due to the possibility of

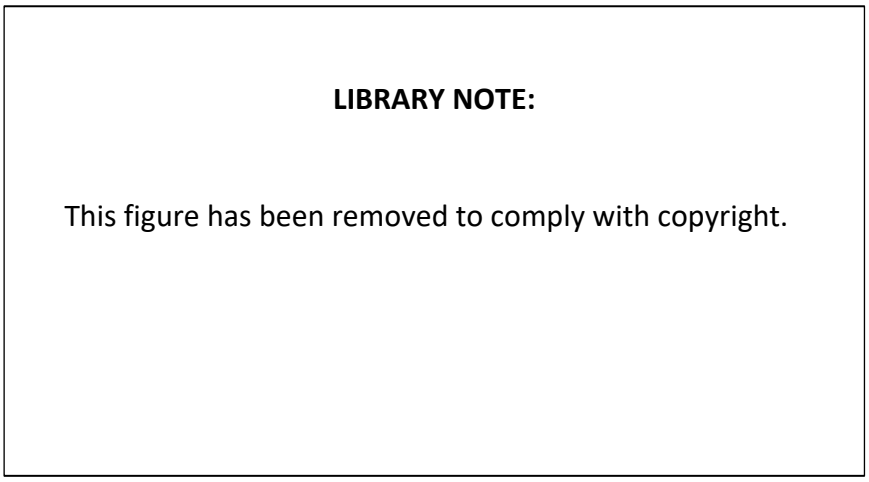

Figure 2.11: Schematic of the testing section of the LEBU device conducted by Lynn et al. [133]. s is the streamwise spacing between manipulators. $x0$ is the streamwise location of the trailing edge of the first manipulator. d is the boundary layer thickness. T is the angle of attack. c is the chord length. h is the height above the test plate. t is the device thickness. e is the distance between the centre and the leading edge.

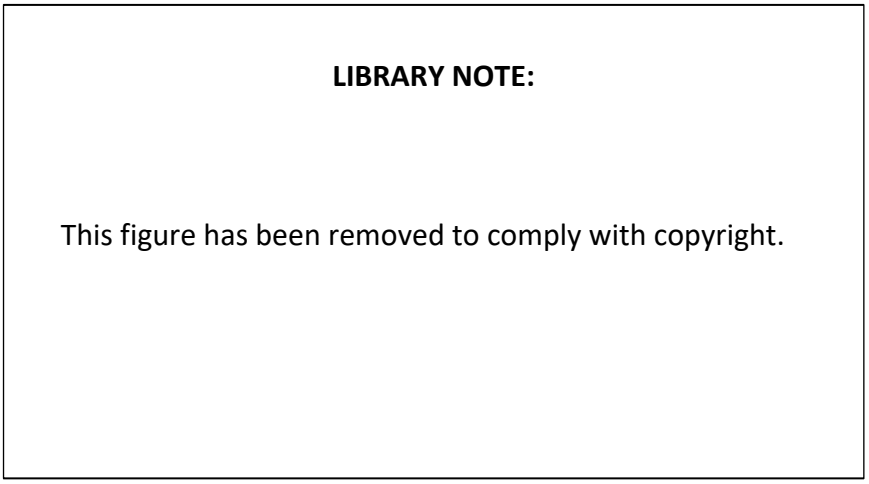

Figure 2.12: Flow visualisation of the downstream of the boundary layer manipulated by the single-plate device [177].

performing direct numerical and well-resolved large-eddy simulations of LEBU flows, where more detailed information about the flow is available. Recent studies have attempted to understand the underlying skin friction drag reduction mechanism based on advanced flow analysis techniques that were unavailable in the past [193, 31, 32], and which have

motivated the present study. Spalart et al. [193] investigated the effect of LEBUs on the levels of wall pressure fluctuation suppression of DNS of a TBL. They found that the LEBU can be used to reduce the intensities of pressure fluctuations by up to 30%, thereby regulating the induced noise. Chin et al. [31] performed LES to study the influence on flow structures of LEBU devices mounted in a ZPG TBL up to $Re_\theta = 4300$. Using spectral analysis of the velocity fluctuations, they provided evidence of the direct interactions between large-scale motions and the LEBU. In a subsequent study, Chin et al. [32] showed that the LEBU device is capable of attenuating the fluctuations of the turbulent/non-turbulent interface and thereby delaying the growth of the turbulent boundary layer. Kim et al. [110] performed DNS TBL to investigate the effect that LEBU have on the contribution of skin friction by Reynolds shear stress and by velocity-vorticity correlations. They found that the skin friction reduction can be interpreted as the effect of the advective vorticity transport and vortex stretching, which accounts for 80% of the skin friction reduction.

Miniature vortex generators

Passive flow control using a device-induced vortex is not new and has been studied intensively for many decades. In early studies, particular attention was paid to the flow separation control by using passive-type vortex generators [e.g. 198, 124, 123, 38] (i.e. without an energy input). The vane-type passive vortex generators (VGs) are conventional devices in a wide variety of shapes, sizes and types of arrangement, for controlling flow with height h of the order of the boundary layer thickness (δ) [123]. Generally speaking, $h/\delta \sim 1$ is referred to as conventional VGs, and $h/\delta \leq 0.5$ is referred to as low-profile VGs with the blade height just a fraction of the conventional VGs. Figure 2.13 shows examples of counter-rotating and co-rotating vane-type low-profile VGs, as well as the Wheeler's doublet and wishbone VGs from an investigation by Lin [122] which refers to them as "micro-VGs" with ratio $h/\delta \sim 0.2$. These devices are arranged in rows of pairs of small plates or airfoils, with an incidence angle with respect to the incoming flow direction, to generate pairs of counter-rotating or co-rotating streamwise trailing vortices. These types of VGs have been widely used for delaying boundary layer separation or to enhance aircraft wing performance [123, 76]. In addition to the standard vane-type VGs,

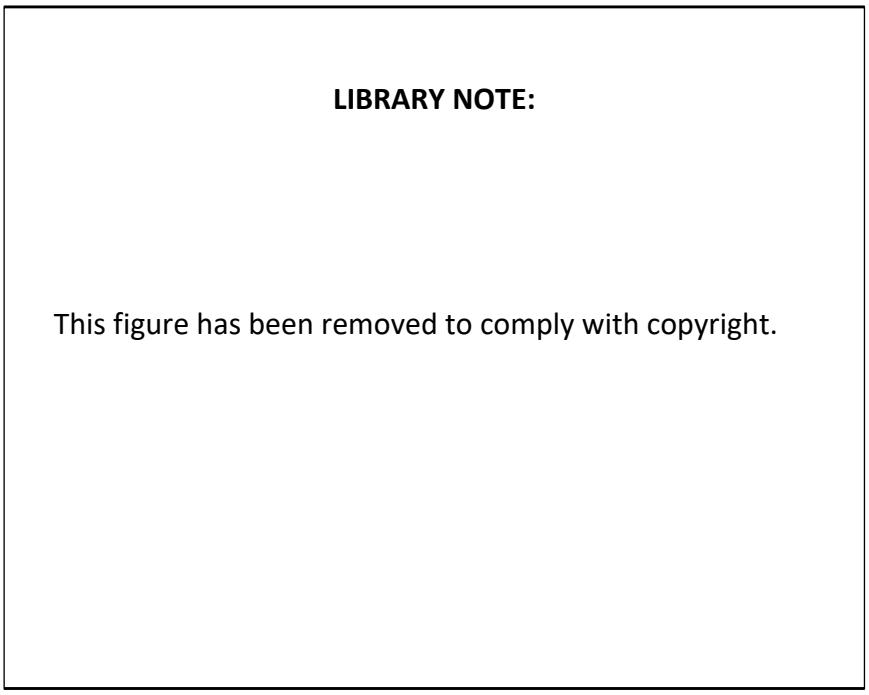

Figure 2.13: (a, b) Conventional vane-type VGs and (c, d) Wheeler's wishbone and doublet VGs. Device parameters are: h is the blade height, e is the blade length, T is the angle of attack and z is the spanwise separation [123].

various VGs consisting of counter-rotating triangular vanes, single triangular vanes and forwards and backwards wedges (see figure 2.14) were investigated in terms of vortex characteristics, such as the device-induced vortex strength (i.e. circulation) and its decay rate, both experimentally and numerically [10, 11]. Early studies that investigated a single low-profile vane-type VG placed within a turbulent boundary layer over a flat plate were conducted by Allan et al. [6] and Yao et al. [218]. However, the numerical studies were based on simplified turbulence and VG models. Lin [123] concluded in his review that there was a need to improve the numerical methods as well as the turbulence modelling in order to improve the VGs' simulations.

A VG-induced vortex-path model was proposed by Lögdberg et al. [125]. Their investigations were into the development of streamwise vortices introduced into the boundary layer by vortex generators, including the actual vortex propagation and vortex strength decay. Figure 2.15 shows the flow visualisation of the instantaneous (top) and averaged

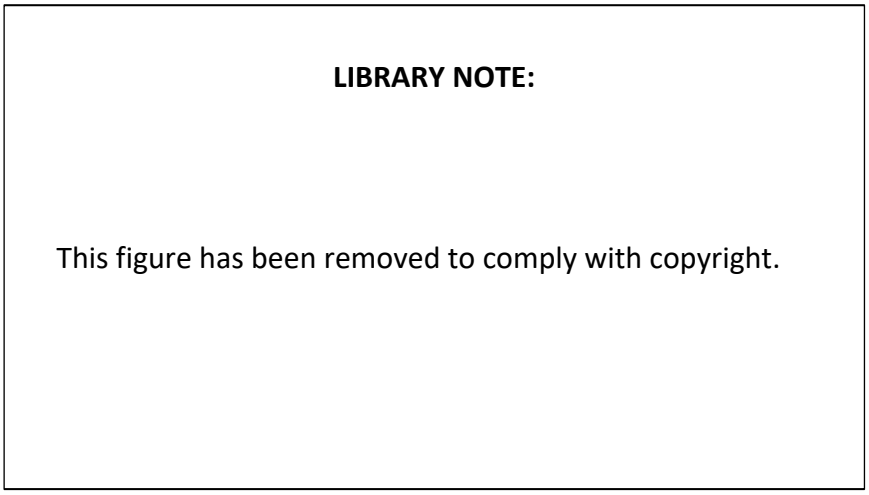

Figure 2.14: Geometry of low-profile VGs [123]. (a, c) Forwards and backwards wedges (ramp-like shape). (b, c) Counter-rotating vane and single vanes (triangular shape). Device sizes are scaled with the blade height h.

(bottom) flow patterns in which the light intensity indicates the paths of the vortex centres at the downstream locations of the VGs. Figure 2.16 shows the vortex centre paths projected on the spanwise-wall-normal plane moving downstream of a single VG pair (top) and an array of VG (bottom). The figure clearly reveals the influence of the vortex path due to the neighbouring vortex pair. By using a potential flow model, they proposed a vortex-path model predicting the streamwise evolution of longitudinal vortices downstream of the vortex generators.

As mentioned above, the original idea of VG was to delay or avoid flow separation in zero and adverse pressure gradient flows. Fransson et al. [64] investigated the use of cylindrical roughness elementsto generate streamwise vortices. The streamwise vortices develop into longitudinal streaks with the aim of suppressing the growth of Tollmien-Schlichting (TS) waves, which delay transition from laminar to turbulent flows and result in lower skin friction drag. Unfortunately, it was found that these surface elements might suffer from strong near-wake instability, which limits the element's ability to create stable, high amplitude, sinusoidal streaks [63–65]. The goal of the miniature vortex generator was

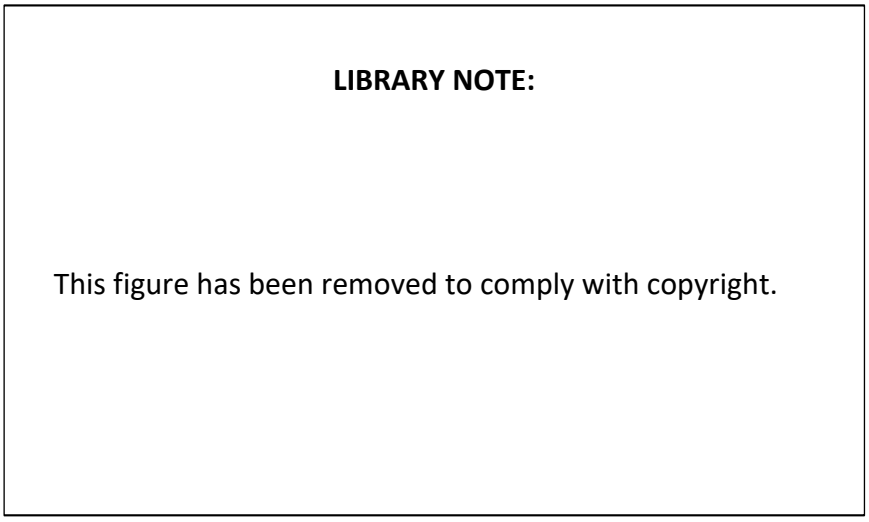

Figure 2.15: Instantaneous snapshots of the VG configurations conducted in Lögdberg et al. [125]. (a) A single pair of VG and (b) Multiple pairs of VG spaced in the spanwise direction. (c) and (d) are the corresponding averaged flow patterns. Dashed lines indicate the position of the maximum positive mean wall-normal velocity component [125]. $x0$ is the streamwise position of the VG and h is the blade height. D is the spanwise spacing between two pairs of VG

to replace the cylindrical roughness elements with the aim of generating high amplitude, stable streaks without initiating a near-wake instability [65, 189]. Fransson and Talamelli [65] explored the possibility of MVG generating stable streamwise streaks that stabilise TS waves for transition delay. They reported that the maximum amplitude of stable streaks was about 30% of the free-stream velocity, which is approximately a doubling of the value of that generated by circular roughness elements [64]. The modulation effect was sustained up to $700h$ downstream of the MVGs (where h is the blade height). A comprehensive parametric study of MVGs (triangular-bladed) optimisation was performed by Shahinfar et al. [187]. By using different MVG configurations, they optimised the streaks' scaling and improved the streak amplitude definition, by taking into consideration the spanwise periodicity of streaks. A DNS study by Siconolfi et al. [191] analysed the flow instabilities introduced by MVGs. An inadequate design of MVGs may amplify the TS waves and lead to faster transitions, which might be one of the drawbacks of MVGs [175].

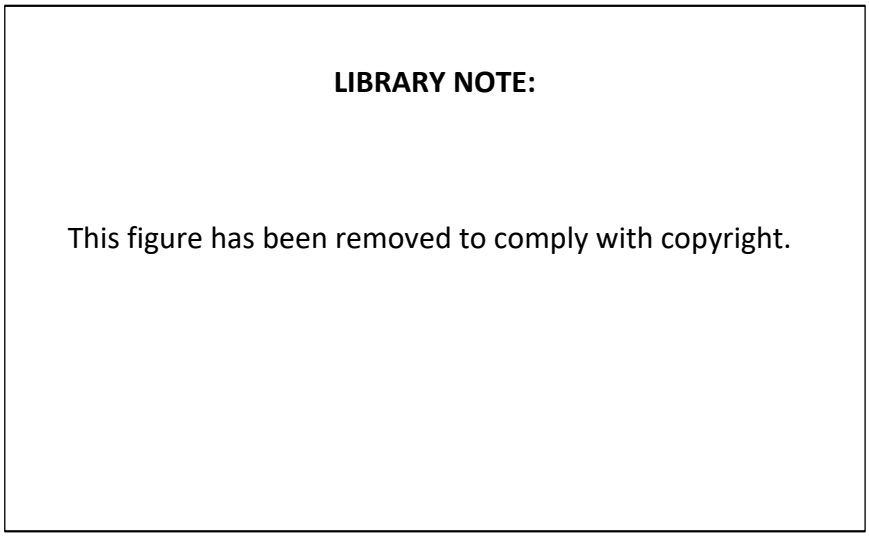

Figure 2.16: Streamwise evolution of the vortex centre plotted in a wall-normal–spanwise plane normal to the flow direction [125]. The vortex centre was tracked based on maximum absolute streamwise vorticity. ⋄, □ and ∘ denote three type of VGs with blade heights of 6mm, 10mm and 18mm, respectively [125]. (a) A single pair of VG and (b) Multiple pairs of VG spaced in the spanwise direction. Here h is the blade height and D is the spanwise spacing between two pairs of VG

The MVGs are small-scale with respect to the classical vortex generators, and from various studies mentioned previously it is known that the MVGs are applicable for laminar flows over flat plates to generate prolonged and organised streamwise-oriented streaks, which are able to stabilise the local flow disturbances and delay laminar flow transition [65, 188, 191], and potentially achieve a lower skin friction drag [189, 176]. Typically, the winglet and rectangular shaped MVGs were investigated. Figure 2.17 shows the experimental set-up of triangular-bladed MVG (left) applied on a flat plate from Shahinfar et al. [188] and (right) the rectangular-bladed MVG employed in Sattarzadeh et al. [176]. The rectangular-bladed MVG results in a higher streak amplitude compared with the same setup using triangular-bladed MVG [65, 187].

So far the majority of MVG studies in the literature have been focused on laminar or transitional boundary layer flows, and from various studies it is clear that the MVG is able to impose large-scale vortical motions and generate long high- and low-speed streaks into

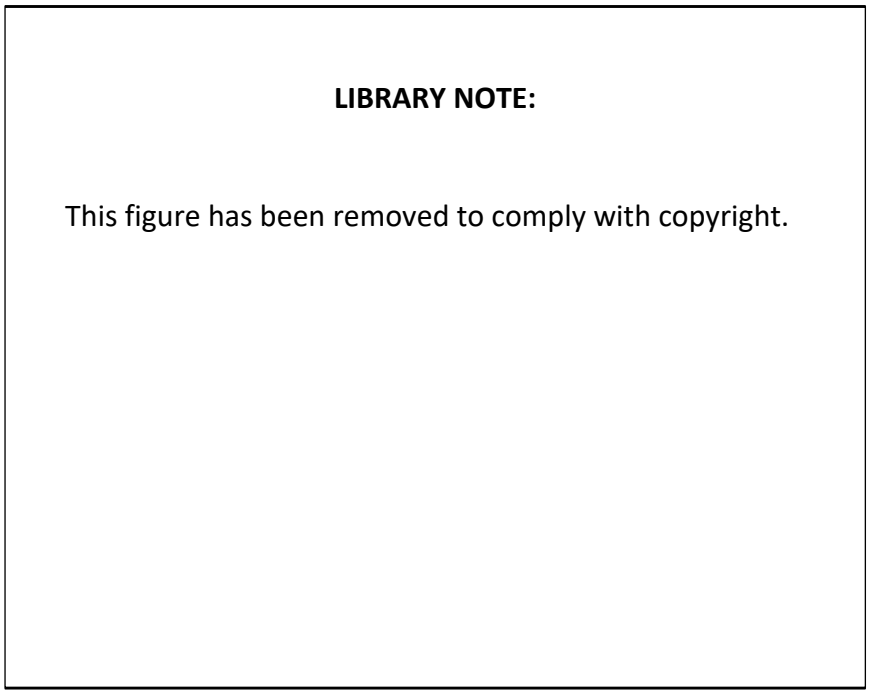

Figure 2.17: Examples of MVG geometry. (a) Triangular-bladed MVGs used in Shahinfar et al. [188]. Here, h is the blade height, L is the blade length, d is the spanwise separation between two blades, Λ is the spanwise spacing between two MVG pairs and x_{MVG} is the distance from the leading edge where the MVGs were located. (b) Rectangular-bladed MVGs used in Sattarzadeh et al. [176]. Here, θ is the angle of attack. x_{TS} is the location where the Tollmien-Schlichting wave is generated. x_{MVG}^{1st} denotes the location for the first MVG array and x_{MVG}^{2nd} denotes the location for the second MVG array.

the turbulent boundary layer by similar mechanisms. A challenge in controlling turbulent boundary layers is the existence of the different scales of naturally-occurring coherent structures in the different regions of the flow. When the Reynolds numbers increase, the very-large-scale features that consist of alternating low-speed and high-speed fluids appear and reside in the logarithmic region. They are known to modulate the near-wall structures and contribute to the mean Reynolds shear stress and skin friction drag. An aim here is therefore to investigate how the MVG-induced streaks evolve in a turbulent boundary layer

and how these streaks disturb the turbulent coherent structures in the near-wall and outer regions.

2.4 Background of the immerse boundary method

The study of fluid-structure interaction (FSI) problems, which consist of single or multiple elastic or rigid bodies interacting with fluid flows, is fundamental in many scientific and engineering applications. From a numerical perspective, depending on whether or not the Cartesian or cylindrical grid conforms to the geometry, the numerical approaches can be classified as either body-conforming or non-body-conforming methods [142, 85]. The body-conforming method often makes use of unstructured mesh for complex shapes, moving bodies, and a new fluid mesh must be regenerated in every time step, which increases the amount of memory and CPU time used. The non-body-conforming method is employed when the solid boundary conditions are modelled by modifying the governing equations, in which case the grid does not necessarily conform to the solid surfaces, which reduces computational costs. The immersed boundary method (IBM) is one of the approaches that is commonly employed [162]. In general, the modification takes the form of a forcing function in the governing equations that reproduces the solid boundary conditions.

2.5 Continuous forcing method

In general, there are two different ways to evaluate the forcing formulation in the IBM. Depending on whether or not the forcing function is discretised together with the governing equations, the force function implementation can be further categorised into the continuous forcing approach and the discrete forcing approach [142]. Some methods make use of the continuous forcing approach, for example, to represent an immersed elastic boundary where the boundary is modelled as a set of mass-less Lagrangian points with elastic springs connecting them, and the governing equations (e.g. incompressible Navier-Stokes equations) are solved on the uniform Cartesian grids. The total force applied by the

boundaries to the fluid was modelled as a local forcing term introduced in the momentum equations [162]

$$f_m(\boldsymbol{x},t) = \sum_n \boldsymbol{F}_n(t)\delta_d(|\boldsymbol{x} - \boldsymbol{X}_n(t)|). \tag{2.50}$$

Note that the Lagrangian boundary point ($\boldsymbol{X}_n$) does not necessarily coincide with the uniform grids ($\boldsymbol{x}$), therefore, δ_d is a smooth distribution function reminiscent of the Dirac delta function. The force $\boldsymbol{F}_n$ satisfies constitutive law, such as the Hooke's law, and is the force from the Lagrangian boundary point $\boldsymbol{X}_n$ acting on the surrounding fluid [142]. The location of the n^{th} Lagrangian boundary point moves with the local fluid velocity and the coordinate $\boldsymbol{X}_n$ representing the n^{th} Lagrangian point is governed by

$$\frac{\partial \boldsymbol{X}_n}{\partial t} = \boldsymbol{u}(\boldsymbol{X}_n,t). \tag{2.51}$$

This method is generally applied to elastic boundaries (and bodies) and was first demonstrated for blood flow modelling [161]. As discussed by Iaccarino and Verzicco [93], elastic boundaries modelling becomes complicated because the boundaries of the domain are moving and the force responses depend on the local flow conditions. If the boundary configuration is fixed and known, the calculation of the interaction between the fluid and the immersed surfaces becomes much simpler. The forcing function that represents a rigid boundary can be modelled using a feedback scheme [75, 174], which treats the forcing term as

$$\boldsymbol{F}(\boldsymbol{x}_s,T) = \alpha \int_0^T \big(\boldsymbol{u}(\boldsymbol{x}_s,t) - \boldsymbol{u}_s(\boldsymbol{x}_s,t)\big)dt + \beta\big(\boldsymbol{u}(\boldsymbol{x}_s,T) - \boldsymbol{u}_s(\boldsymbol{x}_s,T)\big), \tag{2.52}$$

by assuming that the grid nodes coincide with the immersed boundary, where $\boldsymbol{u}_s$ denotes a predefined velocity of the immersed boundary and $\boldsymbol{x}_s$ denotes the grid nodes' locations. In this expression, α and β are negative constants that usually require a parametric study [75]. It was shown that high values of α and β may lead to stability problems [75]. An alternative method to treat flows with rigid boundaries is called the penalty method. This method is based on the Navier-Stokes-Brinkman equations, which have an additional term

in the Navier-Stokes equations [105]:

$$\boldsymbol{F}(\boldsymbol{x},t) = \frac{\mu}{K(\boldsymbol{x},t)}\boldsymbol{u}(\boldsymbol{x},t), \tag{2.53}$$

assuming that the flow occurs in a porous medium, which is characterised by its permeability K. μ is the dynamic viscosity. The idea of this method is to model the fluid and solid regions by controlling the value of permeability, as $K \to \infty$ for the fluid region (i.e. the force vanishes $F \approx 0$) and therefore solve the classical Navier–Stokes equations, and as $K \to 0$ for the solid region (i.e. the force suppresses the flow), which is considered as a particular porous medium with a porosity $\phi \to 1$. A disadvantage of this method is that for a very small value of permeability K, the forcing term may increase the stiffness of the governing equations and thus affects the numerical stability, requiring smaller time steps, which is not practical for high Reynolds number simulations [142, 93]. In summary, the continuous forcing approach is useful for flows around bodies with immersed elastic and rigid boundaries because methods based on this approach are independent of the underlying spatial discretization, making them simpler to implement into an existing solvers. However, given that smoothing of the forcing function is needed, this approach prohibits a sharp representation of the immersed boundary as well as an accurate prediction of the fluid field near the immersed boundary.

2.6 Discrete forcing method

An alternative approach in IBM is the discrete forcing approach. Mohd-Yusof [144] developed the direct forcing method, which consists of an imposition of the velocity boundary conditions on the immersed surface, without requiring the introduction or computation of any forcing term. Thus, this method does not affect the numerical stability. In their approach, the force is explicitly defined and the appropriate boundary values are specified at the immersed surface

$$\boldsymbol{F} = \frac{\boldsymbol{u}_s - \boldsymbol{u}^n}{dt} + (\boldsymbol{u}\cdot\nabla)\boldsymbol{u} + \nabla p - \frac{1}{Re}\Delta\boldsymbol{u}, \tag{2.54}$$

by assuming that the immersed surface coincides with the node and a Dirichlet boundary condition $\boldsymbol{u} = \boldsymbol{u}_s$ is to be applied [144, 142, 93]. $\boldsymbol{u}^n$ is the n^{th} time iteration, the approximated solution of the discrete-time Navier-Stokes equations:

$$\boldsymbol{u}^n = \boldsymbol{u}^{n-1} + dt\Big((\boldsymbol{u}\cdot\nabla)\boldsymbol{u} - \nabla p + \frac{1}{Re}\Delta\boldsymbol{u}\Big), \tag{2.55}$$

where dt is the time step. Fadlun et al. [59] further extended the direct forcing method to a three-dimensional finite difference formulation on a staggered grid. The forcing was applied at the first Eulerian grid points external to the immersed boundary and the interface is sharply expressed by velocity reconstruction. The stability of the time integration remained unchanged with good quantitative agreement with experimental measurements. Finally, there have been a large number of numerical studies of discrete forcing IBM conducted over the last two decades; however, these studies are less relevant to this study and therefore the reader is referred to the provided appropriate sources. Major extensions of the discrete forcing IBM include Tseng and Ferziger [207], Zhang and Zheng [222], Balaras [13], Gilmanov et al. [74], Choi et al. [36], among others. Refinements of the discrete IBM can be found in Lee et al. [118], Li and Wang [120], Muldoon and Acharya [149], Kang et al. [101], Shinn et al. [190] and Gao et al. [73]. IBM has been studied extensively. For comprehensive reviews of the literature, the reader is referred to Peskin [162], Mittal and Iaccarino [142], and recent reviews by Kim and Choi [113] and Huang and Tian [89]. Overall, in contrast with the continuous forcing approach, forcing methods based on the discrete forcing approach do not require force smoothing and therefore enable a better representation of the immersed boundary. The discrete forcing approach does not restrict the computational time step associated with numerical stability, which is more practical for high Reynolds number flows compared with the continuous forcing approach. The disadvantage of the discrete forcing approach is that the force implementation becomes more difficult and less intuitive, and strongly depends on the temporal and spatial discretization schemes.

Chapter 3

Numerical methods

3.1 Large-eddy simulations

The numerical simulations presented in all the papers were performed using the fully spectral code (SIMSON) developed by Chevalier et al. [30] and were 2D parallelised running on $O(10^3)$ processors [121]. In papers 2-5, well-resolved (i.e. near wall well-resolved) large-eddy simulations were performed. Paper 1 was based on a direct numerical simulation data set. A sub-grid-scale approximate deconvolution model (ADM-RT) was employed to compute approximations to the unfiltered solutions by a repeated filter operation [181]. The governing equations are the resolved-scale incompressible continuity and Navier-Stokes equations:

$$\frac{\partial \hat{u}_i}{\partial x_i} = 0. \tag{3.1}$$

$$\frac{\partial \hat{u}_i}{\partial t} + \hat{u}_j \frac{\partial \hat{u}_i}{\partial x_j} + \frac{\partial \hat{p}}{\partial x_i} - \frac{1}{Re} \frac{\partial^2 \hat{u}_i}{\partial x_j \partial x_j} = -\chi H_N \circledast \hat{u}_i, \tag{3.2}$$

Here, x_i are Cartesian coordinates and $\hat{u}_i$ are the corresponding velocity components, i.e. the streamwise, wall-normal and spanwise directions, or simply x, y and z with corresponding velocities $\hat{u}$, $\hat{v}$ and $\hat{w}$. All variables are non-dimensionalised by the free-stream velocity U_∞, inlet displacement thickness δ_0^* and kinematic viscosity ν and give $Re_{\delta_0^*} = U_\infty \delta_0^* / \nu = 450$ ($Re_{\theta_0} = 180$). The relaxation term $-\chi H_N \circledast \hat{u}_i$: χ is the model coefficient; $H_N \circledast \hat{u}_i$ is the high-pass, approximately deconvolved quantities where $H_N :=$

$(I-G)^{N+1}$ is the high pass filter; G, N and I are the low-pass filter, deconvolution order and identity operator, respectively [detailed descriptions can be found in 194, 181]. This additional dissipative term damps out fluctuations near the cut-off wavenumber in order to improve the accuracy of the flow solution. The ADM-RT model has been found to be accurate and robust in predicting transitional and turbulent incompressible flows with spectral methods at momentum thickness Reynolds numbers Re_θ up to 4300 [181, 178, 56]. The spatial discretisation in the streamwise and spanwise directions uses a Fourier series with 3/2 zero-padding for de-aliasing in both directions, and the Chebyshev polynomial is employed in the wall-normal direction. Periodic boundary conditions are applied in the streamwise (x) and spanwise (z) directions, while a no-slip condition is applied at the wall, and a Neumann condition is applied in the free stream (upper boundary). A low-amplitude volume force trip is applied to the Navier-Stokes equations at the region very close to the inlet to trigger a rapid transition to turbulent flow. For further details on the simulations of DNS TBL with different numerical tripping methods, the reader is referred to Schlatter and Örlü [180]. To retain a periodic boundary condition in the streamwise direction, a fringe region is employed at the downstream of the flow, close to the end of the computational domain. In the fringe region, the flow is damped via a volume force until it returns to the inflow condition [30]. The fringe region technique is similar to that described by Bertolotti et al. [17]. The domain sizes were selected such that the two-point correlations in the horizontal directions would essentially be zero at maximum separation (i.e. at least half the domain size). Time advancement is carried out by a second-order Crank-Nicolson scheme for the viscous terms and a third-order four-stage Runge-Kutta scheme for the non-linear terms [30]. An overview of the flow control simulations and parameters is presented in table 3.1.

3.2 Flow geometry modelling

For the current study, the flow geometries (LEBU device and MVG) are modelled by introduction of an external volume force field to the Navier-Stokes equations (3.2). The implementation is based on the immersed boundary layer method proposed by Goldstein

Table 3.1: Flow control cases and simulation parameters: Reynolds numbers based on inlet displacement thickness, computational domain sizes, spectral collocation points and the corresponding papers.

Case	$Re_{\delta^*} = U_\infty \delta_0^* / \nu$	$(x_L \times y_L \times z_L)/\delta_0^*$	$N_x \times N_y \times N_z$	Paper
DNS	450	$10000 \times 300 \times 360$	$12800 \times 769 \times 1024$	1
LB01	450	$6000 \times 200 \times 240$	$6144 \times 513 \times 512$	2 and 3
LB05	450	$6000 \times 200 \times 240$	$6144 \times 513 \times 512$	2 and 3
LB08	450	$6000 \times 200 \times 240$	$6144 \times 513 \times 512$	2 and 3
MVG	450	$6000 \times 200 \times 360$	$6144 \times 513 \times 768$	4 and 5

et al. [75], where the method suppresses the flow velocity field to zero in the solid region of the flow geometry. The volume force can be written in the general form of

$$\boldsymbol{F}(\boldsymbol{x},T) = -\alpha\lambda(\boldsymbol{x})\boldsymbol{u}(\boldsymbol{x},T) + \beta \int_0^T \boldsymbol{u}(\boldsymbol{x},t)dt, \tag{3.3}$$

where λ is a non-zero smoothing function in the forcing region; α and β are constants that determine the forcing strength; T is the time scale of the volume force and $\boldsymbol{u}$ is the flow-field velocities. This method determines the force using direct and integral velocity feedback, and the force is applied to the Navier-Stokes equations at each time instant. The impact of sharp volume force at the geometry boundary is reduced by introducing a smoothing width similar to that used in Chin et al. [31]. The immersed boundary implementation of the MVG was carefully tested in a laminar (Blasius) boundary layer. Figures 3.1 and 3.2 display the instantaneous snapshots of the flow field past a single pair of MVG, conducted in a Blasius boundary layer simulation. The implementation of the LEBU device has been validated in previous studies by Chin et al. [31, 32]. The effectiveness of the volume force implementation in SIMSON has been demonstrated in many studies. For example, for modelling spanwise heterogeneous roughness [62, 186, 196], for implementation of large-scale vortices in channel flows [22, 23] and for modelling of LEBU devices [31]. For more specific information on the numerical set-up of LEBU devices and miniature vortex generators, the reader is referred to papers 2 and 4, respectively.

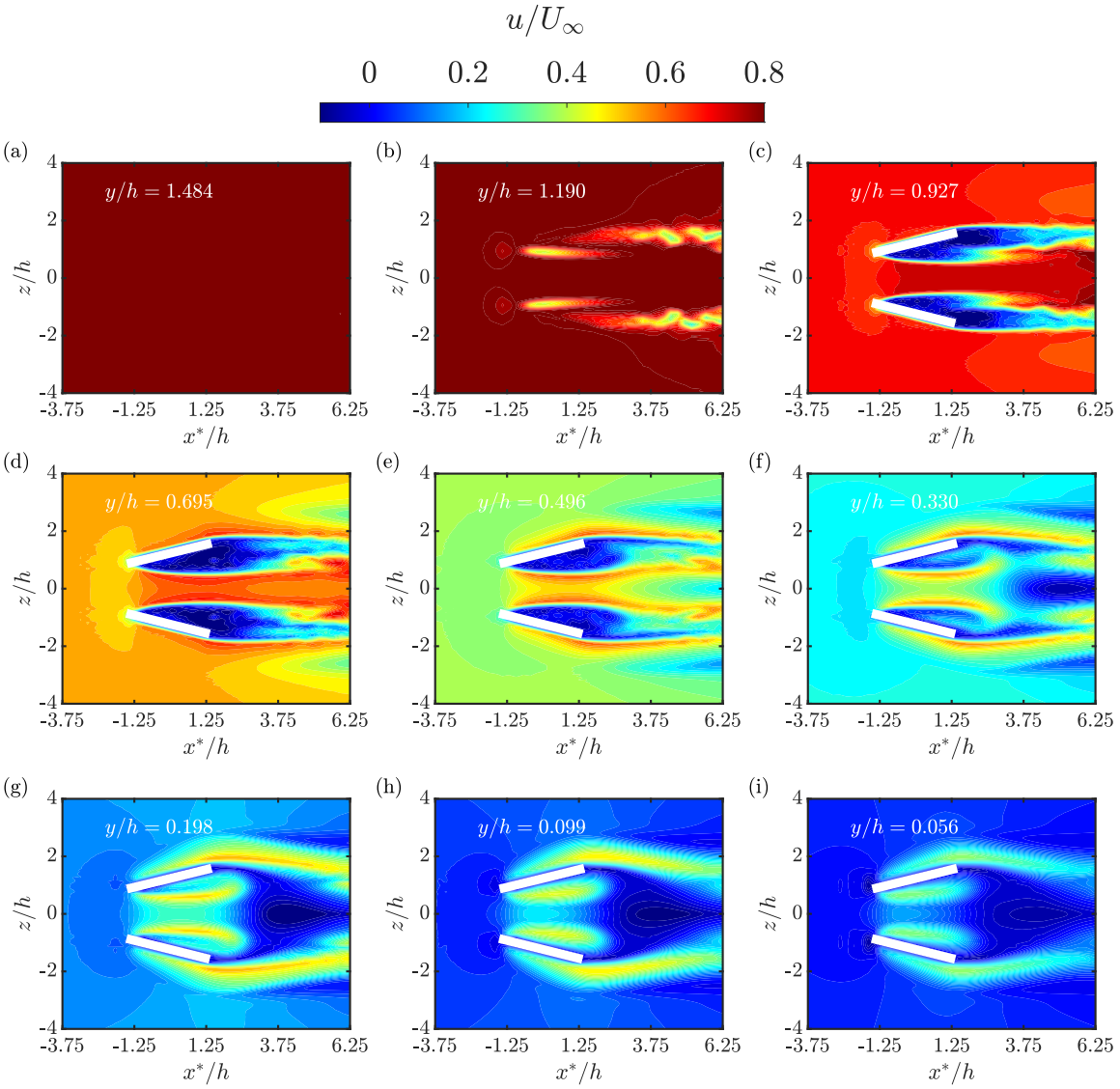

Figure 3.1: Contours of the instantaneous streamwise velocity of laminar boundary layer pasts MVG in the top view, with decreasing wall-normal distance from $(a)-(i)$, at time $TU_\infty/\delta^* = 1460$ (δ^* is the displacement thickness). Here, h is the MVG blade height, z and y are the spanwise and wall-normal directions, respectively. $x^* = x - x_{MVG}/h$ is the normalised streamwise coordinate where x_{MVG} is the streamwise location of the MVG. White rectangles denote the locations of the MVG geometry. In the laminar case, the inlet Reynolds number based on the displacement thickness and free-stream velocity is set to $Re_{\delta_0^*} = 450$ or $Re_x = (450/1.721)^2 = 68369$. The MVG pair is introduced at $Re_{\delta^*} \approx 1230$ or $Re_x \approx 510797$ ($x_{MVG} = 950\delta_0^*$).

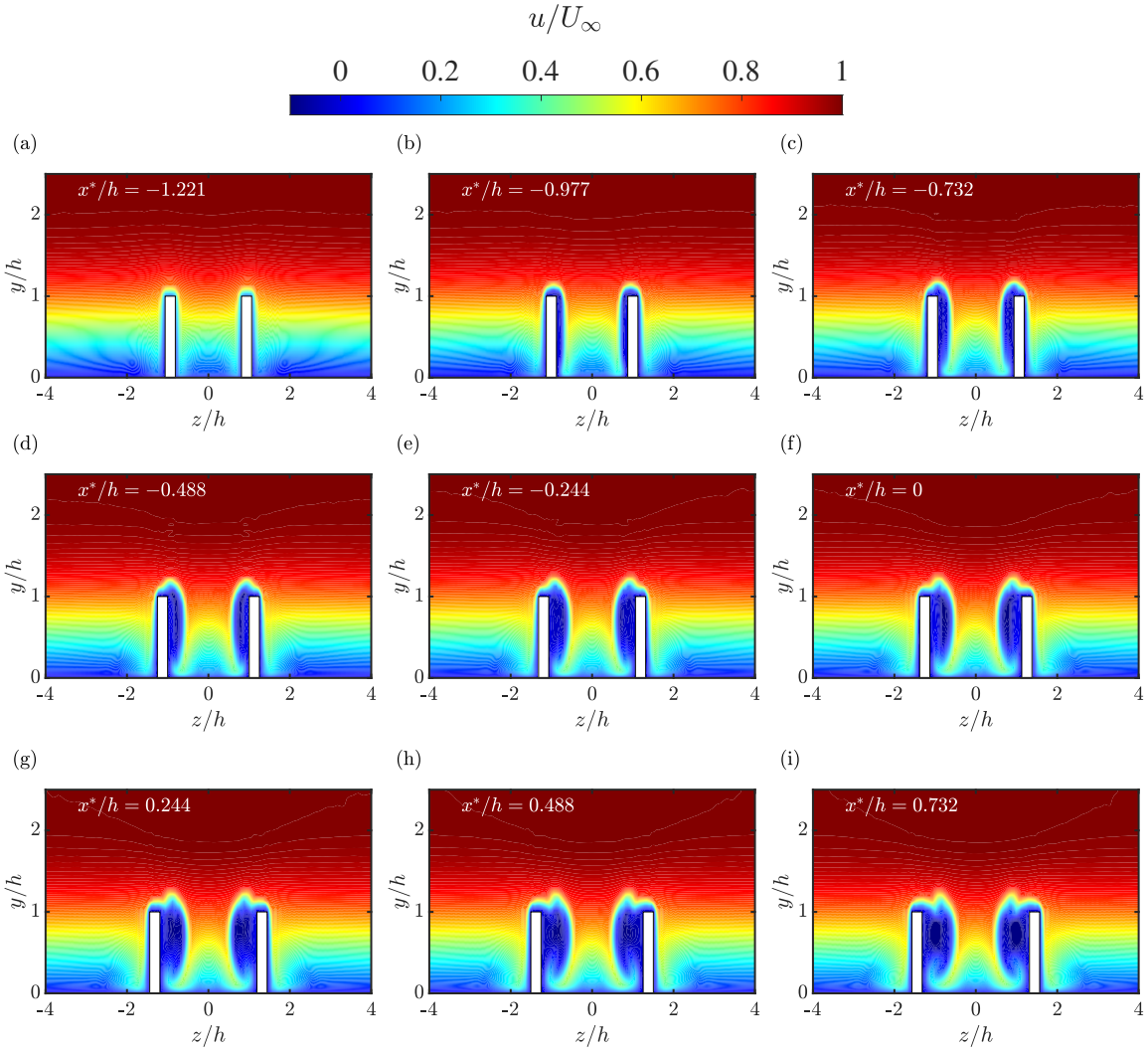

Figure 3.2: Cross-sectional contours of the instantaneous streamwise velocity in the front view moving downstream (laminar case). Black lines indicate the spanwise and wall-normal grid spacings. $x^*/h = 0$ is at the centre of the MVG pair.

Chapter 4

Paper

4.1 Paper 1

Introduction

In this work we extend the concept of scale-by-scale energy budgets to zero pressure gradient boundary layers, based on an innovative analytical approach. Spectral analysis based on the spanwise scale decomposition of the Reynolds stress transport equation is utilised to study a moderate Reynolds number turbulent boundary layer, with data obtained from a direct numerical simulation. This study aims to provide new insights into the spanwise scale interactions in a turbulent boundary layer and explore the differences from plane Couette flows.

Interscale transport mechanisms in turbulent boundary layers

This paper is published as: Chan, C. I., Schlatter, P. and Chin, R. C. (2021). Interscale transport mechanisms in turbulent boundary layers. *Journal of Fluid Mechanics*, 921, A13.

Statement of Authorship

Title of Paper	Interscale transport mechanisms in turbulent boundary layers
Publication Status	☑ Published ☐ Accepted for Publication ☐ Submitted for Publication ☐ Unpublished and Unsubmitted work written in manuscript style
Publication Details	Chan, C. I., Schlatter, P. and Chin, R. C. (2021). Interscale transport mechanisms in turbulent boundary layers. Journal of Fluid Mechanics, 921, A13.

Principal Author

Name of Principal Author (Candidate)	Chi Ip Chan		
Contribution to the Paper	Under the supervision of R. C, Chin and Schlatter P., I performed the simulations, interpreted and processed the data and wrote the manuscript.		
Overall percentage (%)	70		
Certification:	This paper reports on original research I conducted during the period of my Higher Degree by Research candidature and is not subject to any obligations or contractual agreements with a third party that would constrain its inclusion in this thesis. I am the primary author of this paper.		
Signature		Date	05 Jan 2022

Co-Author Contributions

By signing the Statement of Authorship, each author certifies that:

i. the candidate's stated contribution to the publication is accurate (as detailed above);

ii. permission is granted for the candidate in include the publication in the thesis; and

iii. the sum of all co-author contributions is equal to 100% less the candidate's stated contribution.

Name of Co-Author	Philipp Schlatter		
Contribution to the Paper	Helped in the development of the research, contributed in academic discussion and manuscript review		
Signature		Date	02/02/2022

Name of Co-Author	Rey Cheng Chin		
Contribution to the Paper	Supervised the development of the research, participated in developing ideas and concepts, helped in interpretation of results, provided critical revision of manuscript.		
Signature		Date	06/01/2022

Name of Co-Author			
Contribution to the Paper			
Signature		Date	

Name of Co-Author			
Contribution to the Paper			
Signature		Date	

LIBRARY NOTE:

The following article on pages 53-82 has been removed due to copyright.

It is also available online to authorised users at:
https://doi.org/10.1017/jfm.2021.504

4.2 Paper 2

Introduction

To further explore the applicability of large-eddy break up (LEBU) devices. In this work, we aims to complement the existing literature on the skin friction reduction mechanism of a LEBU device in a turbulent boundary layer. A skin friction decomposition procedure is utilised to study different physical mechanisms related to the observed skin friction reduction, including the effects of laminar flow, mean flow and turbulence upon the interaction between the flow and a LEBU device mounted at different wall-normal locations. The presented results demonstrate the universal behaviours of different contributions to the total skin friction reduction.

The skin-friction coefficient of a turbulent boundary layer modified by a large-eddy break-up device

This paper is published as: Chan, C. I., Örlü, R., Schlatter, P. and Chin, R. C. (2021). The skin-friction coefficient of a turbulent boundary layer modified by a large-eddy break-up device. *Physics of Fluids* 33, 035153.

Statement of Authorship

Title of Paper	The skin-friction coefficient of a turbulent boundary layer modified by a large-eddy break-up device
Publication Status	☑ Published ☐ Accepted for Publication ☐ Submitted for Publication ☐ Unpublished and Unsubmitted work written in manuscript style
Publication Details	Chan, C. I., Örlü, R., Schlatter, P. and Chin, R. C. (2021). The skin-friction coefficient of a turbulent boundary layer modified by a large-eddy break-up device. Physics of Fluids 33, 035153.

Principal Author

Name of Principal Author (Candidate)	Chi Ip Chan		
Contribution to the Paper	Under the supervision of R. C, Chin, Örlü, R. and Schlatter P., I performed the simulations, interpreted and processed the data and wrote the manuscript.		
Overall percentage (%)	70		
Certification:	This paper reports on original research I conducted during the period of my Higher Degree by Research candidature and is not subject to any obligations or contractual agreements with a third party that would constrain its inclusion in this thesis. I am the primary author of this paper.		
Signature		Date	05 Jan 2022

Co-Author Contributions

By signing the Statement of Authorship, each author certifies that:

i. the candidate's stated contribution to the publication is accurate (as detailed above);

ii. permission is granted for the candidate in include the publication in the thesis; and

iii. the sum of all co-author contributions is equal to 100% less the candidate's stated contribution.

Name of Co-Author	Ramis Örlü		
Contribution to the Paper	Helped in the development of the research, contributed in academic discussion and manuscript review.		
Signature		Date	06/01/2022

Name of Co-Author	Philipp Schlatter		
Contribution to the Paper	Helped in the development of the research, contributed in academic discussion and manuscript review.		
Signature		Date	02/02/2022

Name of Co-Author	Rey Cheng Chin		
Contribution to the Paper	Supervised the development of the research, participated in developing ideas and concepts, helped in interpretation of results, provided critical revision of manuscript.		
Signature		Date	06/01/2022

Name of Co-Author			
Contribution to the Paper			
Signature		Date	

LIBRARY NOTE:

The following article on pages 86-99 has been removed due to copyright.

It is also available online to authorised users at:
https://doi.org/10.1063/5.0043984

4.3 Paper 3

Introduction

This paper assesses the contributions of different scales to the skin friction reduction of a turbulent boundary layer modified by a LEBU device, based on a Fourier mode decomposition and spectral analysis. Large-scale and small-scale Reynolds shear stress events are defined based on the quadrant analysis, and their influence on the skin friction coefficient is explored through an extension of the skin friction decomposition scheme.

Large-scale and small-scale contribution to the skin friction reduction in a modified turbulent boundary layer by a large-eddy break-up device

This paper is submitted to *Physical Review Fluids* and accepted on 14 February for publication.

Statement of Authorship

Title of Paper	Large-scale and small-scale contribution to the skin friction reduction in a modified turbulent boundary layer by a large-eddy break-up device.
Publication Status	☐ Published ☑ Accepted for Publication ☐ Submitted for Publication ☐ Unpublished and Unsubmitted work written in manuscript style
Publication Details	Accepted for publication on 14 Feb 2022.

Principal Author

Name of Principal Author (Candidate)	Chi Ip Chan		
Contribution to the Paper	Under the supervision of R. C, Chin, Örlü, R. and Schlatter P., I performed the simulations, interpreted and processed the data and wrote the manuscript.		
Overall percentage (%)	70		
Certification:	This paper reports on original research I conducted during the period of my Higher Degree by Research candidature and is not subject to any obligations or contractual agreements with a third party that would constrain its inclusion in this thesis. I am the primary author of this paper.		
Signature		Date	05 Jan 2022

Co-Author Contributions

By signing the Statement of Authorship, each author certifies that:

i. the candidate's stated contribution to the publication is accurate (as detailed above);

ii. permission is granted for the candidate in include the publication in the thesis; and

iii. the sum of all co-author contributions is equal to 100% less the candidate's stated contribution.

Name of Co-Author	Ramis Örlü		
Contribution to the Paper	Helped in the development of the research, contributed in academic discussion and manuscript review.		
Signature		Date	06/01/2022

Name of Co-Author	Philipp Schlatter		
Contribution to the Paper	Helped in the development of the research, contributed in academic discussion and manuscript review.		
Signature		Date	02/02/2022

Name of Co-Author	Rey Cheng Chin		
Contribution to the Paper	Supervised the development of the research, participated in developing ideas and concepts, helped in interpretation of results, provided critical revision of manuscript.		
Signature		Date	06/01/2022

Name of Co-Author			
Contribution to the Paper			
Signature		Date	

4.4 Paper 4

Introduction

Vortex generators (VGs) have been widely used in flow control due to their ability to delay flow from transition to turbulence and to control flow separation in adverse pressure gradient boundary layers. In this work, we explore the flow characteristics of miniature vortex generators (MVGs) in turbulent boundary layers by means of spectral analysis. A novel triple decomposition approach to kinetic energy transport is used to investigate the source of the secondary motion.

Investigation of the influence of miniature vortex generators on the large-scale motions of a turbulent boundary layer

This paper is published as: Chan, C. I. and Chin, R. C. (2022). Investigation of the influence of miniature vortex generators on the large-scale motions of a turbulent boundary layer. *Journal of Fluid Mechanics*, 932, A29.

Statement of Authorship

Title of Paper	Investigation of the influence of miniature vortex generators on the large-scale motions of a turbulent boundary layer.
Publication Status	☑ Published ☐ Accepted for Publication ☐ Submitted for Publication ☐ Unpublished and Unsubmitted work written in manuscript style
Publication Details	Chan, C. I. and Chin, R. C. (2022). Investigation of the influence of miniature vortex generators on the large-scale motions of a turbulent boundary layer. Journal of Fluid Mechanics. 932, A29.

Principal Author

Name of Principal Author (Candidate)	CHI IP CHAN		
Contribution to the Paper	Under the supervision of R. C, CHIN, I performed the simulations, interpreted and processed the data and wrote the manuscript.		
Overall percentage (%)	70		
Certification:	This paper reports on original research I conducted during the period of my Higher Degree by Research candidature and is not subject to any obligations or contractual agreements with a third party that would constrain its inclusion in this thesis. I am the primary author of this paper.		
Signature		Date	05 Jan 2022

Co-Author Contributions

By signing the Statement of Authorship, each author certifies that:

i. the candidate's stated contribution to the publication is accurate (as detailed above);

ii. permission is granted for the candidate in include the publication in the thesis; and

iii. the sum of all co-author contributions is equal to 100% less the candidate's stated contribution.

Name of Co-Author	Rey Cheng Chin		
Contribution to the Paper	I acted as primary supervisor for the candidate, aided in developing of the simulations, revising the manuscript and evaluating the final version of the manuscript.		
Signature		Date	06/01/2022

Name of Co-Author			
Contribution to the Paper			
Signature		Date	

4.5 Paper 5

Introduction

This study explores the modulation effects of MVGs in terms of spanwise modulation of the Reynolds shear stress distributions, which characterise the induced momentum transport due to the MVGs. Quadrant analysis of Reynolds shear stress and spanwise Fourier mode decomposition are proposed to study the large-scale and small-scale sweep and ejection events using well-resolved large-eddy simulation data.

Decomposition of the Reynolds shear stress in a turbulent boundary layer modified by miniature vortex generators

This paper is submitted to *Physical Review Fluids* and is currently under review.

Statement of Authorship

Title of Paper	Decomposition of the Reynolds shear stress in a turbulent boundary layer modified by miniature vortex generators
Publication Status	☐ Published ☐ Accepted for Publication ☑ Submitted for Publication ☐ Unpublished and Unsubmitted work written in manuscript style
Publication Details	

Principal Author

Name of Principal Author (Candidate)	Chi Ip Chan		
Contribution to the Paper	Under the supervision of R. C, CHIN, I performed the simulations, interpreted and processed the data and wrote the manuscript.		
Overall percentage (%)	70		
Certification:	This paper reports on original research I conducted during the period of my Higher Degree by Research candidature and is not subject to any obligations or contractual agreements with a third party that would constrain its inclusion in this thesis. I am the primary author of this paper.		
Signature		Date	05 Jan 2022

Co-Author Contributions

By signing the Statement of Authorship, each author certifies that:

i. the candidate's stated contribution to the publication is accurate (as detailed above);

ii. permission is granted for the candidate in include the publication in the thesis; and

iii. the sum of all co-author contributions is equal to 100% less the candidate's stated contribution.

Name of Co-Author	Rey Cheng Chin		
Contribution to the Paper	Supervised the development of the research, participated in developing ideas and concepts, helped in interpretation of results, provided critical revision of manuscript.		
Signature		Date	05/01/2022

Name of Co-Author			
Contribution to the Paper			
Signature		Date	

Chapter 5

Summary, conclusions, and outlook

5.1 Summary

The works in this thesis present passive drag reduction controls of turbulent boundary layers, using large-eddy break-up devices and miniatures vortex generators, which can be implemented into engineering systems for different applications. Studies were conducted using well-resolved numerical simulations that reported new findings based on recently developed approaches that aimed to advance fundamental knowledge of passive controls of large-eddy break-up (LEBU) devices and miniatures vortex generators (MVGs), as presented in papers 2 and 4. It has been shown that MVG has promising potential as an efficient low-profile vortex generator in turbulent boundary layers. Furthermore, the ability of large-scale counter-rotating vortices to reduce skin friction drag was demonstrated in Schoppa and Hussain [184], thus the MVG may offer a way to obtain a low-cost skin friction reduction system. On the other hand, it has been shown that LEBU can stabilise the turbulent flow at a specific downstream location, with significant skin friction reduction and lower pressure fluctuations [193]. A particularly promising feature is that they can easily be placed on the surface of aircraft wings, thereby reducing the local induced noise. Overall, both passive control methods have their strengths and weaknesses. Another objective was to develop novel methods to characterise the flow state under the influence of the passive controls implemented and to provide a compact and instructive way of describing the fluid

flow, with a particular emphasis on the quadrant analysis method. Specific conclusions can be found in papers 3 and 5.

5.2 Conclusions

5.2.1 LEBU

Parametric studies based on three well-resolved (near wall well-resolved) large-eddy numerical simulations were carried out for turbulent boundary layer flows over LEBU devices located at three different wall-normal distances from the wall to achieve local skin friction drag reduction and ultimately to achieve net drag reduction. It has been shown that the maximum of the local skin friction drag reduction rate depends on the wall-normal distance where the LEBU device is located. From the parametric studies, the magnitude of maximum skin friction drag reduction rate was found to be

$$\mathrm{DR}_{\max} = 0.087 \times (y/\delta)^{-0.84} \times 100\%, \tag{5.1}$$

where DR = $(c_{f,0} - c_{f,LB})/c_{f,0}$. A detailed analysis on the skin friction variation was performed based on a skin friction decomposition procedure to study different physical mechanisms and identified the main contribution associated with the observed drag reduction, which was due to Reynolds shear stress deficits and disruption of TKE transport. This suggested that the occurrence of turbulence reduction of the flow was due to a wake-wall interaction, as first demonstrated by Savill and Mumford [177]. A remain challenge in applying LEBU in TBL is that the device drag constitutes a major factor when accounting the net drag reduction. Nevertheless, as the device thickness can be further decreased, the device drag in terms of form drag can be considerably reduced.

5.2.2 MVG

We have performed a well-resolved large-eddy simulation for flow over MVG using the IBM, which is sufficiently flexible and possible to work with different configurations of

MVGs to examine the effect of this type of flow control device to different fluid motions of different scales with sufficient accuracy. The simulation clearly shows that the flow over MVG results in high-momentum and low-momentum patterns which cause a large-scale spanwise variation. Over the low-momentum region, fluid flow was forced and transported away from the wall, forming a region of common-flow-up, where a local skin friction reduction of up to 15% was obtained at the low-momentum region. Over the high-momentum region, the opposite situation was observed. The flow was forced to move closer towards the wall, with downward motion formed a region common-flow-down, which confined the turbulent fluctuations in the vicinity of the wall, resulting in the increase of skin friction drag at this area. Because it is possible to systemically change the scale at which the disturbance is introduced to the flow, e.g. by changing the spanwise spacing between MVGs or their geometry. A goal for the future obviously is to extend this base case by setting up parametric study cases attempted to optimise the configurations for net drag reduction purpose or to investigate how the turbulent boundary layer flow responses to the input at different scales. In addition, it would be interesting to see what happens when disturbance is put in at different scales at the same instant of time to the flow by combining MVGs with different sizes (e.g. multi-scale fractal-like structures). A brief summary table with %DR results for all cases studied is presented below.

Summary of passive control results			
Case	Max. %DR	Main DR mechanism	Existing difficulties
LEBU (LB01, LB05 and LB08)	100% $\times$ $0.087(y/\delta)^{-0.84}$	wake-wall interaction	Minimising device drag
MVG	15%	large-scale PVPs	Minimising HSR

5.3 Outlook

In paper 1 we extended the analysis of interscale transport by [104] to consider the turbulent kinetic energy and Reynolds shear stress cascades following Reynolds decomposition (2.33), which is valid in smooth wall zero pressure gradient turbulent boundary layers. As

indicated in (2.34), the Reynolds decomposition can be generalised to fluid flows when the spanwise variation is heterogeneous. Future work can be carried out by extending this approach to include, for example, rough-wall flows, such as those demonstrated by Alves-Portela et al. [7] for two-point scale energy balance [84, 134].

In paper 3 we investigated the performance of miniature vortex generators in zero pressure gradient turbulent boundary layers. The simulation requires Chebyshev-Fourier spectral formulation, using global basis functions. Therefore, the MVGs are introduced using the immerse boundary method with modified boundary conditions, such as those in [20, 31], which might have otherwise led to the Gibbs phenomenon. Future work will focus on this implementation aspect. In our study, the MVG model is restricted to rectangular blades with small thickness. An extension of this work is to take into account the winglet type MVG, which is difficult to implement using the SIMSON code [30]. These restrictions should be relaxed in future work; for example, Nek5000 could be a potential candidate for such a purpose [191].

In paper 5 we presented an analysis to characterise the momentum transport of a turbulent boundary layer modified by miniature vortex generators, in terms of spanwise modulation of the Reynolds shear stress distributions. The quadrant analysis method of triple decomposition of Reynolds shear stress and spanwise Fourier mode decomposition are utilised, and perhaps several potential extensions of this work can be carried out by extending this approach to various other decomposition schemes, such as proper orthogonal decomposition [131, 132] and dynamic mode decomposition [183].

References

[1] Abe, H., Kawamura, H., and Choi, H. (2004). Very large-scale structures and their effects on the wall shear-stress fluctuations in a turbulent channel flow up to $Re_\tau \approx 640$. *J. Fluids Eng.*, 126(5):835–843.

[2] Acarlar, M. S. and Smith, C. R. (1987). A study of hairpin vortices in a laminar boundary layer. part 2. hairpin vortices generated by fluid injection. *J. Fluid Mech.*, 175:43–83.

[3] Adrian, R. J. (2007). Hairpin vortex organization in wall turbulence. *Phys. Fluids*, 19(4):041301.

[4] Adrian, R. J., Meinhart, C. D., and Tomkins, C. D. (2000). Vortex organization in the outer region of the turbulent boundary layer. *J. Fluid Mech.*, 422:1–54.

[5] Alfredsson, P. H. and Örlü, R. (2018). Large-eddy breakup devices–a 40 years perspective from a stockholm horizon. *Flow Turbul. Combust.*, 100(4):877–888.

[6] Allan, B., Yao, C.-S., and Lin, J. (2002). Numerical simulations of vortex generator vanes and jets on a flat plate. *AIAA Paper*. No. 2002-3160.

[7] Alves-Portela, F., Papadakis, G., and Vassilicos, J. C. (2020). The role of coherent structures and inhomogeneity in near-field interscale turbulent energy transfers. *J. Fluid Mech.*, 896:A16.

[8] Anders, J. B. (1990). Boundary layer manipulators at high Reynolds numbers. In Gyr, A., editor, *Structure of Turbulence and Drag Reduction*, pages 475–482, Berlin, Heidelberg. Springer Berlin Heidelberg.

[9] Anders, J. B., Hefner, J. N., and Bushnell, D. M. (1984). Performance of large-eddy breakup devices at post-transitional Reynolds numbers. *AIAA J.* No. 1984-0345.

[10] Ashill, P., Fulker, J., and Hackett, K. (2001). Research at dera on sub boundary layer vortex generators (SBVGs). *AIAA Paper*. No. 2001-0887.

[11] Ashill, P., Fulker, J., and Hackett, K. (2002). Studies of flows induced by sub boundary layer vortex generators (SBVGs). *AIAA Paper*. No. 2002-0968.

[12] Balakumar, B. and Adrian, R. (2007). Large- and very-large-scale motions in channel and boundary-layer flows. *Phil. Trans. R. Soc. Lond. A*, 365(1852):665–681.

[13] Balaras, E. (2004). Modeling complex boundaries using an external force field on fixed Cartesian grids in large-eddy simulations. *Computers & Fluids*, 33(3):375–404.

[14] Bandyopadhyay, P. R. (1986). Review—mean flow in turbulent boundary layers disturbed to alter skin friction. *J. Fluids Eng.*, 108(2):127–140.

[15] Bandyopadhyay, P. R. and Hussain, A. K. M. F. (1984). The coupling between scales in shear flows. *Phys. Fluids*, 27(9):2221–2228.

[16] Bendat, J. S. and Piersol, A. G. (2011). *Random data: analysis and measurement procedures*, volume 729. John Wiley & Sons.

[17] Bertolotti, F. P., Herbert, T., and Spalart, P. R. (1992). Linear and nonlinear stability of the blasius boundary layer. *J. Fluid Mech.*, 242:441–474.

[18] Bolotnov, I. A., Lahey, R. T., Drew, D. A., Jansen, K. E., and Oberai, A. A. (2010). Spectral analysis of turbulence based on the dns of a channel flow. *Comput. Fluids*, 39(4):640–655.

[19] Brown, G. L. and Thomas, A. S. W. (1977). Large structure in a turbulent boundary layer. *Phys. Fluids*, 20(10):S243–S252.

[20] Brynjell-Rahkola, M., Schlatter, P., Hanifi, A., and Henningson, D. S. (2015). Global stability analysis of a roughness wake in a Falkner–Skan–Cooke boundary layer. *Procedia IUTAM*, 14:192–200.

[21] Camarri, S., Fransson, J. H. M., and Talamelli, A. (2014). Numerical investigation of the afrodite transition control strategy. In *Progress in Turbulence V*, pages 65–69. Springer.

[22] Canton, J., Örlü, R., Chin, C., Hutchins, N., Monty, J., and Schlatter, P. (2016a). On large-scale friction control in turbulent wall flow in low Reynolds number channels. *Flow Turbul. Combust.*, 97(3):811–827.

[23] Canton, J., Örlü, R., Chin, C., and Schlatter, P. (2016b). Reynolds number dependence of large-scale friction control in turbulent channel flow. *Phys. Rev. Fluids*, 1:081501.

[24] Cantwell, B. J. (1981). Organized motion in turbulent flow. *Annu. Rev. Fluid Mech.*, 13(1):457–515.

[25] Carpenter, P. W. and Morris, P. J. (1990). The effect of anisotropic wall compliance on boundary-layer stability and transition. *J. Fluid Mech.*, 218:171–223.

[26] Chan, C. I. and Chin, R. C. (2022). Investigation of the influence of miniature vortex generators on the large-scale motions of a turbulent boundary layer. *J. Fluid Mech.*, 932:A29.

[27] Chan, C. I., Schlatter, P., and Chin, R. C. (2021a). Interscale transport mechanisms in turbulent boundary layers. *J. Fluid Mech.*, 921:A13.

[28] Chan, C. I., Örlü, R., Schlatter, P., and Chin, R. C. (2021b). The skin-friction coefficient of a turbulent boundary layer modified by a large-eddy break-up device. *Phys. Fluids*, 33(3):035153.

[29] Chan, L., MacDonald, M., Chung, D., Hutchins, N., and Ooi, A. (2018). Secondary motion in turbulent pipe flow with three-dimensional roughness. *J. Fluid Mech.*, 854:5–33.

[30] Chevalier, M., Lundbladh, A., and Henningson, D. S. (2007). SIMSON–a pseudo-spectral solver for incompressible boundary layer flow. Tech. Rep. TRITA-MEK 2007:07, KTH Mechanics, Stockholm, Sweden.

[31] Chin, C., Örlü, R., Monty, J., Hutchins, N., Ooi, A., and Schlatter, P. (2017a). Simulation of a large-eddy-break-up device (LEBU) in a moderate Reynolds number turbulent boundary layer. *Flow Turbul. Combust.*, 98(2):445–460.

[32] Chin, C., Örlü, R., Schlatter, P., Monty, J., and Hutchins, N. (2017b). Influence of a large-eddy-breakup-device on the turbulent interface of boundary layers. *Flow Turbul. Combust.*, 99(3):823–835.

[33] Cho, M., Hwang, Y., and Choi, H. (2018). Scale interactions and spectral energy transfer in turbulent channel flow. *J. Fluid Mech.*, 854:474–504.

[34] Choi, H., Moin, P., and Kim, J. (1993). Direct numerical simulation of turbulent flow over riblets. *J. Fluid Mech.*, 255:503–539.

[35] Choi, H., Moin, P., and Kim, J. (1994). Active turbulence control for drag reduction in wall bounded flows. *J. Fluid Mech.*, 262:75–110.

[36] Choi, J.-I., Oberoi, R. C., Edwards, J. R., and Rosati, J. A. (2007). An immersed boundary method for complex incompressible flows. *J. Comput. Phys.*, 224(2):757–784.

[37] Christensen, K. T. and Adrian, R. J. (2001). Statistical evidence of hairpin vortex packets in wall turbulence. *J. Fluid Mech.*, 431:433–443.

[38] Chung, S. Y., L., J., and A., B. (2002). Flowfield measurement of device-induced embedded streamwise vortex on a flat plate. *AIAA Paper*. No. 2002-3162.

[39] Cimarelli, A., De Angelis, E., and Casciola, C. (2013). Paths of energy in turbulent channel flows. *J. Fluid Mech.*, 715:436–451.

[40] Cimarelli, A., De Angelis, E., Jiménez, J., and Casciola, C. M. (2016). Cascades and wall-normal fluxes in turbulent channel flows. *J. Fluid Mech.*, 796:417–436.

[41] Coceal, O. and Belcher, S. E. (2004). A canopy model of mean winds through urban areas. *Q. J. R. Meteorol. Soc.*, 130(599):1349–1372.

[42] Coceal, O., Thomas, T. G., Castro, I. P., and Belcher, S. E. (2006). Mean flow and turbulence statistics over groups of urban-like cubical obstacles. *Boundary-Layer Met.*, 121(3):491–519.

[43] Corino, E. R. and Brodkey, R. S. (1969). A visual investigation of the wall region in turbulent flow. *J. Fluid Mech.*, 37(1):1–30.

[44] Corke, T. C., Guezennic, Y., and Nagib, H. M. (1979). Modification in drag of turbulent boundary layers resulting from manipulation of large-scale structures. *Prog. Astronaut Aeromut*, 72:128–143.

[45] Corke, T. C., Nagib, H. M., and Guezennec, Y. (1982). A new view on origin, role and manipulation of large scales in turbulent boundary layers. *NASA CR*, (165861).

[46] Corke, T. C. and Thomas, F. O. (2018). Active and passive turbulent boundary-layer drag reduction. *AIAA Journal*, 56(10):3835–3847.

[47] Danaila, L., Anselmet, F., Zhou, T., and Antonia, R. A. (2001). Turbulent energy scale budget equations in a fully developed channel flow. *J. Fluid Mech.*, 430:87–109.

[48] De Giovanetti, M., Hwang, Y., and Choi, H. (2016). Skin-friction generation by attached eddies in turbulent channel flow. *J. Fluid Mech.*, 808:511–538.

[49] Deck, S., Renard, N., Laraufie, R., and Weiss, P.-É. (2014). Large-scale contribution to mean wall shear stress in high-Reynolds-number flat-plate boundary layers up to Re_θ= 13650. *J. Fluid Mech.*, 743:202–248.

[50] Del Álamo, J. C. and Jiménez, J. (2003). Spectra of the very large anisotropic scales in turbulent channels. *Phys. Fluids*, 15(6):L41–L44.

[51] Den Toonder, J. M. J. and Nieuwstadt, F. T. M. (1997). Reynolds number effects in a turbulent pipe flow for low to moderate re. *Phys. Fluids*, 9(11):3398–3409.

[52] Dimitropoulos, C. D., Dubief, Y., Shaqfeh, E. S. G., and Moin, P. (2006). Direct numerical simulation of polymer-induced drag reduction in turbulent boundary layer flow of inhomogeneous polymer solutions. *J. Fluid Mech.*, 566:153–162.

[53] Domaradzki, J. A., Liu, W., Härtel, C., and Kleiser, L. (1994). Energy transfer in numerically simulated wall-bounded turbulent flows. *Phys. Fluids*, 6(4):1583–1599.

[54] Dong, S., Huang, Y., Yuan, X., and Lozano-Durán, A. (2020). The coherent structure of the kinetic energy transfer in shear turbulence. *J. Fluid Mech.*, 892:A22.

[55] Duan, Y., Zhong, Q., Wang, G., Zhang, P., and Li, D. (2021). Contributions of different scales of turbulent motions to the mean wall-shear stress in open channel flows at low-to-moderate Reynolds numbers. *J. Fluid Mech.*, 918:A40.

[56] Eitel-Amor, G., Örlü, R., and Schlatter, P. (2014). Simulation and validation of a spatially evolving turbulent boundary layer up to Re_θ = 8300. *Intl J. Heat Fluid Flow*, 47:57 – 69.

[57] Endo, T. and Himeno, R. (2002). Direct numerical simulation of turbulent flow over a compliant surface. *J. Turbul.*, 3:7.

[58] Endo, T., Kasagi, N., and Suzuki, Y. (2000). Feedback control of wall turbulence with wall deformation. *Intl J. Heat Fluid Flow*, 21(5):568 – 575. Turbulence and Shear Flow Phenomena 1.

[59] Fadlun, E., Verzicco, R., Orlandi, P., and Mohd-Yusof, J. (2000). Combined immersed-boundary finite-difference methods for three-dimensional complex flow simulations. *J. Comput. Phys.*, 161(1):35–60.

[60] Falco, R. E., Walker, J. D. A., and Smith, F. T. (1991). A coherent structure model of the turbulent boundary layer and its ability to predict Reynolds number dependence. *Phil. Trans. R. Soc. Lond. A*, 336(1641):103–129.

[61] Fiscaletti, D., de Kat, R., and Ganapathisubramani, B. (2018). Spatial–spectral characteristics of momentum transport in a turbulent boundary layer. *J. Fluid Mech.*, 836:599–634.

[62] Forooghi, P., Stroh, A., Schlatter, P., and Frohnapfel, B. (2018). Direct numerical simulation of flow over dissimilar, randomly distributed roughness elements: A systematic study on the effect of surface morphology on turbulence. *Phys. Rev. Fluids*, 3:044605.

[63] Fransson, J. H. M., Brandt, L., Talamelli, A., and Cossu, C. (2004). Experimental and theoretical investigation of the nonmodal growth of steady streaks in a flat plate boundary layer. *Phys. Fluids*, 16(10):3627–3638.

[64] Fransson, J. H. M., Brandt, L., Talamelli, A., and Cossu, C. (2005). Experimental study of the stabilization of Tollmien–Schlichting waves by finite amplitude streaks. *Phys. Fluids*, 17(5):054110.

[65] Fransson, J. H. M. and Talamelli, A. (2012). On the generation of steady streamwise streaks in flat-plate boundary layers. *J. Fluid Mech.*, 698:211–234.

[66] Fukagata, K., Iwamoto, K., and Kasagi, N. (2002). Contribution of Reynolds stress distribution to the skin friction in wall-bounded flows. *Phys. Fluids*, 14(11):L73–L76.

[67] Fukagata, K. and Kasagi, N. (2003). Drag reduction in turbulent pipe flow with feedback control applied partially to wall. *Intl J. Heat Fluid Flow*, 24(4):480–490.

[68] Fukagata, K. and Kasagi, N. (2004). Suboptimal control for drag reduction via suppression of near-wall Reynolds shear stress. *Intl J. Heat Fluid Flow*, 25(3):341 – 350.

[69] Fukagata, K., Kern, S., Chatelain, P., Koumoutsakos, P., and Kasagi, N. (2008). Evolutionary optimization of an anisotropic compliant surface for turbulent friction drag reduction. *J. Turbul.*, 9:N35.

[70] Gad-el Hak, M. (2000). *Flow Control: Passive, Active, and Reactive Flow Management*. Cambridge University Press.

[71] Ganapathisubramani, B., Hutchins, N., Monty, J. P., Chung, D., and Marusic, I. (2012). Amplitude and frequency modulation in wall turbulence. *J. Fluid Mech.*, 712:61–91.

[72] Ganapathisubramani, B., Longmire, E. K., and Marusic, I. (2003). Characteristics of vortex packets in turbulent boundary layers. *J. Fluid Mech.*, 478:35–46.

[73] Gao, T., Tseng, Y.-H., and Lu, X.-Y. (2007). An improved hybrid Cartesian/immersed boundary method for fluid–solid flows. *Int. J. Numer. Methods Fluids*, 55(12):1189–1211.

[74] Gilmanov, A., Sotiropoulos, F., and Balaras, E. (2003). A general reconstruction algorithm for simulating flows with complex 3D immersed boundaries on Cartesian grids. *J. Comput. Phys.*, 191(2):660–669.

[75] Goldstein, D., Handler, R., and Sirovich, L. (1993). Modeling a no-slip flow boundary with an external force field. *J. Comput. Phys.*, 105(2):354–366.

[76] Gorton, S., Jenkins, L., and Anders, S. (2002). Flow control device evaluation for an internal flow with an adverse pressure gradient. *AIAA Paper*. No. 2002-0266.

[77] Grant, H. L. (1958). The large eddies of turbulent motion. *J. Fluid Mech.*, 4(2):149–190.

[78] Guala, M., Hommema, S. E., and Adrian, R. J. (2006). Large-scale and very-large-scale motions in turbulent pipe flow. *J. Fluid Mech.*, 554:521–542.

[79] Haidari, A. H. and Smith, C. R. (1994). The generation and regeneration of single hairpin vortices. *J. Fluid Mech.*, 277:135–162.

[80] Hamilton, J. M., Kim, J., and Waleffe, F. (1995). Regeneration mechanisms of near-wall turbulence structures. *J. Fluid Mech.*, 287:317–348.

[81] Head, M. R. and Bandyopadhyay, P. (1981). New aspects of turbulent boundary-layer structure. *J. Fluid Mech.*, 107:297–338.

[82] Hefner, J. N., Weinstein, I. M., and Bushnell, D. M. (1979). Large-eddy breakup scheme for turbulent viscous drag reduction. *Prog. Astronaut Aeroaut*, 72:110–127.

[83] Hill, R. J. (2001). Equations relating structure functions of all orders. *J. Fluid Mech.*, 434:379–388.

[84] Hill, R. J. (2002). Exact second-order structure-function relationships. *J. Fluid Mech.*, 468:317–326.

[85] Hou, G., Wang, J., and Layton, A. (2012). Numerical methods for Fluid-Structure Interaction — A Review. *Commun. Comput. Phys.*, 12(2):337–377.

[86] Hou, Y. X., Somandepalli, V. S. R., and Mungal, M. G. (2006). A technique to determine total shear stress and polymer stress profiles in drag reduced boundary layer flows. *Exp. Fluids*, 40(4):589–600.

[87] Hou, Y. X., Somandepalli, V. S. R., and Mungal, M. G. (2008). Streamwise development of turbulent boundary-layer drag reduction with polymer injection. *J. Fluid Mech.*, 597:31–66.

[88] Hoyas, S. and Jiménez, J. (2006). Scaling of the velocity fluctuations in turbulent channels up to $Re_\tau \approx 2003$. *Phys. Fluids*, 18(1):011702.

[89] Huang, W.-X. and Tian, F.-B. (2019). Recent trends and progress in the immersed boundary method. *Proc. Inst. Mech. Engng C*, 233(23-24):7617–7636.

[90] Hunt, J. C. R. and Morrison, J. F. (2000). Eddy structure in turbulent boundary layers. *Eur. J. Mech. B Fluids*, 19(5):673 – 694.

[91] Hutchins, N. and Marusic, I. (2007a). Evidence of very long meandering features in the logarithmic region of turbulent boundary layers. *J. Fluid Mech.*, 579:1–28.

[92] Hutchins, N. and Marusic, I. (2007b). Large-scale influences in near-wall turbulence. *Phil. Trans. R. Soc. Lond. A*, 365(1852):647–664.

[93] Iaccarino, G. and Verzicco, R. (2003). Immersed boundary technique for turbulent flow simulations . *Appl. Mech. Rev.*, 56(3):331–347.

[94] Jelly, T. O., Jung, S. Y., and Zaki, T. A. (2014). Turbulence and skin friction modification in channel flow with streamwise-aligned superhydrophobic surface texture. *Phys. Fluids*, 26(9):095102.

[95] Jeong, J., Hussain, F., Schoppa, W., and Kim, J. (1997). Coherent structures near the wall in a turbulent channel flow. *J. Fluid Mech.*, 332:185–214.

[96] Jiménez, J. (2004). Turbulent flows over rough walls. *Annu. Rev. Fluid Mech.*, 36(1):173–196.

[97] Jiménez, J. and Pinelli, A. (1999). The autonomous cycle of near-wall turbulence. *J. Fluid Mech.*, 389:335–359.

[98] Jodai, Y. and Elsinga, G. E. (2016). Experimental observation of hairpin autogeneration events in a turbulent boundary layer. *J. Fluid Mech.*, 795:611–633.

[99] Jung, W. J., Mangiavacchi, N., and Akhavan, R. (1992). Suppression of turbulence in wall-bounded flows by high-frequency spanwise oscillations. *Phys. Fluids*, 4(8):1605–1607.

[100] Kametani, Y. and Fukagata, K. (2011). Direct numerical simulation of spatially developing turbulent boundary layers with uniform blowing or suction. *J. Fluid Mech.*, 681:154–172.

[101] Kang, S., Iaccarino, G., Ham, F., and Moin, P. (2009). Prediction of wall-pressure fluctuation in turbulent flows with an immersed boundary method. *J. Comput. Phys.*, 228(18):6753–6772.

[102] Kasagi, N., Suzuki, Y., and Fukagata, K. (2009). Microelectromechanical systems–based feedback control of turbulence for skin friction reduction. *Annu. Rev. Fluid Mech.*, 41:231–251.

[103] Kawata, T. and Alfredsson, P. (2019). Scale interactions in turbulent rotating planar couette flow: insight through the Reynolds stress transport. *J. Fluid Mech.*, 879:255–295.

[104] Kawata, T. and Alfredsson, P. H. (2018). Inverse interscale transport of the Reynolds shear stress in plane Couette turbulence. *Phys. Rev. Lett.*, 120:244501.

[105] Khadra, K., Angot, P., Parneix, S., and Caltagirone, J.-P. (2000). Fictitious domain approach for numerical modelling of navier–stokes equations. *Int. J. Numer. Methods Fluids*, 34(8):651–684.

[106] Kim, H. T., Kline, S. J., and Reynolds, W. C. (1971). The production of turbulence near a smooth wall in a turbulent boundary layer. *J. Fluid Mech.*, 50(1):133–160.

[107] Kim, J. (2003). Control of turbulent boundary layers. *Phys. Fluids*, 15(5):1093–1105.

[108] Kim, J., Kim, K., and Sung, H. J. (2003). Wall pressure fluctuations in a turbulent boundary layer after blowing or suction. *AIAA J.*, 41(9):1697–1704.

[109] Kim, J., Moin, P., and Moser, R. (1987). Turbulence statistics in fully developed channel flow at low Reynolds number. *J. Fluid Mech.*, 177:133–166.

[110] Kim, J.-S., Hwang, J., Yoon, M., Ahn, J., and Sung, H. J. (2017). Influence of a large-eddy breakup device on the frictional drag in a turbulent boundary layer. *Phys. Fluids*, 29(6):065103.

[111] Kim, K., Sung, H. J., and Chung, M. K. (2002). Assessment of local blowing and suction in a turbulent boundary layer. *AIAA J.*, 40(1):175–177.

[112] Kim, K. C. and Adrian, R. J. (1999). Very large-scale motion in the outer layer. *Phys. Fluids*, 11(2):417–422.

[113] Kim, W. and Choi, H. (2019). Immersed boundary methods for fluid-structure interaction: A review. *Intl J. Heat Fluid Flow*, 75:301–309.

[114] Kline, S. J., Reynolds, W. C., Schraub, F. A., and Runstadler, P. W. (1967). The structure of turbulent boundary layers. *J. Fluid Mech.*, 30:741–773.

[115] Kovasznay, L. S. G., Kibens, V., and Blackwelder, R. F. (1970). Large-scale motion in the intermittent region of a turbulent boundary layer. *J. Fluid Mech.*, 41(2):283–325.

[116] Lee, C., Kim, J., Babcock, D., and Goodman, R. (1997). Application of neural networks to turbulence control for drag reduction. *Phys. Fluids*, 9(6):1740–1747.

[117] Lee, C., Kim, J., and Choi, H. (1998). Suboptimal control of turbulent channel flow for drag reduction. *J. Fluid Mech.*, 358:245–258.

[118] Lee, J., Kim, J., Choi, H., and Yang, K.-S. (2011). Sources of spurious force oscillations from an immersed boundary method for moving-body problems. *J. Comput. Phys.*, 230(7):2677–2695.

[119] Lee, M. and Moser, R. D. (2019). Spectral analysis of the budget equation in turbulent channel flows at high Reynolds number. *J. Fluid Mech.*, 860:886–938.

[120] Li, C. W. and Wang, L. L. (2004). An immersed boundary finite difference method for les of flow around bluff shapes. *Int. J. Numer. Methods Fluids*, 46(1):85–107.

[121] Li, Q., Schlatter, P., and Henningson, D. S. (2008). Spectral simulations of wall-bounded flows on massively parallel computers. Tech. Rep., KTH Mechanics, Stockholm, Sweden.

[122] Lin, J. (1999). Control of turbulent boundary-layer separation using micro-vortex generators. *AIAA Paper*. No. 1999-3404.

[123] Lin, J. (2002). Review of research on low-profile vortex generators to control boundary-layer separation. *Prog. Aerospace Sci.*, 38(4):389–420.

[124] Lina, L. J. and Reed III, W. H. (1950). A preliminary flight investigation of the effects of vortex generators on separation due to shock. Tech. Rep.

[125] Lögdberg, O., Fransson, J. H. M., and Alfredsson, P. H. (2009). Streamwise evolution of longitudinal vortices in a turbulent boundary layer. *J. Fluid Mech.*, 623:27–58.

[126] Lozano-Durán, A., Flores, O., and Jiménez, J. (2012). The three-dimensional structure of momentum transfer in turbulent channels. *J. Fluid Mech.*, 694:100–130.

[127] Lozano-Durán, A. and Jiménez, J. (2014). Time-resolved evolution of coherent structures in turbulent channels: characterization of eddies and cascades. *J. Fluid Mech.*, 759:432–471.

[128] Lu, S. S. and Willmarth, W. W. (1973). Measurements of the structure of the Reynolds stress in a turbulent boundary layer. *J. Fluid Mech.*, 60(3):481–511.

[129] Lumley, J. and Blossey, P. (1998). Control of turbulence. *Annu. Rev. Fluid Mech.*, 30(1):311–327.

[130] Lumley, J. L. (1964). Spectral energy budget in wall turbulence. *Phys. Fluids*, 7(2):190–196.

[131] Lumley, J. L. (1967). The structure of inhomogeneous turbulent flows. *Atmospheric Turbulence and Radio Wave Propagation*, pages 166–178. Nauka.

[132] Lumley, J. L. (1970). *Stochastic tools in turbulence*. Academic Press. New York.

[133] Lynn, T. B., Bechert, D. W., and Gerich, D. A. (1995). Direct drag measurements in a turbulent flat-plate boundary layer with turbulence manipulators. *Exp. Fluids*, 19(6):405–416.

[134] Marati, N., Casciola, C. M., and Piva, R. (2004). Energy cascade and spatial fluxes in wall turbulence. *J. Fluid Mech.*, 521:191–215.

[135] Martell, M. B., Perot, J. B., and Rothstein, J. P. (2009). Direct numerical simulations of turbulent flows over superhydrophobic surfaces. *J. Fluid Mech.*, 620:31–41.

[136] Marusic, I. (2001). On the role of large-scale structures in wall turbulence. *Phys. Fluids*, 13(3):735–743.

[137] Marusic, I. and Monty, J. P. (2019). Attached eddy model of wall turbulence. *Annu. Rev. Fluid Mech.*, 51(1):49–74.

[138] Marusic, I., Monty, J. P., Hultmark, M., and Smits, A. J. (2013). On the logarithmic region in wall turbulence. *J. Fluid Mech.*, 716:R3.

[139] Mathis, R., Hutchins, N., and Marusic, I. (2009). Large-scale amplitude modulation of the small-scale structures in turbulent boundary layers. *J. Fluid Mech.*, 628:311–337.

[140] Millikan, C. B. (1939). A critical discussion of turbulent flow in channels and circular tubes. *Proc. 5th Int. Congress on Applied Mechanics (Cambridge, MA, 1938)*, pages 386–392.

[141] Min, T., Yul Yoo, J., Choi, H., and Joseph, D. D. (2003). Drag reduction by polymer additives in a turbulent channel flow. *J. Fluid Mech.*, 486:213–238.

[142] Mittal, R. and Iaccarino, G. (2005). Immersed boundary methods. *Annu. Rev. Fluid Mech.*, 37(1):239–261.

[143] Mizuno, Y. (2016). Spectra of energy transport in turbulent channel flows for moderate Reynolds numbers. *J. Fluid Mech.*, 805:171–187.

[144] Mohd-Yusof, J. (1997). Combined immersed-boundary/b-spline methods for simulations of flow in complex geometries. *Annu. Res. Briefs. Center for Turbulence Research*, 161(1):317–327.

[145] Moin, P. and Mahesh, K. (1998). Direct numerical simulation: A tool in turbulence research. *Annu. Rev. Fluid Mech.*, 30(1):539–578.

[146] Monty, J. P., Hutchins, N., NG, H. C. H., Marusic, I., and Chong, M. S. (2009). A comparison of turbulent pipe, channel and boundary layer flows. *J. Fluid Mech.*, 632:431–442.

[147] Moser, R. D., Kim, J., and Mansour, N. N. (1999). Direct numerical simulation of turbulent channel flow up to $Re_\tau = 590$. *Phys. Fluids*, 11(4):943–945.

[148] Motoori, Y. and Goto, S. (2019). Generation mechanism of a hierarchy of vortices in a turbulent boundary layer. *J. Fluid Mech.*, 865:1085–1109.

[149] Muldoon, F. and Acharya, S. (2008). A divergence-free interpolation scheme for the immersed boundary method. *Int. J. Numer. Methods Fluids*, 56(10):1845–1884.

[150] Murlis, J., Tsai, H. M., and Bradshaw, P. (1982). The structure of turbulent boundary layers at low Reynolds numbers. *J. Fluid Mech.*, 122:13–56.

[151] Nagano, Y. and Tagawa, M. (1988). Statistical characteristics of wall turbulence with a passive scalar. *J. Fluid Mech.*, 196:157–185.

[152] Nakanishi, R., Mamori, H., and Fukagata, K. (2012). Relaminarization of turbulent channel flow using traveling wave-like wall deformation. *Intl J. Heat Fluid Flow*, 35:152 – 159. 7th Symposium on Turbulence & Shear Flow Phenomena (TSFP7).

[153] Nepf, H. M. (2012). Flow and transport in regions with aquatic vegetation. *Annu. Rev. Fluid Mech.*, 44(1):123–142.

[154] Ong, L. and Wallace, J. M. (1998). Joint probability density analysis of the structure and dynamics of the vorticity field of a turbulent boundary layer. *J. Fluid Mech.*, 367:291–328.

[155] Panton, R. L. (2001). Overview of the self-sustaining mechanisms of wall turbulence. *Prog. Aerosp. Sci.*, 37(4):341 – 383.

[156] Park, J. and Choi, H. (1999). Effects of uniform blowing or suction from a spanwise slot on a turbulent boundary layer flow. *Phys. Fluids*, 11(10):3095–3105.

[157] Peaudecerf, F. J., Landel, J. R., Goldstein, R. E., and Luzzatto-Fegiz, P. (2017). Traces of surfactants can severely limit the drag reduction of superhydrophobic surfaces. *Proc. Natl Acad. Sci. USA*, 114(28):7254–7259.

[158] Perry, A. E. and Chong, M. S. (1982). On the mechanism of wall turbulence. *J. Fluid Mech.*, 119:173–217.

[159] Perry, A. E., Henbest, S., and Chong, M. S. (1986). A theoretical and experimental study of wall turbulence. *J. Fluid Mech.*, 165:163–199.

[160] Perry, A. E. and Marušić, I. (1995). A wall-wake model for the turbulence structure of boundary layers. part 1. extension of the attached eddy hypothesis. *J. Fluid Mech.*, 298:361–388.

[161] Peskin, C. S. (1972). Flow patterns around heart valves: A numerical method. *J. Comput. Phys.*, 10(2):252–271.

[162] Peskin, C. S. (2002). The immersed boundary method. *Acta Numer.*, 11:479–517.

[163] Philip, J. R. (1972). Flows satisfying mixed no-slip and no-shear conditions. *Zeitschrift für angewandte Mathematik und Physik ZAMP*, 23(3):353–372.

[164] Pirozzoli, S., Bernardini, M., and Orlandi, P. (2011). Large-scale motions and inner/outer layer interactions in turbulent Couette–Poiseuille flows. *J. Fluid Mech.*, 680:534–563.

[165] Pope, S. B. (2000). *Turbulent Flows*. Cambridge University Press.

[166] Quadrio, M. and Ricco, P. (2004). Critical assessment of turbulent drag reduction through spanwise wall oscillations. *J. Fluid Mech.*, 521:251–271.

[167] Renard, N. and Deck, S. (2016). A theoretical decomposition of mean skin friction generation into physical phenomena across the boundary layer. *J. Fluid Mech.*, 790:339–367.

[168] Reynolds, W. C. and Hussain, A. K. M. F. (1972). The mechanics of an organized wave in turbulent shear flow. Part 3. Theoretical models and comparisons with experiments. *J. Fluid Mech.*, 54(2):263–288.

[169] Robinson, S. K. (1991). Coherent motions in the turbulent boundary layer. *Annu. Rev. Fluid Mech.*, 23(1):601–639.

[170] Rotta, J. (1951). Statistische theorie nichthomogener turbulenz. *Zeitschrift für Physik*, 129(6):547–572.

[171] S., T. Y. Y. and K., N. (2008). Drag reduction of turbulence air channel flow with distributed micro sensors and actuators. *J. Fluid Sci. Technol.*, 3(1):137–148.

[172] Sahlin, A., Alfredsson, P. H., and Johansson, A. V. (1986). Direct drag measurements for a flat plate with passive boundary layer manipulators. *Phys. Fluids*, 29(3):696–700.

[173] Sahlin, A., Johansson, A. V., and Alfredsson, P. H. (1988). The possibility of drag reduction by outer layer manipulators in turbulent boundary layers. *Phys. Fluids*, 31(10):2814–2820.

[174] Saiki, E. and Biringen, S. (1996). Numerical simulation of a cylinder in uniform flow: Application of a virtual boundary method. *J. Comput. Phys.*, 123(2):450–465.

[175] Sattarzadeh, S. S. and Fransson, J. H. M. (2015). On the scaling of streamwise streaks and their efficiency to attenuate Tollmien–Schlichting waves. *Exp. Fluids*, 56(3):1–16.

[176] Sattarzadeh, S. S., Fransson, J. H. M., Talamelli, A., and Fallenius, B. E. G. (2014). Consecutive turbulence transition delay with reinforced passive control. *Phys. Rev. E*, 89:061001.

[177] Savill, A. M. and Mumford, J. C. (1988). Manipulation of turbulent boundary layers by outer-layer devices: skin-friction and flow-visualization results. *J. Fluid Mech.*, 191:389–418.

[178] Schlatter, P., Li, Q., Brethouwer, G., Johansson, A. V., and Henningson, D. S. (2010). Simulations of spatially evolving turbulent boundary layers up to $Re_\theta = 4300$. *Intl J. Heat Fluid Flow*, 31(3):251 – 261.

[179] Schlatter, P., Li, Q., Örlü, R., Hussain, F., and Henningson, D. (2014). On the near-wall vortical structures at moderate Reynolds numbers. *Eur. J. Mech. B Fluids*, 48:75 – 93.

[180] Schlatter, P. and Örlü, R. (2012). Turbulent boundary layers at moderate Reynolds numbers: inflow length and tripping effects. *J. Fluid Mech.*, 710:5–34.

[181] Schlatter, P., Stolz, S., and Kleiser, L. (2004). LES of transitional flows using the approximate deconvolution model. *Intl J. Heat Fluid Flow*, 25(3):549 – 558.

[182] Schlichting, H. and Gersten, K. (2003). *Boundary Layer Theory*. Springer.

[183] Schmid, P. J. (2010). Dynamic mode decomposition of numerical and experimental data. *J. Fluid Mech.*, 656:5–28.

[184] Schoppa, W. and Hussain, F. (1998). A large-scale control strategy for drag reduction in turbulent boundary layers. *Phys. Fluids*, 10(5):1049–1051.

[185] Schoppa, W. and Hussain, F. (2002). Coherent structure generation in near-wall turbulence. *J. Fluid Mech.*, 453:57–108.

[186] Schäfer, K., Stroh, A., Forooghi, P., and Frohnapfel, B. (2022). Modelling spanwise heterogeneous roughness through a parametric forcing approach. *J. Fluid Mech.*, 930:A7.

[187] Shahinfar, S., Fransson, J. H. M., Sattarzadeh, S. S., and Talamelli, A. (2013). Scaling of streamwise boundary layer streaks and their ability to reduce skin-friction drag. *J. Fluid Mech.*, 733:1–32.

[188] Shahinfar, S., Sattarzadeh, S. S., and Fransson, J. H. M. (2014). Passive boundary layer control of oblique disturbances by finite-amplitude streaks. *J. Fluid Mech.*, 749:1–36.

[189] Shahinfar, S., Sattarzadeh, S. S., Fransson, J. H. M., and Talamelli, A. (2012). Revival of classical vortex generators now for transition delay. *Phys. Rev. Lett.*, 109:074501.

[190] Shinn, A., Goodwin, M., and Vanka, S. (2009). Immersed boundary computations of shear- and buoyancy-driven flows in complex enclosures. *Int. J. Heat Mass Transfer*, 52(17):4082–4089. Special Issue Honoring Professor D. Brian Spalding.

[191] Siconolfi, L., Camarri, S., and Fransson, J. H. M. (2015). Stability analysis of boundary layers controlled by miniature vortex generators. *J. Fluid Mech.*, 784:596–618.

[192] Smits, A. J., McKeon, B. J., and Marusic, I. (2011). High–Reynolds number wall turbulence. *Annu. Rev. Fluid Mech.*, 43(1):353–375.

[193] Spalart, P., Strelets, M., and Travin, A. (2006). Direct numerical simulation of large-eddy-break-up devices in a boundary layer. *Intl J. Heat Fluid Flow*, 27(5):902 – 910. Special issue of the 6th International Symposium on Engineering Turbulence Modelling and Measurements – ETMM6.

[194] Stolz, S., Adams, N. A., and Kleiser, L. (2001). An approximate deconvolution model for large-eddy simulation with application to incompressible wall-bounded flows. *Phys. Fluids*, 13(4):997–1015.

[195] Stroh, A., Frohnapfel, B., Schlatter, P., and Hasegawa, Y. (2015). A comparison of opposition control in turbulent boundary layer and turbulent channel flow. *Phys. Fluids*, 27(7):075101.

[196] Stroh, A., Schäfer, K., Frohnapfel, B., and Forooghi, P. (2020). Rearrangement of secondary flow over spanwise heterogeneous roughness. *J. Fluid Mech.*, 885:R5.

[197] Sumitani, Y. and Kasagi, N. (1995). Direct numerical simulation of turbulent transport with uniform wall injection and suction. *AIAA J.*, 33(7):1220–1228.

[198] Taylor, H. D. (1947). The elimination of diffuser separation by vortex generators. *Research Department Report No. R-4012-3, United Aircraft Corporation, East Hartford, Connecticut*, 103.

[199] Tennekes, H. and Lumley, J. L. (1972). *A First Course in Turbulence*. MIT press.

[200] Theodorsen, T. (1952). Mechanisms of turbulence. *Proceedings of the* 2^{nd} *Midwestern Conference on Fluid Mechanics, 1952*.

[201] Thiesset, F., Danaila, L., and Antonia, R. (2014). Dynamical interactions between the coherent motion and small scales in a cylinder wake. *J. Fluid Mech.*, 749:201–226.

[202] Toh, S. and Itano, T. (2005). Interaction between a large-scale structure and near-wall structures in channel flow. *J. Fluid Mech.*, 524:249–262.

[203] Tomiyama, N. and Fukagata, K. (2013). Direct numerical simulation of drag reduction in a turbulent channel flow using spanwise traveling wave-like wall deformation. *Phys. Fluids*, 25(10):105115.

[204] Tomkins, C. D. and Adrian, R. J. (2003). Spanwise structure and scale growth in turbulent boundary layers. *J. Fluid Mech.*, 490:37–74.

[205] Toms, B. A. (1977). On the early experiments on drag reduction by polymers. *Phys. Fluids*, 20(10):S3–S5.

[206] Townsend, A. A. (1976). *The Structure of Turbulent Shear Flow*. Cambridge University Press.

[207] Tseng, Y.-H. and Ferziger, J. H. (2003). A ghost-cell immersed boundary method for flow in complex geometry. *J. Comput. Phys.*, 192(2):593–623.

[208] Türk, S., Daschiel, G., Stroh, A., Hasegawa, Y., and Frohnapfel, B. (2014). Turbulent flow over superhydrophobic surfaces with streamwise grooves. *J. Fluid Mech.*, 747:186–217.

[209] Virk, P. S., Merrill, E. W., Mickley, H. S., Smith, K. A., and Mollo-Christensen, E. L. (1967). The toms phenomenon: turbulent pipe flow of dilute polymer solutions. *J. Fluid Mech.*, 30(2):305–328.

[210] Von Kármán, T. (1930). Mechanische aenlichkeit und turbulenz. *Nachrichten von der Gesellschaft der Wissenschaften zu Göttingen, Mathematisch-Physikalische Klasse*, 1930:58–76.

[211] Waleffe, F. (1997). On a self-sustaining process in shear flows. *Phys. Fluids*, 9(4):883–900.

[212] Wallace, J. M. (2016). Quadrant analysis in turbulence research: history and evolution. *Annu. Rev. Fluid Mech.*, 48:131–158.

[213] Wallace, J. M., Eckelmann, H., and Brodkey, R. S. (1972). The wall region in turbulent shear flow. *J. Fluid Mech.*, 54:39–48.

[214] White, C. M. and Mungal, M. G. (2008). Mechanics and prediction of turbulent drag reduction with polymer additives. *Annu. Rev. Fluid Mech.*, 40(1):235–256.

[215] Willmarth, W. W. and Lu, S. S. (1972). Structure of the Reynolds stress near the wall. *J. Fluid Mech.*, 55:65–92.

[216] Wu, X. and Moin, P. (2009). Direct numerical simulation of turbulence in a nominally zero-pressure-gradient flat-plate boundary layer. *J. Fluid Mech.*, 630:5–41.

[217] Yajnik, K. S. and Acharya, M. (1978). Non-equilibrium effects in a turbulent boundary layer due to the destruction of large eddies. In Fiedler, H., editor, *Structure and Mechanisms of Turbulence I*, volume 75 of *Lecture Notes in Physics, Berlin Springer Verlag*, pages 249–260.

[218] Yao, C., Lin, J., and Allen, B. (2002). Flowfield measurement of device-induced embedded streamwise vortex on a flat plate. *AIAA Paper*. No. 2002-3162.

[219] Yao, J., Chen, X., Thomas, F., and Hussain, F. (2017). Large-scale control strategy for drag reduction in turbulent channel flows. *Phys. Rev. Fluids*, 2:062601.

[220] Yoon, M., Ahn, J., Hwang, J., and Sung, H. J. (2016). Contribution of velocity-vorticity correlations to the frictional drag in wall-bounded turbulent flows. *Phys. Fluids*, 28(8):081702.

[221] Yu, B., Li, F., and Kawaguchi, Y. (2004). Numerical and experimental investigation of turbulent characteristics in a drag-reducing flow with surfactant additives. *Intl J. Heat Fluid Flow*, 25(6):961 – 974.

[222] Zhang, N. and Zheng, Z. (2007). An improved direct-forcing immersed-boundary method for finite difference applications. *J. Comput. Phys.*, 221(1):250–268.

[223] Zhou, J., Adrian, R. J., Balachandar, S., and Kendall, T. M. (1999). Mechanisms for generating coherent packets of hairpin vortices in channel flow. *J. Fluid Mech.*, 387:353–396.

Appendix A

Fukagata-Iwamoto-Kasagi identity

The FIK identity proposed by Fukagata et al. [66] discusses dynamic effects and their statistical contributions to the skin friction coefficient, mainly utilised for investigation into incompressible turbulent wall-bounded flows. A note for the derivation of the FIK identity in plane channel and plane TBL flows is provided here.

A.1 Two-dimensional turbulent channel flows

Considering the RANS in the streamwise direction for two-dimensional turbulent channel flows

$$-\frac{\partial \bar{p}^\star}{\partial x^\star} = \frac{\partial}{\partial y^\star}\left[\overline{u'v'}^\star - \frac{1}{Re_b}\frac{\partial \bar{u}^\star}{\partial y^\star}\right] + \bar{I}_x^\star + \frac{\partial \bar{u}^\star}{\partial t^\star}, \tag{A.1}$$

where

$$\bar{I}_x^\star = \frac{\partial \bar{u}^\star \bar{u}^\star}{\partial x^\star} + \frac{\partial \bar{u}^\star \bar{v}^\star}{\partial y^\star} - \frac{1}{Re_b}\frac{\partial^2 \bar{u}^\star}{\partial x^{\star 2}}, \tag{A.2}$$

where $\star$ denotes that a quantity is non-dimensionalised with δ and twice the bulk mean velocity $2U_b$. With assumptions that there is a (i) constant flow rate, (ii) homogeneity in the spanwise direction, (iii) symmetry with respect to the centre plane, and (iv) no-slip wall condition ie. $u|_{wall} = w|_{wall} = 0$ and (v) $\bar{v}(x, 0, z, t) = 0$. An integration of (A.1) from the wall to δ gives

$$\int_0^1 -\frac{\partial \bar{p}^\star}{\partial x^\star}\, dy^\star = \int_0^1 \frac{\partial}{\partial y^\star}\left[\overline{u'v'}^\star - \frac{1}{Re_b}\frac{\partial \bar{u}^\star}{\partial y^\star}\right] + \bar{I}_x^\star + \frac{\partial \bar{u}^\star}{\partial t^\star}\, dy^\star, \tag{A.3}$$

$$\int_0^1 -\frac{\partial \bar{p}^\star}{\partial x^\star}\, dy^\star = \int_0^1 \bar{I}_x^\star + \frac{\partial \bar{u}^\star}{\partial t^\star}\, dy^\star + \left[\overline{u'v'}^\star - \frac{1}{Re_b}\frac{\partial \bar{u}^\star}{\partial y^\star} \right]\Bigg|_0^1, \tag{A.4}$$

$$\int_0^1 -\frac{\partial \bar{p}^\star}{\partial x^\star}\, dy^\star = \int_0^1 \bar{I}_x^\star + \frac{\partial \bar{u}^\star}{\partial t^\star}\, dy^\star + \frac{1}{Re_b}\frac{\partial \bar{u}^\star}{\partial y^\star}\Bigg|_0^1, \tag{A.5}$$

$$\int_0^1 -\frac{\partial \bar{p}^\star}{\partial x^\star}\, dy^\star = \int_0^1 \bar{I}_x^\star + \frac{\partial \bar{u}^\star}{\partial t^\star}\, dy^\star + \frac{1}{8} c_f(x), \tag{A.6}$$

where

$$c_f(x) = \frac{\tau_w}{\frac{1}{2}\rho {U_b}^2} = \frac{8}{Re_b} \left. \frac{\partial \frac{\bar{u}}{2U_b}}{\partial \frac{y}{\delta}} \right|_w = \frac{8}{Re_b} \left. \frac{\partial \bar{u}^\star}{\partial y^\star} \right|_w .$$

Substitute (A.6) into (A.1)

$$-\frac{\partial \bar{p}^\star}{\partial x^\star} + \int_0^1 \frac{\partial \bar{p}^\star}{\partial x^\star}\, dy^\star = \frac{\partial}{\partial y^\star}\left[\overline{u'v'}^\star - \frac{1}{Re_b}\frac{\partial \bar{u}^\star}{\partial y^\star} \right] + \bar{I}_x^\star - \int_0^1 \bar{I}_x^\star\, dy^\star - \frac{1}{8} c_f(x) + \frac{\partial \bar{u}^\star}{\partial t^\star}, \tag{A.7}$$

$$\frac{1}{8} c_f(x) = \frac{\partial}{\partial y^\star}\left[\overline{u'v'}^\star - \frac{1}{Re_b}\frac{\partial \bar{u}^\star}{\partial y^\star} \right] + \check{I}_x + \frac{\partial \check{p}}{\partial x} + \frac{\partial \bar{u}^\star}{\partial t^\star}, \tag{A.8}$$

where

$$\check{I}_x = \bar{I}_x^\star - \int_0^1 \bar{I}_x^\star\, dy^\star, \tag{A.9}$$

$$\frac{\partial \check{p}}{\partial x} = \frac{\partial \bar{p}^\star}{\partial x^\star} - \int_0^1 \frac{\partial \bar{p}^\star}{\partial x^\star}\, dy^\star. \tag{A.10}$$

Integrate (A.8) from the wall with respect to y

$$\int_0^{y^\star} \frac{c_f(x)}{8}\, d\gamma = \int_0^{y^\star} \frac{\partial}{\partial \gamma}\left[\overline{u'v'}^\star - \frac{1}{Re_b}\frac{\partial \bar{u}^\star}{\partial \gamma} \right] d\gamma + \int_0^{y^\star} \check{I}_x + \frac{\partial \check{p}}{\partial x} + \frac{\partial \bar{u}^\star}{\partial t^\star}\, d\gamma, \tag{A.11}$$

$$y^\star \frac{c_f(x)}{8} = \overline{u'v'}^\star(x^\star, y^\star) - \frac{1}{Re_b}\frac{\partial \bar{u}^\star}{\partial y^\star}(x^\star, y^\star) + \left. \frac{1}{Re_b}\frac{\partial \bar{u}^\star}{\partial y^\star}(x^\star, y^\star) \right|_w + \int_0^{y^\star} S_D(x^\star, \gamma)\, d\gamma, \tag{A.12}$$

where

$$S_D(x^\star, \gamma) = \check{I}_x + \frac{\partial \check{p}}{\partial x} + \frac{\partial \bar{u}^\star}{\partial t^\star}, \tag{A.13}$$

$$(y^\star - 1)\frac{c_f(x)}{8} = \overline{u'v'}^\star(x^\star, y^\star) - \frac{1}{Re_b}\frac{\partial \bar{u}^\star}{\partial y^\star}(x^\star, y^\star) + \int_0^{y^\star} S_D(x^\star, \gamma)\, d\gamma. \tag{A.14}$$

Integrate (A.12) from the wall with respect to y

$$
\begin{aligned}
&(\frac{y^{\star 2}}{2}-y^{\star})\,\frac{c_f(x)}{8}\\
&=\int_0^{y^\star}\overline{u'v'}^{\star}(x^\star,\phi)d\phi-\frac{1}{Re_b}\bar{u}(x^\star,y^\star)+\frac{1}{Re_b}\bar{u}(x^\star,y^\star)\,|_w+\int_0^{y^\star}\int_0^{\phi}S_D(x^\star,\gamma)\,d\gamma d\phi,\\
&=\int_0^{y^\star}\overline{u'v'}^{\star}(x^\star,\phi)\,d\phi-\frac{1}{Re_b}\bar{u}(x^\star,y^\star)+\int_0^{y^\star}\int_0^{\phi}S_D(x^\star,\gamma)\,d\gamma d\phi. \qquad \text{(A.15)}
\end{aligned}
$$

Integrate (A.15) from the wall to the boundary layer thickness

$$
\begin{aligned}
&\int_0^1(\frac{y^{\star 2}}{2}-y^{\star})\,\frac{c_f(x)}{8}\,dy^\star\\
&=\int_0^1\int_0^{y^\star}\overline{u'v'}^{\star}(x^\star,\phi)\,d\phi dy^\star-\int_0^1\frac{1}{Re_b}\bar{u}(x^\star,y^\star)\,dy^\star+\int_0^1\int_0^{y^\star}\int_0^{\phi}S_D(x^\star,\gamma)\,d\gamma d\phi dy^\star,
\end{aligned}
\qquad \text{(A.16)}
$$

$$
\begin{aligned}
&-\frac{1}{24}c_f(x)\\
&=\underbrace{\int_0^1\int_0^{y^\star}\overline{u'v'}^{\star}(x^\star,\phi)\,d\phi dy^\star}_{a}-\underbrace{\int_0^1\frac{1}{Re_b}\bar{u}(x^\star,y^\star)\,dy^\star}_{b}+\underbrace{\int_0^1\int_0^{y^\star}\int_0^{\phi}S_D(x^\star,\gamma)\,d\gamma d\phi dy^\star}_{c}.
\end{aligned}
\qquad \text{(A.17)}
$$

(A.17a) is

$$
\begin{aligned}
\int_0^1\int_0^{y^\star}\overline{u'v'}^{\star}(x^\star,\phi)\,d\phi dy^\star&=y^\star\int_0^{y^\star}\overline{u'v'}^{\star}(x^\star,\phi)\,d\phi\Big|_0^1-\int_0^1 y^\star\overline{u'v'}^{\star}(x^\star,y^\star)\,dy^\star,\\
&=\int_0^1\overline{u'v'}^{\star}(x^\star,\phi)\,d\phi-\int_0^1 y^\star\overline{u'v'}^{\star}(x^\star,y^\star)\,dy^\star,\\
&=\int_0^1(1-y^\star)\overline{u'v'}^{\star}(x^\star,y^\star)\,dy^\star.
\end{aligned}
$$

(A.17b) is

$$
\int_0^1\frac{1}{Re_b}\bar{u}(x^\star,y^\star)\,dy^\star=\frac{1}{Re_b}\int_0^1\bar{u}(x^\star,y^\star)\,dy^\star=\frac{1}{2Re_b}.
$$

(A.17c) is

$$\begin{aligned}
&\int_0^1 \int_0^{y^\star} \int_0^{\phi} S_D(x^\star,\gamma)\, d\gamma d\phi dy^\star \\
&= y^\star \int_0^{y^\star} \int_0^{\phi} S_D(x^\star,\gamma)\, d\gamma d\phi \Big|_0^1 - \int_0^1 y^\star \int_0^{y^\star} S_D(x^\star,\gamma)\, d\gamma dy^\star, \\
&= \underbrace{\int_0^1 \int_0^{\phi} S_D(x^\star,\gamma)\, d\gamma d\phi}_{c1} - \underbrace{\int_0^1 y^\star \int_0^{y^\star} S_D(x^\star,\gamma)\, d\gamma dy^\star}_{c2}.
\end{aligned} \tag{A.18}$$

(A.18c1) is

$$\begin{aligned}
\int_0^1 \int_0^{\phi} S_D(x^\star,\gamma)\, d\gamma d\phi &= \phi \int_0^{\phi} S_D(x^\star,\gamma)\, d\gamma \Big|_0^1 - \int_0^1 \phi S_D(x^\star,\phi)\, d\phi, \\
&= \int_0^1 S_D(x^\star,y^\star)\, dy^\star - \int_0^1 y^\star S_D(x^\star,y^\star)\, dy^\star.
\end{aligned}$$

(A.18c2) is

$$\begin{aligned}
&\int_0^1 y^\star \int_0^{y^\star} S_D(x^\star,\gamma)\, d\gamma dy^\star \\
&\quad = y^{\star 2} \int_0^{y^\star} S_D(x^\star,\gamma)\, d\gamma \Big|_0^1 - \int_0^1 y^\star \frac{\partial}{\partial y^\star}(y^\star \int_0^{y^\star} S_D(x^\star,\gamma)\, d\gamma)\, dy^\star, \\
&\quad = \int_0^1 S_D(x^\star,y^\star)\, dy^\star - \int_0^1 y^\star \int_0^{y^\star} S_D(x^\star,\gamma)\, d\gamma dy^\star - \int_0^1 y^{\star 2} S_D(x^\star,y^\star)\, dy^\star.
\end{aligned}$$

Rearrange

$$\int_0^1 y^\star \int_0^{y^\star} S_D(x^\star,\gamma)\, d\gamma dy^\star = \frac{1}{2} \int_0^1 (1-y^{\star 2}) S_D(x^\star,y^\star)\, dy^\star.$$

Hence, (A.17c) becomes

$$\begin{aligned}
&\int_0^1 \int_0^{y^\star} \int_0^{\phi} S_D(x^\star, \gamma)\, d\gamma d\phi dy^\star \\
&= \int_0^1 S_D(x^\star, y^\star)\, dy^\star - \int_0^1 y^\star S_D(x^\star, y^\star)\, dy^\star - \frac{1}{2}\int_0^1 (1 - y^{\star 2}) S_D(x^\star, y^\star)\, dy^\star, \\
&= \frac{1}{2}\int_0^1 (1 - y^\star)^2 S_D(x^\star, y^\star)\, dy^\star.
\end{aligned}$$

Rearranging (A.17) gives the FIK identity

$$c_f(x^\star) = \underbrace{\frac{12}{Re_b}}_{\textbf{laminar}} \underbrace{-24\int_0^1 (1 - y^\star)\overline{u'v'}^\star(x^\star, y^\star)\, dy^\star}_{\textbf{turbulent contribution}} \underbrace{-12\int_0^1 (1 - y^\star)^2 S_D(x^\star, y^\star)\, dy^\star}_{\textbf{inhomogeneous and transient contribution}}, \tag{A.19}$$

where

$$S_D(x^\star, y^\star) = \check{I}_x + \frac{\partial \check{p}}{\partial x} + \frac{\partial \bar{u}^\star}{\partial t^\star}.$$

A.2 Two-dimensional turbulent boundary layers

Consider RANS for turbulent boundary layer flows in the streamwise direction

$$0 = \frac{\partial}{\partial y^\star}\left[\overline{u'v'}^\star - \frac{1}{Re_\delta}\frac{\partial \bar{u}^\star}{\partial y^\star} + \bar{u}^\star\bar{v}^\star\right] + \bar{I}_x^\star + \frac{\partial \bar{u}^\star}{\partial t^\star}, \tag{A.20}$$

where

$$\bar{I}_x^\star = \frac{\partial \bar{p}^\star}{\partial x^\star} + \frac{\partial \bar{u}^\star\bar{u}^\star}{\partial x^\star} - \frac{1}{Re_\delta}\frac{\partial^2 \bar{u}^\star}{\partial x^{\star 2}} + \frac{\partial \overline{u'u'}^\star}{\partial x^\star}, \tag{A.21}$$

where $\star$ denotes that a quantity is non-dimensionalised with δ and free-stream velocity U_∞. With assumptions that there is a (i) constant free stream velocity, (ii) homogeneity in the spanwise direction, (iii) $\left.\frac{\partial \bar{u}^\star}{\partial y^\star}\right|_{y^\star=1} \approx 0$, (iv) no-slip wall condition ie. $u|_{wall} = w|_{wall} = 0$ and (v) $\bar{v}(x,0,z,t) = 0$. An integration of (A.20) with respect to y gives

$$0 = \int_0^{y^\star} \frac{\partial}{\partial \gamma}\left[\overline{u'v'}^\star - \frac{1}{Re_\delta}\frac{\partial \bar{u}^\star}{\partial \gamma} + \bar{u}^\star\bar{v}^\star\right] + \bar{I}_x^\star + \frac{\partial \bar{u}^\star}{\partial t^\star}\, d\gamma, \tag{A.22}$$

$$0 = \overline{u'v'}^\star - \frac{1}{Re_\delta}\frac{\partial \bar{u}^\star}{\partial y^\star} + \left.\frac{1}{Re_\delta}\frac{\partial \bar{u}^\star}{\partial y^\star}\right|_w + \bar{u}^\star\bar{v}^\star + \int_0^{y^\star} \bar{I}_x^\star + \frac{\partial \bar{u}^\star}{\partial t^\star}\, d\gamma, \tag{A.23}$$

$$0 = \overline{u'v'}^\star - \frac{1}{Re_\delta}\frac{\partial \bar{u}^\star}{\partial y^\star} + \bar{u}^\star\bar{v}^\star + \frac{1}{2}c_f(x) + \int_0^{y^\star} \bar{I}_x^\star + \frac{\partial \bar{u}^\star}{\partial t^\star}\, d\gamma, \tag{A.24}$$

where

$$c_f(x) = \frac{\tau_w}{\frac{1}{2}\rho {U_b}^2} = \frac{2}{Re_\delta}\left.\frac{\partial \frac{\bar{u}*}{U_\infty}}{\partial \frac{y*}{\delta}}\right|_w = \frac{2}{Re_\delta}\left.\frac{\partial \bar{u}^\star}{\partial y^\star}\right|_w.$$

Integrations of (A.24) with respect to y and δ give

$$\begin{aligned} 0 = &\underbrace{\int_0^1\int_0^{y^\star} \overline{u'v'}^\star(x^\star,\phi) + \bar{u}^\star\bar{v}^\star(x^\star,\phi)\, d\phi dy^\star}_{a} + \underbrace{\int_0^1\int_0^{y^\star} -\frac{1}{Re_\delta}\frac{\partial \bar{u}^\star}{\partial y^\star}(x^\star,\phi)\, d\phi dy^\star}_{b} \\ &+ \underbrace{\int_0^1\int_0^{y^\star} \frac{1}{2}c_f(x)\, d\phi dy^\star}_{c} + \underbrace{\int_0^1\int_0^{y^\star}\int_0^{\phi} S_T(x^\star,\gamma)\, d\gamma d\phi dy^\star}_{d}, \end{aligned} \tag{A.25}$$

where

$$S_T(x^\star,\gamma) = \bar{I}_x^\star + \frac{\partial \bar{u}^\star}{\partial t^\star}. \tag{A.26}$$

(A.25a) is

$$\begin{aligned}
&\int_0^1 \int_0^{y^\star} \overline{u'v'}^\star(x^\star,\phi) + \bar{u}^\star\bar{v}^\star(x^\star,\phi)\, d\phi dy^\star \\
&= y^\star \int_0^{y^\star} \overline{u'v'}^\star(x^\star,\phi) + \bar{u}^\star\bar{v}^\star(x^\star,\phi)\, d\phi \Big|_0^1 - \int_0^1 y^\star \left[\overline{u'v'}^\star + \bar{u}^\star\bar{v}^\star\right](x^\star,y^\star)\, dy^\star, \\
&= \int_0^1 \overline{u'v'}^\star(x^\star,\phi) + \bar{u}^\star\bar{v}^\star(x^\star,\phi)\, d\phi - \int_0^1 y^\star \left[\overline{u'v'}^\star + \bar{u}^\star\bar{v}^\star\right](x^\star,y^\star)\, dy^\star, \\
&= \int_0^1 (1-y^\star)\left[\overline{u'v'}^\star + \bar{u}^\star\bar{v}^\star\right](x^\star,y^\star)\, dy^\star.
\end{aligned}$$

(A.25b) is

$$\int_0^1 \int_0^{y^\star} -\frac{1}{Re_\delta}\frac{\partial \bar{u}^\star}{\partial y^\star}(x^\star,\phi)\, d\phi dy^\star = \frac{1}{Re_\delta}\int_0^1 \bar{u}^\star(x^\star,y^\star)\, dy^\star = \frac{1}{Re_\delta}\delta_d - \frac{1}{Re_\delta}.$$

(A.25c) is

$$\int_0^1 \int_0^{y^\star} \frac{1}{2} c_f(x)\, d\phi dy^\star = \int_0^1 \frac{1}{2} y^\star c_f(x)\, dy^\star = \frac{1}{4} c_f(x).$$

(A.25d) is

$$\begin{aligned}
&\int_0^1 \int_0^{y^\star} \int_0^{\phi} S_T(x^\star,\gamma)\, d\gamma d\phi dy^\star \\
&= y^\star \int_0^{y^\star} \int_0^{\phi} S_T(x^\star,\gamma)\, d\gamma d\phi \Big|_0^1 - \int_0^1 y^\star \int_0^{y^\star} S_T(x^\star,\gamma)\, d\gamma dy^\star, \\
&= \underbrace{\int_0^1 \int_0^{\phi} S_T(x^\star,\gamma)\, d\gamma d\phi}_{d1} - \underbrace{\int_0^1 y^\star \int_0^{y^\star} S_T(x^\star,\gamma)\, d\gamma dy^\star}_{d2}.
\end{aligned} \tag{A.27}$$

(A.27d1) is

$$\int_0^1 \int_0^\phi S_T(x^\star,\gamma)\,d\gamma d\phi = \phi \int_0^\phi S_T(x^\star,\gamma)\,d\gamma\Big|_0^1 - \int_0^1 \phi\, S_T(x^\star,\phi)\,d\phi,$$
$$= \int_0^1 S_T(x^\star,y^\star)\,dy^\star - \int_0^1 y^\star\, S_T(x^\star,y^\star)\,dy^\star.$$

(A.27d2) is

$$\int_0^1 y^\star \int_0^{y^\star} S_T(x^\star,\gamma)\,d\gamma dy^\star$$
$$= y^{\star 2} \int_0^{y^\star} S_T(x^\star,\gamma)\,d\gamma\Big|_0^1 - \int_0^1 y^\star \frac{\partial}{\partial y^\star}(y^\star \int_0^{y^\star} S_T(x^\star,\gamma)\,d\gamma)\,dy^\star,$$
$$= \int_0^1 S_T(x^\star,y^\star)\,dy^\star - \int_0^1 y^\star \int_0^{y^\star} S_T(x^\star,\gamma)\,d\gamma dy - \int_0^1 y^{\star 2} S_T(x^\star,y^\star)\,dy^\star.$$

Rearrange so that

$$\int_0^1 y^\star \int_0^{y^\star} S_T(x^\star,\phi)\,d\phi dy^\star = \frac{1}{2}\int_0^1 (1-y^{\star 2}) S_T(x^\star,y^\star)\,dy^\star.$$

Hence, (A.27) becomes

$$\int_0^1 \int_0^{y^\star} \int_0^\phi S_T(x^\star,\gamma)\,d\gamma d\phi dy^\star$$
$$= \int_0^1 S_T(x^\star,y^\star)\,dy^\star - \int_0^1 y^\star S_T(x^\star,y^\star)\,dy^\star - \frac{1}{2}\int_0^1 (1-y^{\star 2}) S_T(x^\star,y^\star)\,dy^\star,$$
$$= \frac{1}{2}\int_0^1 (1-y^\star)^2\, S_T(x^\star,y^\star)\,dy^\star. \qquad \text{(A.28)}$$

Rearranging (A.25) gives the FIK identity for incompressible two-dimensional TBL

$$c_f(x^\star) = \underbrace{\frac{4(1-\delta_d)}{Re_\delta}(x)}_{\textbf{mass flow deficit}} + \underbrace{4\int_0^1 (1-y^\star)\left(-\overline{u'v'}^\star(x^\star,y^\star)\right)dy^\star}_{\textbf{turbulent contribution}} + \underbrace{4\int_0^1 (1-y^\star)\left(-\bar{u}^\star\bar{v}^\star(x^\star,y^\star)\right)dy^\star}_{\textbf{mean convection}} - \underbrace{2\int_0^1 (1-y^\star)^2 S_T(x^\star,y^\star)\,dy^\star}_{\substack{\textbf{spatial development,}\\ \textbf{mean pressure gradient}\\ \textbf{and transient contribution}}}, \tag{A.29}$$

where

$$S_T(x^\star,y^\star) = \bar{I}_x^\star + \frac{\partial \bar{u}^\star}{\partial t^\star}. \tag{A.30}$$

Appendix B

Fourier mode decomposition of the Reynolds stress transport equation

The large- and small-scale Reynolds stress transport equations defined by (2.39) and (2.40) were proposed by Kawata and Alfredsson [104]. We provide here one of the derivation. Suppose the velocity fluctuations are decomposed into large-scale and small-scale components by their spanwise Fourier wavenumber and are given by

$$u_i''(\boldsymbol{x},t) = u_i''^{,\mathrm{L}}(k_z,\boldsymbol{x},t) + u_i''^{,\mathrm{S}}(k_z,\boldsymbol{x},t), \tag{B.1}$$

where k_z denotes the cut-off wavenumber. There is no overlapping wavenumber between them, therefore their cross-correlation is zero. The large-scale $u_i''^{,\mathrm{L}}$ and small-scale $u_i''^{,\mathrm{S}}$ velocities are

$$\left\langle u_i''^{,\mathrm{L}} u_j''^{,\mathrm{S}} \right\rangle (k_z,x,y) = 0, \tag{B.2}$$

$$\left\langle u_i'' u_j'' \right\rangle (k_z,x,y) = \left\langle u_i''^{,\mathrm{L}} u_j''^{,\mathrm{L}} \right\rangle (k_z,x,y) + \left\langle u_i''^{,\mathrm{S}} u_j''^{,\mathrm{S}} \right\rangle (k_z,x,y). \tag{B.3}$$

Considering flow that satisfies the incompressible Navier-Stokes equations:

$$\underbrace{\frac{\partial}{\partial t}(U_i + u_i'')}_{a} + \underbrace{(U_k + u_k'')\frac{\partial}{\partial x_k}(U_i + u_i'')}_{b} = \underbrace{-\frac{1}{\rho}\frac{\partial}{\partial x_i}(P + p'')}_{c} + \underbrace{\nu\Delta(U_i + u_i'')}_{d}, \tag{B.4}$$

and

$$\frac{\partial U_i}{\partial x_i} = 0, \quad \frac{\partial u_i''}{\partial x_i} = 0. \tag{B.5}$$

Multiplying (B.4a) by $u_j''^{,\mathrm{L}}$ and taking the average, we obtain

$$\left\langle u_j''^{,\mathrm{L}} \frac{\partial}{\partial t}\left(U_i + u_i''\right)\right\rangle(k_z,x,y) = \left\langle u_j''^{,\mathrm{L}} \frac{\partial u_i''}{\partial t}\right\rangle = \left\langle u_j''^{,\mathrm{L}} \frac{\partial u_i''^{,\mathrm{L}}}{\partial t}\right\rangle + \left\langle u_j''^{,\mathrm{L}} \frac{\partial u_i''^{,\mathrm{S}}}{\partial t}\right\rangle. \tag{B.6}$$

By interchanging i and j in (B.6) and adding up the two terms, we obtain the temporal term

$$\left\langle u_j''^{,\mathrm{L}} \frac{\partial u_i''^{,\mathrm{L}}}{\partial t}\right\rangle + \left\langle u_j''^{,\mathrm{L}} \frac{\partial u_i''^{,\mathrm{S}}}{\partial t}\right\rangle + \left\langle u_i''^{,\mathrm{L}} \frac{\partial u_j''^{,\mathrm{L}}}{\partial t}\right\rangle + \left\langle u_i''^{,\mathrm{L}} \frac{\partial u_j''^{,\mathrm{S}}}{\partial t}\right\rangle$$

$$= \left\langle \frac{\partial u_i''^{,\mathrm{L}} u_j''^{,\mathrm{L}}}{\partial t}\right\rangle + \underbrace{\left\langle u_j''^{,\mathrm{L}} \frac{\partial u_i''^{,\mathrm{S}}}{\partial t}\right\rangle + \left\langle u_i''^{,\mathrm{L}} \frac{\partial u_j''^{,\mathrm{S}}}{\partial t}\right\rangle}_{0}. \tag{B.7}$$

Multiplying (B.4b) by $u_j''^{,\mathrm{L}}$ and taking the average, we obtain

$$\left\langle u_j''^{,\mathrm{L}} \left(U_k + u_k''\right) \frac{\partial}{\partial x_k}\left(U_i + u_i''\right)\right\rangle(k_z,x,y)$$

$$= \underbrace{\left\langle u_j''^{,\mathrm{L}}\right\rangle \left\langle U_k \frac{\partial U_i}{\partial x_k}\right\rangle}_{0} + \left\langle U_k\right\rangle \left\langle u_j''^{,\mathrm{L}} \frac{\partial u_i''}{\partial x_k}\right\rangle + \left\langle \frac{\partial U_i}{\partial x_k}\right\rangle \left\langle u_j''^{,\mathrm{L}} u_k''\right\rangle + \left\langle u_j''^{,\mathrm{L}} u_k'' \frac{\partial u_i''}{\partial x_k}\right\rangle.$$

Hence,

$$\left\langle u_j''^{,\mathrm{L}} \left(U_k + u_k''\right) \frac{\partial}{\partial x_k}\left(U_i + u_i''\right)\right\rangle(k_z,x,y) = \underbrace{U_k \left\langle u_j''^{,\mathrm{L}} \frac{\partial u_i''}{\partial x_k}\right\rangle}_{a} + \underbrace{\frac{\partial U_i}{\partial x_k} \left\langle u_j''^{,\mathrm{L}} u_k''\right\rangle}_{b} + \underbrace{\left\langle u_j''^{,\mathrm{L}} u_k'' \frac{\partial u_i''}{\partial x_k}\right\rangle}_{c}. \tag{B.8}$$

Using (B.1), the term (B.8a) can be written as

$$U_k \left\langle u_j''^{,\mathrm{L}} \frac{\partial u_i''}{\partial x_k}\right\rangle(k_z,x,y) = U_k \left\langle u_j''^{,\mathrm{L}} \frac{\partial u_i''^{,\mathrm{L}}}{\partial x_k}\right\rangle + U_k \left\langle u_j''^{,\mathrm{L}} \frac{\partial u_i''^{,\mathrm{S}}}{\partial x_k}\right\rangle. \tag{B.9}$$

By interchanging i and j in (B.9) and adding up the two terms, we obtain the convection term

$$U_k\Big\langle u_j''^{,\mathrm{L}}\frac{\partial u_i''^{,\mathrm{L}}}{\partial x_k}\Big\rangle + U_k\Big\langle u_j''^{,\mathrm{L}}\frac{\partial u_i''^{,\mathrm{S}}}{\partial x_k}\Big\rangle + U_k\Big\langle u_i''^{,\mathrm{L}}\frac{\partial u_j''^{,\mathrm{L}}}{\partial x_k}\Big\rangle + U_k\Big\langle u_i''^{,\mathrm{L}}\frac{\partial u_j''^{,\mathrm{S}}}{\partial x_k}\Big\rangle$$

$$= U_k\Big\langle \frac{\partial u_i''^{,\mathrm{L}}u_j''^{,\mathrm{L}}}{\partial x_k}\Big\rangle + \underbrace{U_k\Big\langle u_j''^{,\mathrm{L}}\frac{\partial u_i''^{,\mathrm{S}}}{\partial x_k} + u_i''^{,\mathrm{L}}\frac{\partial u_j''^{,\mathrm{S}}}{\partial x_k}\Big\rangle}_{0}. \tag{B.10}$$

Next, using (B.1), the term (B.8b) can be written as

$$\frac{\partial U_i}{\partial x_k}\big\langle u_j''^{,\mathrm{L}}u_k''\big\rangle(k_z,x,y) = \frac{\partial U_i}{\partial x_k}\big\langle u_j''^{,\mathrm{L}}u_k''^{,\mathrm{L}}\big\rangle + \underbrace{\frac{\partial U_i}{\partial x_k}\big\langle u_j''^{,\mathrm{L}}u_k''^{,\mathrm{S}}\big\rangle}_{0} = \frac{\partial U_i}{\partial x_k}\big\langle u_j''^{,\mathrm{L}}u_k''^{,\mathrm{L}}\big\rangle. \tag{B.11}$$

By interchanging i and j in (B.11) and adding up the two terms, we obtain the production term

$$\frac{\partial U_i}{\partial x_k}\big\langle u_j''^{,\mathrm{L}}u_k''^{,\mathrm{L}}\big\rangle(k_z,x,y) + \frac{\partial U_j}{\partial x_k}\big\langle u_i''^{,\mathrm{L}}u_k''^{,\mathrm{L}}\big\rangle(k_z,x,y). \tag{B.12}$$

Next, using (B.1), the term (B.8c) can be written as

$$\big\langle u_j''^{,\mathrm{L}}u_k''\frac{\partial u_i''}{\partial x_k}\big\rangle(k_z,x,y) = \underbrace{\big\langle u_j''^{,\mathrm{L}}u_k''^{,\mathrm{L}}\frac{\partial u_i''^{,\mathrm{L}}}{\partial x_k}\big\rangle}_{a} + \underbrace{\big\langle u_j''^{,\mathrm{L}}u_k''^{,\mathrm{S}}\frac{\partial u_i''^{,\mathrm{L}}}{\partial x_k}\big\rangle}_{b}$$
$$+ \underbrace{\big\langle u_j''^{,\mathrm{L}}u_k''^{,\mathrm{L}}\frac{\partial u_i''^{,\mathrm{S}}}{\partial x_k}\big\rangle}_{c} + \underbrace{\big\langle u_j''^{,\mathrm{L}}u_k''^{,\mathrm{S}}\frac{\partial u_i''^{,\mathrm{S}}}{\partial x_k}\big\rangle}_{d}. \tag{B.13}$$

By interchanging i and j in (B.13a) and adding up the two terms, we obtain

$$\big\langle u_j''^{,\mathrm{L}}u_k''^{,\mathrm{L}}\frac{\partial u_i''^{,\mathrm{L}}}{\partial x_k}\big\rangle + \big\langle u_i''^{,\mathrm{L}}u_k''^{,\mathrm{L}}\frac{\partial u_j''^{,\mathrm{L}}}{\partial x_k}\big\rangle = \big\langle \frac{\partial u_i''^{,\mathrm{L}}u_j''^{,\mathrm{L}}u_k''^{,\mathrm{L}}}{\partial x_k}\big\rangle - \underbrace{\big\langle u_i''^{,\mathrm{L}}u_j''^{,\mathrm{L}}\frac{\partial u_k''^{,\mathrm{L}}}{\partial x_k}\big\rangle}_{0},$$
$$= \big\langle \frac{\partial u_i''^{,\mathrm{L}}u_j''^{,\mathrm{L}}u_k''^{,\mathrm{L}}}{\partial x_k}\big\rangle(k_z,x,y). \tag{B.14}$$

By interchanging i and j in (B.13b) and adding up the two terms, we obtain

$$\left\langle u_j''^{,\mathrm{L}} u_k''^{,\mathrm{S}} \frac{\partial u_i''^{,\mathrm{L}}}{\partial x_k} \right\rangle + \left\langle u_i''^{,\mathrm{L}} u_k''^{,\mathrm{S}} \frac{\partial u_j''^{,\mathrm{L}}}{\partial x_k} \right\rangle = \left\langle \frac{\partial u_i''^{,\mathrm{L}} u_j''^{,\mathrm{L}} u_k''^{,\mathrm{S}}}{\partial x_k} \right\rangle - \underbrace{\left\langle u_i''^{,\mathrm{L}} u_j''^{,\mathrm{L}} \frac{\partial u_k''^{,\mathrm{S}}}{\partial x_k} \right\rangle}_{0},$$

$$= \left\langle \frac{\partial u_i''^{,\mathrm{L}} u_j''^{,\mathrm{L}} u_k''^{,\mathrm{S}}}{\partial x_k} \right\rangle (k_z, x, y). \tag{B.15}$$

By interchanging i and j in (B.13c) and adding up the two terms, we obtain

$$\left\langle u_j''^{,\mathrm{L}} u_k''^{,\mathrm{L}} \frac{\partial u_i''^{,\mathrm{S}}}{\partial x_k} \right\rangle (k_z, x, y) + \left\langle u_i''^{,\mathrm{L}} u_k''^{,\mathrm{L}} \frac{\partial u_j''^{,\mathrm{S}}}{\partial x_k} \right\rangle (k_z, x, y). \tag{B.16}$$

By interchanging i and j in (B.13d) and adding up the two terms, we obtain

$$\left\langle u_j''^{,\mathrm{L}} u_k''^{,\mathrm{S}} \frac{\partial u_i''^{,\mathrm{S}}}{\partial x_k} \right\rangle + \left\langle u_i''^{,\mathrm{L}} u_k''^{,\mathrm{S}} \frac{\partial u_j''^{,\mathrm{S}}}{\partial x_k} \right\rangle = \left\langle \frac{\partial u_i''^{,\mathrm{S}} u_j''^{,\mathrm{L}} u_k''^{,\mathrm{S}}}{\partial x_k} \right\rangle - \left\langle u_i''^{,\mathrm{S}} u_k''^{,\mathrm{S}} \frac{\partial u_j''^{,\mathrm{L}}}{\partial x_k} \right\rangle$$

$$+ \left\langle \frac{\partial u_i''^{,\mathrm{L}} u_j''^{,\mathrm{S}} u_k''^{,\mathrm{S}}}{\partial x_k} \right\rangle - \left\langle u_j''^{,\mathrm{S}} u_k''^{,\mathrm{S}} \frac{\partial u_i''^{,\mathrm{L}}}{\partial x_k} \right\rangle. \tag{B.17}$$

Multiplying (B.4c) by $u_j''^{,\mathrm{L}}$ and taking the average, by interchanging i with j and adding up the two terms, we obtain

$$-\frac{1}{\rho} \left[\left\langle \frac{\partial p''^{,\mathrm{L}}}{\partial x_i} u_j''^{,\mathrm{L}} \right\rangle + \left\langle \frac{\partial p''^{,\mathrm{L}}}{\partial x_j} u_i''^{,\mathrm{L}} \right\rangle \right] (k_z, x, y). \tag{B.18}$$

Multiplying (B.4d) by $u_j''^{,\mathrm{L}}$ and taking the average, we obtain

$$\nu \left\langle u_j''^{,\mathrm{L}} \Delta \left(U_i + u_i'' \right) \right\rangle (k_z, x, y) = \nu \left\langle u_j''^{,\mathrm{L}} \Delta u_i''^{,\mathrm{L}} \right\rangle + \nu \left\langle u_j''^{,\mathrm{L}} \Delta u_i''^{,\mathrm{S}} \right\rangle. \tag{B.19}$$

By interchanging i with j in (B.19) and adding up the two terms, we obtain

$$\underbrace{\nu \left\langle u_j''^{,\mathrm{L}} \Delta u_i''^{,\mathrm{L}} \right\rangle + \nu \left\langle u_i''^{,\mathrm{L}} \Delta u_j''^{,\mathrm{L}} \right\rangle}_{} + \underbrace{\nu \left\langle u_j''^{,\mathrm{L}} \Delta u_i''^{,\mathrm{S}} \right\rangle + \nu \left\langle u_i''^{,\mathrm{L}} \Delta u_j''^{,\mathrm{S}} \right\rangle}_{0}$$

$$= \nu \left\langle \Delta u_j''^{,\mathrm{L}} u_i''^{,\mathrm{L}} \right\rangle (k_z, x, y) - 2\nu \left\langle \frac{\partial u_i''^{,\mathrm{L}}}{\partial x_k} \frac{\partial u_j''^{,\mathrm{L}}}{\partial x_k} \right\rangle (k_z, x, y). \tag{B.20}$$

Summarising all the terms, we obtain

$$\underbrace{\Big\langle \frac{\partial u_i''^{,\mathrm{L}} u_j''^{,\mathrm{L}}}{\partial t} \Big\rangle}_{(B.7)} + \underbrace{U_k \Big\langle \frac{\partial u_i''^{,\mathrm{L}} u_j''^{,\mathrm{L}}}{\partial x_k} \Big\rangle}_{(B.10)} = \underbrace{-\frac{\partial U_i}{\partial x_k}\big\langle u_j''^{,\mathrm{L}} u_k''^{,\mathrm{L}}\big\rangle - \frac{\partial U_j}{\partial x_k}\big\langle u_i''^{,\mathrm{L}} u_k''^{,\mathrm{L}}\big\rangle}_{(B.12)}$$
$$\underbrace{-\Big\langle u_j''^{,\mathrm{L}} u_k''^{,\mathrm{L}} \frac{\partial u_i''^{,\mathrm{S}}}{\partial x_k}\Big\rangle - \Big\langle u_i''^{,\mathrm{L}} u_k''^{,\mathrm{L}} \frac{\partial u_j''^{,\mathrm{S}}}{\partial x_k}\Big\rangle}_{(B.16)} \underbrace{-\Big\langle \frac{\partial u_i''^{,\mathrm{L}} u_j''^{,\mathrm{L}} u_k''^{,\mathrm{L}}}{\partial x_k}\Big\rangle}_{(B.14)} \underbrace{-\Big\langle \frac{\partial u_i''^{,\mathrm{L}} u_j''^{,\mathrm{L}} u_k''^{,\mathrm{S}}}{\partial x_k}\Big\rangle}_{(B.15)}$$
$$\underbrace{-\Big\langle \frac{\partial u_i''^{,\mathrm{S}} u_j''^{,\mathrm{L}} u_k''^{,\mathrm{S}}}{\partial x_k}\Big\rangle + \Big\langle u_i''^{,\mathrm{S}} u_k''^{,\mathrm{S}} \frac{\partial u_j''^{,\mathrm{L}}}{\partial x_k}\Big\rangle - \Big\langle \frac{\partial u_i''^{,\mathrm{L}} u_j''^{,\mathrm{S}} u_k''^{,\mathrm{S}}}{\partial x_k}\Big\rangle + \Big\langle u_j''^{,\mathrm{S}} u_k''^{,\mathrm{S}} \frac{\partial u_i''^{,\mathrm{L}}}{\partial x_k}\Big\rangle}_{(B.17)}$$
$$\underbrace{-\frac{1}{\rho}\Big[\Big\langle \frac{\partial p''^{,\mathrm{L}}}{\partial x_i} u_j''^{,\mathrm{L}}\Big\rangle + \Big\langle \frac{\partial p''^{,\mathrm{L}}}{\partial x_j} u_i''^{,\mathrm{L}}\Big\rangle\Big]}_{(B.18)} + \underbrace{\nu\big\langle \Delta u_j''^{,\mathrm{L}} u_i''^{,\mathrm{L}}\big\rangle - 2\nu\Big\langle \frac{\partial u_i''^{,\mathrm{L}}}{\partial x_k}\frac{\partial u_j''^{,\mathrm{L}}}{\partial x_k}\Big\rangle}_{(B.20)}.$$

We may rewrite the terms (B.7) and (B.10) as

$$\frac{D\big\langle u_i''^{,\mathrm{L}} u_j''^{,\mathrm{L}}\big\rangle}{Dt}(k_z,x,y). \tag{B.21}$$

(B.12) is

$$P_{ij}^{L}(k_z,x,y) = -\frac{\partial U_i}{\partial x_k}\big\langle u_j''^{,\mathrm{L}} u_k''^{,\mathrm{L}}\big\rangle - \frac{\partial U_j}{\partial x_k}\big\langle u_i''^{,\mathrm{L}} u_k''^{,\mathrm{L}}\big\rangle. \tag{B.22}$$

(B.14) to (B.17) are

$$\underbrace{-\Big\langle \frac{\partial u_i''^{,\mathrm{L}} u_j''^{,\mathrm{L}} u_k''^{,\mathrm{L}}}{\partial x_k}\Big\rangle - \Big\langle \frac{\partial u_i''^{,\mathrm{L}} u_j''^{,\mathrm{L}} u_k''^{,\mathrm{S}}}{\partial x_k}\Big\rangle - \Big\langle \frac{\partial u_i''^{,\mathrm{S}} u_j''^{,\mathrm{L}} u_k''^{,\mathrm{S}}}{\partial x_k}\Big\rangle - \Big\langle \frac{\partial u_i''^{,\mathrm{L}} u_j''^{,\mathrm{S}} u_k''^{,\mathrm{S}}}{\partial x_k}\Big\rangle}_{D_{ij}^{t,L}(k_z,x,y)}, \tag{B.23}$$

$$\underbrace{-\Big\langle u_j''^{,\mathrm{L}} u_k''^{,\mathrm{L}} \frac{\partial u_i''^{,\mathrm{S}}}{\partial x_k}\Big\rangle - \Big\langle u_i''^{,\mathrm{L}} u_k''^{,\mathrm{L}} \frac{\partial u_j''^{,\mathrm{S}}}{\partial x_k}\Big\rangle + \Big\langle u_i''^{,\mathrm{S}} u_k''^{,\mathrm{S}} \frac{\partial u_j''^{,\mathrm{L}}}{\partial x_k}\Big\rangle + \Big\langle u_j''^{,\mathrm{S}} u_k''^{,\mathrm{S}} \frac{\partial u_i''^{,\mathrm{L}}}{\partial x_k}\Big\rangle}_{-Tr_{ij}(k_z,x,y)}. \tag{B.24}$$

(B.18) is

$$\Phi_{ij}^{L}(k_z,x,y) = -\frac{1}{\rho}\Big[\Big\langle \frac{\partial p''^{,\mathrm{L}}}{\partial x_i} u_j''^{,\mathrm{L}}\Big\rangle + \Big\langle \frac{\partial p''^{,\mathrm{L}}}{\partial x_j} u_i''^{,\mathrm{L}}\Big\rangle\Big]. \tag{B.25}$$

(B.20) is

$$\underbrace{\nu\left\langle \Delta u_j''^{,\mathrm{L}} u_i''^{,\mathrm{L}} \right\rangle}_{D_{ij}^{\nu,L}(k_z,x,y)} \underbrace{-2\nu\left\langle \frac{\partial u_i''^{,\mathrm{L}}}{\partial x_k}\frac{\partial u_j''^{,\mathrm{L}}}{\partial x_k} \right\rangle}_{\epsilon_{ij}^{L}(k_z,x,y)}. \tag{B.26}$$

Finally, we obtain

$$\frac{D\left\langle u_i''^{,\mathrm{L}} u_j''^{,\mathrm{L}} \right\rangle}{Dt}(k_z,x,y) = P_{ij}^{L} + D_{ij}^{t,L} + \Phi_{ij}^{L} + D_{ij}^{\nu,L} - \epsilon_{ij}^{L} - Tr_{ij} \tag{B.27}$$

The transport equation for small-scale $\left\langle u_i''^{,\mathrm{S}} u_j''^{,\mathrm{S}} \right\rangle$ can be obtained by using (B.27) and is given by

$$\frac{D\left\langle u_i''^{,\mathrm{S}} u_j''^{,\mathrm{S}} \right\rangle}{Dt} = \frac{D\left\langle u_i'' u_j'' \right\rangle}{Dt} - \frac{D\left\langle u_i''^{,\mathrm{L}} u_j''^{,\mathrm{L}} \right\rangle}{Dt}. \tag{B.28}$$

Appendix C

Triple decomposed Reynolds stress transport equations

The Reynolds decomposition distinguishes between the mean and fluctuating components:

$$u_i(\boldsymbol{x},t) = \overline{u}(\boldsymbol{x}) + u_i'(\boldsymbol{x},t), \tag{C.1}$$

Flows that exhibit periodic states (e.g. a periodic flow on roughness surfaces), the total velocity fluctuations can be decomposed into a turbulent component and a coherent component [41, 42, 153]:

$$u_i(\boldsymbol{x},t) = U_i(x,y) + u_i'(\boldsymbol{x},t) + \tilde{u}_i(\boldsymbol{x}), \tag{C.2}$$

The velocity fluctuations can be expressed as:

$$u_i(\boldsymbol{x},t) - U_i(x,y) = \underbrace{u_i''(\boldsymbol{x},t)}_{\text{total}} = \underbrace{u_i'(\boldsymbol{x},t)}_{\text{turbulent}} + \underbrace{\tilde{u}_i(\boldsymbol{x})}_{\text{coherent}}. \tag{C.3}$$

Considering a flow that satisfies the incompressible Navier-Stokes equations:

$$\underbrace{\frac{\partial}{\partial t}(U_i + u_i'')}_{a} + \underbrace{(U_k + u_k'')\frac{\partial}{\partial x_k}(U_i + u_i'')}_{b} = \underbrace{-\frac{1}{\rho}\frac{\partial}{\partial x_i}(P + p'')}_{c} + \underbrace{\nu\Delta(U_i + u_i'')}_{d}, \tag{C.4}$$

and

$$\frac{\partial U_i}{\partial x_i} = 0, \quad \frac{\partial u_i'}{\partial x_i} = 0, \quad \frac{\partial \tilde{u}_i}{\partial x_i} = 0. \tag{C.5}$$

C.1 Total kinetic energy transport

Multiplying (C.4a) by u_j'' and taking the time average, by interchanging i and j and adding up the two terms, we obtain

$$\overline{u_j'' \frac{\partial}{\partial t}\left(U_i + u_i''\right)}(\boldsymbol{x}) + \overline{u_i'' \frac{\partial}{\partial t}\left(U_j + u_j''\right)}(\boldsymbol{x}) = \overline{u_j'' \frac{\partial u_i''}{\partial t}} + \overline{u_i'' \frac{\partial u_j''}{\partial t}} = \overline{\frac{\partial u_i'' u_j''}{\partial t}}. \tag{C.6}$$

Multiplying (C.4b) by u_j'' and taking the time average, we obtain

$$\begin{aligned}\overline{u_j''\left(U_k + u_k''\right)\frac{\partial}{\partial x_k}\left(U_i + u_i''\right)}(\boldsymbol{x}) &= \overline{u_j'' U_k \frac{\partial U_i}{\partial x_k}} + \overline{u_j'' U_k \frac{\partial u_i''}{\partial x_k}} + \overline{u_j'' u_k'' \frac{\partial U_i}{\partial x_k}} + \overline{u_j'' u_k'' \frac{\partial u_i''}{\partial x_k}}, \\ &= \underbrace{\tilde{u}_j U_k \frac{\partial U_i}{\partial x_k}}_{a} + \underbrace{U_k \overline{u_j'' \frac{\partial u_i''}{\partial x_k}}}_{b} + \underbrace{\overline{u_j'' u_k''} \frac{\partial U_i}{\partial x_k}}_{c} + \underbrace{\overline{u_j'' u_k'' \frac{\partial u_i''}{\partial x_k}}}_{d}.\end{aligned} \tag{C.7}$$

By interchanging i and j and adding up the two terms, we obtain, respectively,

$$\begin{aligned}&(C.7a): \tilde{u}_j U_k \frac{\partial U_i}{\partial x_k} + \tilde{u}_i U_k \frac{\partial U_j}{\partial x_k}, \quad (C.7b): U_k \overline{\frac{\partial u_i'' u_j''}{\partial x_k}}, \\ &(C.7c): \overline{u_j'' u_k''} \frac{\partial U_i}{\partial x_k} + \overline{u_i'' u_k''} \frac{\partial U_j}{\partial x_k}, \quad (C.7d): \overline{u_j'' u_k'' \frac{\partial u_i''}{\partial x_k}} + \overline{u_i'' u_k'' \frac{\partial u_j''}{\partial x_k}} = \overline{\frac{\partial u_i'' u_j'' u_k''}{\partial x_k}}.\end{aligned} \tag{C.8}$$

Multiplying (C.4c) by u_j'' and taking the time average, by interchanging i and j and adding up the two terms, we obtain

$$\begin{aligned}&-\frac{1}{\rho}\left[\overline{\frac{\partial}{\partial x_i}(P + p'') \cdot u_j''} + \overline{\frac{\partial}{\partial x_j}(P + p'') \cdot u_i''}\right](\boldsymbol{x}) \\ &\quad = -\frac{1}{\rho}\left[\frac{\partial P}{\partial x_i} \cdot \tilde{u}_j + \frac{\partial P}{\partial x_j} \cdot \tilde{u}_i\right] - \frac{1}{\rho}\left[\overline{\frac{\partial p''}{\partial x_i} \cdot u_j''} + \overline{\frac{\partial p''}{\partial x_j} \cdot u_i''}\right].\end{aligned} \tag{C.9}$$

Multiplying (C.4d) by u_j'' and taking the time average, by interchanging i and j and adding up the two terms, we obtain

$$\nu\overline{\Delta\left(U_i+u_i''\right)\cdot u_j''}(\boldsymbol{x})+\nu\overline{\Delta\left(U_j+u_j''\right)\cdot u_i''}(\boldsymbol{x})=\nu\Delta U_i\cdot\tilde{u}_j+\nu\Delta U_j\cdot\tilde{u}_i+\nu\overline{\Delta u_i''u_j''}-2\nu\overline{\frac{\partial u_i''}{\partial x_k}\frac{\partial u_j''}{\partial x_k}}. \tag{C.10}$$

Finally, the kinetic energy transport for total fluctuation (2.49) is given by (i.e. i=j)

$$\begin{aligned}&\frac{1}{2}\overline{\frac{\partial u_i''u_i''}{\partial t}}(\boldsymbol{x})+\underbrace{\tilde{u}_iU_k\frac{\partial U_i}{\partial x_k}+\frac{U_k}{2}\overline{\frac{\partial u_i''u_i''}{\partial x_k}}}_{C''(\boldsymbol{x})}=\underbrace{-\overline{u_i''u_k''}\frac{\partial U_i}{\partial x_k}}_{\mathcal{P}''(\boldsymbol{x})}\underbrace{-\frac{1}{2}\frac{\partial}{\partial x_k}\overline{u_i''u_i''u_k''}}_{\mathcal{D}''(\boldsymbol{x})}\\&\underbrace{-\frac{1}{\rho}\left[\frac{\partial P}{\partial x_i}\cdot\tilde{u}_i+\overline{\frac{\partial p''}{\partial x_i}\cdot u_i''}\right]}_{\varphi''(\boldsymbol{x})}+\underbrace{\nu\Delta U_i\cdot\tilde{u}_i+\frac{1}{2}\nu\overline{\Delta u_i''u_i''}}_{\mathcal{D}_\nu''(\boldsymbol{x})}-\underbrace{\nu\overline{\frac{\partial u_i''}{\partial x_k}\frac{\partial u_i''}{\partial x_k}}}_{\epsilon''(\boldsymbol{x})}.\end{aligned} \tag{C.11}$$

C.2 Turbulent kinetic energy transport

Multiplying (C.4a) by u_j' and taking the time average, by interchanging i and j and adding up the two terms, we obtain

$$\overline{u_j'\frac{\partial}{\partial t}\left(U_i+u_i''\right)}(\boldsymbol{x})+\overline{u_i'\frac{\partial}{\partial t}\left(U_j+u_j''\right)}(\boldsymbol{x})=\overline{u_j'\frac{\partial u_i''}{\partial t}}+\overline{u_i'\frac{\partial u_j''}{\partial t}}=\overline{\frac{\partial u_i'u_j'}{\partial t}}. \tag{C.12}$$

Multiplying (C.4b) by u_j' and taking the time average.

$$\begin{aligned}\overline{u_j'\left(U_k+u_k''\right)\frac{\partial}{\partial x_k}\left(U_i+u_i''\right)}(\boldsymbol{x})&=\overline{u_j'U_k\frac{\partial U_i}{\partial x_k}}+\overline{u_j'U_k\frac{\partial u_i''}{\partial x_k}}+\overline{u_j'u_k''\frac{\partial U_i}{\partial x_k}}+\overline{u_j'u_k''\frac{\partial u_i''}{\partial x_k}},\\&=\underbrace{U_k\overline{u_j'\frac{\partial u_i''}{\partial x_k}}}_{a}+\underbrace{\overline{u_j'u_k''}\frac{\partial U_i}{\partial x_k}}_{b}+\underbrace{\overline{u_j'u_k''\frac{\partial u_i''}{\partial x_k}}}_{c}.\end{aligned} \tag{C.13}$$

By interchanging i and j in each term and adding up the two terms, we obtain, respectively,

$$(C.13a): U_k \overline{\frac{\partial u_i' u_j'}{\partial x_k}}, \quad (C.13b): \overline{u_j' u_k'} \frac{\partial U_i}{\partial x_k} + \overline{u_i' u_k'} \frac{\partial U_j}{\partial x_k},$$
$$(C.13c): \overline{\frac{\partial u_i' u_j' u_k'}{\partial x_k}} + \left(\overline{u_i' \frac{\partial u_j'}{\partial x_k}} + \overline{u_j' \frac{\partial u_i'}{\partial x_k}} \right) \cdot \tilde{u}_k + \overline{u_j' u_k'} \frac{\partial \tilde{u}_i}{\partial x_k} + \overline{u_i' u_k'} \frac{\partial \tilde{u}_j}{\partial x_k}. \tag{C.14}$$

Multiplying (C.4c) by u_j' and taking the time average, by interchanging i and j and adding up the two terms, we obtain

$$-\frac{1}{\rho} \left[\overline{\frac{\partial}{\partial x_i} \left(P + p'' \right) \cdot u_j'} + \overline{\frac{\partial}{\partial x_j} \left(P + p'' \right) \cdot u_i'} \right] (\boldsymbol{x}) = -\frac{1}{\rho} \left[\overline{\frac{\partial p'}{\partial x_i} \cdot u_j'} + \overline{\frac{\partial p'}{\partial x_j} \cdot u_i'} \right]. \tag{C.15}$$

Multiplying (C.4d) by u_j' and taking the time average, by interchanging i and j and adding up the two terms, we obtain

$$\nu \overline{\Delta \left(U_i + u_i'' \right) \cdot u_j'} \left(\boldsymbol{x} \right) + \nu \overline{\Delta \left(U_j + u_j'' \right) \cdot u_i'} (\boldsymbol{x}) = \nu \overline{\Delta u_i' u_j'} - 2\nu \overline{\frac{\partial u_i'}{\partial x_k} \frac{\partial u_j'}{\partial x_k}}. \tag{C.16}$$

Finally, the kinetic energy transport for turbulent fluctuation is given by

$$\begin{aligned} &\frac{1}{2} \overline{\frac{\partial u_i' u_i'}{\partial t}} + \frac{U_k}{2} \overline{\frac{\partial u_i' u_i'}{\partial x_k}} = -\overline{u_i' u_k'} \frac{\partial U_i}{\partial x_k} - \frac{1}{2} \frac{\partial}{\partial x_k} \overline{u_i' u_i' u_k'} \\ &- \frac{1}{2} \tilde{u}_k \overline{\frac{\partial u_i' u_i'}{\partial x_k}} - \overline{u_i' u_k'} \frac{\partial \tilde{u}_i}{\partial x_k} - \frac{1}{\rho} \overline{\frac{\partial p' u_i'}{\partial x_i}} + \frac{1}{2} \nu \overline{\Delta u_i' u_i'} - \nu \overline{\frac{\partial u_i'}{\partial x_k} \frac{\partial u_i'}{\partial x_k}}, \end{aligned} \tag{C.17}$$

after some calculus we obtain [26]:

$$\frac{1}{2}\overline{\frac{\partial u_i' u_i'}{\partial t}}(\boldsymbol{x}) + \underbrace{\frac{U_k}{2}\overline{\frac{\partial u_i' u_i'}{\partial x_k}}}_{C'(\boldsymbol{x})} = \underbrace{-\overline{u_i' u_k'}\frac{\partial U_i}{\partial x_k}}_{\mathcal{P}'(\boldsymbol{x})} \underbrace{-\frac{1}{2}\frac{\partial}{\partial x_k}\left[\overline{u_i' u_i' u_k'} + \overline{u_i' u_i' \tilde{u}_k} + 2\overline{u_i' \tilde{u}_i u_k'}\right]}_{\mathcal{D}'(\boldsymbol{x})}$$
$$+ \underbrace{\tilde{u}_i\overline{\frac{\partial u_k' u_i'}{\partial x_k}}}_{\mathcal{T}(\boldsymbol{x})} \underbrace{-\frac{1}{\rho}\overline{\frac{\partial p' u_i'}{\partial x_i}}}_{\varphi'(\boldsymbol{x})} + \underbrace{\frac{1}{2}\nu\overline{\Delta u_i' u_i'}}_{\mathcal{D}_\nu'(\boldsymbol{x})} \underbrace{-\nu\overline{\frac{\partial u_i'}{\partial x_k}\frac{\partial u_i'}{\partial x_k}}}_{\epsilon'(\boldsymbol{x})}. \tag{C.18}$$

C.3 Coherent kinetic energy transport

Multiplying (C.4a) by $\tilde{u}_j$ and taking the time average, by interchanging i and j and adding up the two terms, we obtain

$$\overline{\tilde{u}_j\frac{\partial}{\partial t}\left(U_i + u_i''\right)}(\boldsymbol{x}) + \overline{\tilde{u}_i\frac{\partial}{\partial t}\left(U_j + u_j''\right)}(\boldsymbol{x}) = 0. \tag{C.19}$$

Multiplying (C.4b) by $\tilde{u}_j$ and taking time average we obtain

$$\begin{aligned}\overline{\tilde{u}_j\left(U_k + u_k''\right)\frac{\partial}{\partial x_k}\left(U_i + u_i''\right)}(\boldsymbol{x}) &= \overline{\tilde{u}_j U_k\frac{\partial U_i}{\partial x_k}} + \overline{\tilde{u}_j U_k\frac{\partial u_i''}{\partial x_k}} + \overline{\tilde{u}_j u_k''\frac{\partial U_i}{\partial x_k}} + \overline{\tilde{u}_j u_k''\frac{\partial u_i''}{\partial x_k}},\\ &= \underbrace{\tilde{u}_j U_k\frac{\partial U_i}{\partial x_k}}_{a} + \underbrace{\tilde{u}_j U_k\frac{\partial \tilde{u}_i}{\partial x_k}}_{b} + \underbrace{\tilde{u}_j\tilde{u}_k\frac{\partial U_i}{\partial x_k}}_{c} + \underbrace{\tilde{u}_j\overline{u_k''\frac{\partial u_i''}{\partial x_k}}}_{d}.\end{aligned} \tag{C.20}$$

By interchanging i and j in each term and adding up the two terms, we obtain, respectively,

$$\begin{aligned}&(C.20a): \tilde{u}_j U_k\frac{\partial U_i}{\partial x_k} + \tilde{u}_i U_k\frac{\partial U_j}{\partial x_k}, \quad (C.20b): \tilde{u}_j U_k\frac{\partial \tilde{u}_i}{\partial x_k} + \tilde{u}_i U_k\frac{\partial \tilde{u}_j}{\partial x_k},\\ &(C.20c): \tilde{u}_j\tilde{u}_k\frac{\partial U_i}{\partial x_k} + \tilde{u}_i\tilde{u}_k\frac{\partial U_j}{\partial x_k},\\ &(C.20d): \tilde{u}_j\overline{u_k''\frac{\partial u_i''}{\partial x_k}} + \tilde{u}_i\overline{u_k''\frac{\partial u_j''}{\partial x_k}} = \tilde{u}_j\overline{u_k'\frac{\partial u_i'}{\partial x_k}} + \tilde{u}_j\tilde{u}_k\frac{\partial \tilde{u}_i}{\partial x_k} + \tilde{u}_i\overline{u_k'\frac{\partial u_j'}{\partial x_k}} + \tilde{u}_i\tilde{u}_k\frac{\partial \tilde{u}_j}{\partial x_k}.\end{aligned} \tag{C.21}$$

Multiplying (C.4c) by $\tilde{u}_j$ and taking the time average, by interchanging i and j and adding up the two terms, we obtain

$$-\frac{1}{\rho}\left[\overline{\frac{\partial}{\partial x_i}\left(P+p''\right)\cdot\tilde{u}_j}+\overline{\frac{\partial}{\partial x_j}\left(P+p''\right)\cdot\tilde{u}_i}\right](\boldsymbol{x}) = -\frac{1}{\rho}\left[\frac{\partial P}{\partial x_i}\cdot\tilde{u}_j+\frac{\partial P}{\partial x_j}\cdot\tilde{u}_i\right]-\frac{1}{\rho}\left[\frac{\partial\tilde{p}}{\partial x_i}\cdot\tilde{u}_j+\frac{\partial\tilde{p}}{\partial x_j}\cdot\tilde{u}_i\right]. \tag{C.22}$$

Multiplying (C.4d) by $\tilde{u}_j$ and taking the time average, by interchanging i and j and adding up the two terms, we obtain

$$\nu\overline{\Delta\left(U_i+u_i''\right)\cdot\tilde{u}_j}(\boldsymbol{x})+\nu\overline{\Delta\left(U_j+u_j''\right)\cdot\tilde{u}_i}(\boldsymbol{x}) = \nu\Delta U_i\cdot\tilde{u}_j+\nu\Delta U_j\cdot\tilde{u}_i+\nu\Delta\tilde{u}_i\cdot\tilde{u}_j+\nu\Delta\tilde{u}_j\cdot\tilde{u}_i. \tag{C.23}$$

The coherent kinetic energy transport for coherent fluctuation is given by

$$\begin{aligned}\tilde{u}_iU_k\frac{\partial U_i}{\partial x_k}+\tilde{u}_iU_k\frac{\partial\tilde{u}_i}{\partial x_k} &= -\tilde{u}_i\tilde{u}_k\frac{\partial U_i}{\partial x_k}-\tilde{u}_i\overline{u_k'\frac{\partial u_i'}{\partial x_k}}-\tilde{u}_i\tilde{u}_k\frac{\partial\tilde{u}_i}{\partial x_k}\\ &\quad-\frac{1}{\rho}\left[\frac{\partial P}{\partial x_i}\cdot\tilde{u}_i+\frac{\partial\tilde{p}}{\partial x_i}\cdot\tilde{u}_i\right]+\nu\Delta U_i\cdot\tilde{u}_i+\frac{1}{2}\nu\Delta\tilde{u}_i\tilde{u}_i-\nu\frac{\partial\tilde{u}_i}{\partial x_k}\frac{\partial\tilde{u}_i}{\partial x_k},\end{aligned} \tag{C.24}$$

which we may rewrite as [26]

$$\begin{aligned}&\underbrace{\tilde{u}_iU_k\frac{\partial U_i}{\partial x_k}+\tilde{u}_iU_k\frac{\partial\tilde{u}_i}{\partial x_k}}_{\tilde{C}(\boldsymbol{x})} = \underbrace{-\tilde{u}_i\tilde{u}_k\frac{\partial U_i}{\partial x_k}}_{\tilde{\mathcal{P}}(\boldsymbol{x})}\underbrace{-\tilde{u}_i\overline{\frac{\partial u_k'u_i'}{\partial x_k}}}_{\mathcal{T}(\boldsymbol{x})}\underbrace{-\frac{1}{2}\frac{\partial}{\partial x_k}\left[\tilde{u}_i\tilde{u}_i\tilde{u}_k\right]}_{\tilde{\mathcal{D}}(\boldsymbol{x})}\\ &\underbrace{-\frac{1}{\rho}\left[\frac{\partial P}{\partial x_i}\cdot\tilde{u}_i+\frac{\partial\tilde{p}}{\partial x_i}\cdot\tilde{u}_i\right]}_{\tilde{\varphi}(\boldsymbol{x})}+\underbrace{\nu\Delta U_i\cdot\tilde{u}_i+\frac{1}{2}\nu\Delta\tilde{u}_i\tilde{u}_i}_{\tilde{\mathcal{D}}_\nu(\boldsymbol{x})}\underbrace{-\nu\frac{\partial\tilde{u}_i}{\partial x_k}\frac{\partial\tilde{u}_i}{\partial x_k}}_{\tilde{\epsilon}(\boldsymbol{x})}.\end{aligned} \tag{C.25}$$